

PARAMETRIC COOLING AND ITINERANT FERROMAGNETISM IN A
DEGENERATE FERMI GAS

A Dissertation

Submitted to the Faculty

of

Purdue University

by

Leonardo F. de Melo

In Partial Fulfillment of the

Requirements for the Degree

of

Doctor of Philosophy

December 2018

Purdue University

Indianapolis, Indiana

THE PURDUE UNIVERSITY GRADUATE SCHOOL
STATEMENT OF COMMITTEE APPROVAL

Dr. Ruihua Cheng, Chair

Department of Physics

Dr. Le Luo

Department of Physics

Dr. Horia Petrache

Department of Physics

Dr. Yogesh Joglekar

Department of Physics

Dr. Chris Greene

Department of Physics

Approved by:

Dr. Ricardo Decca

Head of the Graduate Program

ACKNOWLEDGMENTS

I thank Dr. Le Luo for accepting me into his research group. I joined his lab knowing nothing about atomic physics research, and owe him much gratitude for everything I know today. He has taught me so much about atomic physics and continues inspire me to be a scientist. I am very grateful for all his patience and endless effort to train me as an experimental physicist.

Special thanks to my lab mates Wen Xu, Jiaming Li and Ji “Money” Liu for all their helpful ideas, constructive criticism, and support during our time together. I know my time in graduate school would not have been as fruitful or enjoyable without them by my side. I admire Jiaming’s leadership and thank him for teaching me so much about electronics. Many thanks also for taking me to all the excellent restaurants in Zhuhai during my visit. Wen Xu was a great partner for class projects, machining jobs, and the work on ferromagnetism; I could always count on him for a different perspective on things when something wasn’t working. If I ever needed a laugh or help with theoretical calculations, Ji Money was glad to offer his services with no payment required. Thanks also to the current members of the ${}^6\text{Li}$ team in Zhuhai: Xiao Zhang, Jianxiong Fang, Yang Chen and Tishuo Wang for helping me around the lab and continuing research on the apparatus I built.

My studies at IUPUI also provided me new friends from the physics department. Thank you to all the graduate students who spent time with me outside the lab. Our time together exploring Indianapolis was exciting, and our conversations were stimulating. Special thanks to the students in LD 065 for the non-physics discussions, and of course the coffee.

Throughout my academic career, my parents have supported me more than I could have imagined. They have made great efforts for me to be where I am today and I know I can count on them to keep encouraging me on my future endeavors.

Our journey together has led me to where I am today and I am forever thankful for all their sacrifice. I also thank my father for all his help with machining parts for our lab, supplying tools, and teaching me all I know about machining. He was the invisible member of our research group.

Lastly, I would like to thank my wife Rebecca for all the years of loving support and understanding. She has been with me from the start of my studies at IUPUI and has believed in me until the end. I cannot imagine going through all of this without her.

TABLE OF CONTENTS

	Page
LIST OF TABLES	viii
LIST OF FIGURES	ix
ABSTRACT	xvi
1 INTRODUCTION	1
1.1 Overview	2
1.1.1 Ultracold Fermi Gas	2
1.1.2 Cooling and Trapping Fermi Gases	3
1.1.3 Parametric Cooling in Cold Atoms	4
1.1.4 Itinerant Ferromagnetism in Cold Atoms	4
1.1.5 Absolute Absorption of ${}^6\text{Li}$ in an Ar Buffer Gas	5
1.2 Significance of Research	6
1.3 Organization	7
2 ${}^6\text{Li}$ FERMI GAS PROPERTIES	8
2.1 Electronic States of ${}^6\text{Li}$ in a Magnetic Field	8
2.1.1 Hyperfine States	9
2.1.2 Hyperfine States in Magnetic Fields	11
2.1.3 Optical Electronic Transitions	13
2.2 Properties of Trapped Fermi Gas	14
2.2.1 Ideal Fermi Gas in Harmonic Trap	14
2.2.2 Density Profile	15
2.3 Ultracold Atoms Interactions	16
2.3.1 s -wave Scattering	16
2.3.2 Feshbach Resonance	17
2.3.3 Tuning Interactions	18
3 EXPERIMENTAL APPARATUS	22
3.1 Vacuum System	22
3.1.1 Design	22
3.1.2 Preparation	26
3.1.3 Performance	28
3.2 ${}^6\text{Li}$ Oven	28
3.3 Laser Cooling and Trapping	29
3.3.1 Zeeman Slower	30
3.3.2 671 nm Laser Systems	31

	Page
3.3.3	671 nm Lasers Frequency Locking 35
3.3.4	MOT 39
3.4	Optical Dipole Trap 43
3.4.1	Beam Generation 43
3.4.2	Optical Dipole Trap Design 46
3.4.3	Measured Trap Characteristics 46
3.5	Electromagnets 48
3.5.1	Design 48
3.5.2	Performance 49
3.6	Radio-Frequency Antenna 51
3.7	Control and Data Acquisition 51
3.7.1	Timing System 52
3.7.2	Absorption Imaging 52
3.8	Experimental Methods 57
3.8.1	Magnetic Field Calibration 57
3.8.2	Evaporative Cooling 58
3.8.3	Image Processing 59
4	PARAMETRIC COOLING 61
4.1	Introduction 61
4.1.1	Cooling Techniques for Ultracold Atoms 61
4.1.2	Parametric Excitation 64
4.1.3	Parametric Cooling in Cold Atoms 66
4.2	Optical Trap Anharmonicity 67
4.3	Experimental Procedure 70
4.4	Results 72
4.4.1	Modulation Amplitude 72
4.4.2	Modulation Frequency 74
4.4.3	Modulation Time 74
4.5	Simulation of Parametric Cooling 74
5	ITINERANT FERROMAGNETISM IN A TWO-DIMENSIONAL FERMI GAS 78
5.1	Stoner Model of Itinerant Ferromagnetism 78
5.2	Mean-Field Treatment of Itinerant Ferromagnetism in an Atomic Fermi Gas 80
5.2.1	Three-Dimensional Gas 80
5.2.2	Two-Dimensional Gas 81
5.2.3	Dimensional Dependence of Gas Properties 83
5.3	Experimental Search for Itinerant Ferromagnetism in a Three-Dimensional Atomic Fermi Gas 85
5.3.1	Review of First Experiment from MIT Group 85
5.3.2	Review of Second MIT Group Experiment 88

	Page
5.4 Repulsive Polaron in an Atomic Fermi Gas	89
5.4.1 Spectrum and Lifetime of Polaron in Three Dimensions	91
5.4.2 Spectrum and Lifetime of Polaron in Two Dimensions	92
5.4.3 Search of Ferromagnetism in a Two-Dimensional Fermi Gas	95
5.4.4 Preparation of Repulsive Polaron	98
6 ABSOLUTE ABSORPTION OF A LITHIUM VAPOR CELL	101
6.1 Theory	101
6.1.1 Effective Three-Level Model	101
6.1.2 Optical Master Equation and Rate Equation	103
6.1.3 Velocity-Changing Collisions	104
6.2 Transverse Gas Dynamics and Numerical Solution of Atom-Light Coupled Equations	105
6.3 Experimental Setup	110
6.4 Results	112
6.4.1 Experimental Method and Comparison with Simulation	112
6.4.2 Peak Transmission as Function of Beam Intensity and Size	113
7 SUMMARY AND OUTLOOK	125
REFERENCES	129
A Physical Constants & ${}^6\text{Li}$ Properties	138
B Mathematica Code for Parametric Cooling	139
C Mathematica Code for Polaron Properties	144
D Mathematica Code for Absolute Absorption	147
VITA	152

LIST OF TABLES

Table	Page
2.1 ${}^6\text{Li}$ properties for hyperfine interactions	9
2.2 ${}^6\text{Li}$ Feshbach resonance parameters, values taken from Ref. [74].	19
3.1 Operating temperatures of the oven sections.	29
3.2 Zeeman slower coil vertical windings.	32
3.3 Dynamic MOT properties	42
4.1 Parametric cooling in cold atoms.	68
6.1 Conversion from dimensional variables to nondimensional variables.	109
A.1 ${}^6\text{Li}$ properties	138
A.2 Physical constants	138

LIST OF FIGURES

Figure	Page
2.1 Partial hyperfine energy structure of ${}^6\text{Li}$. The $2^2S_{1/2} \leftrightarrow 3^2P_{3/2}$ transition (blue arrow) has wavelength 323.361168 nm, and the $2^2S_{1/2} \leftrightarrow 2^2P_{3/2}$ (red arrow) is the D_2 transition with 670.97738 nm wavelength.	10
2.2 $2^2S_{1/2}$ hyperfine energy splitting description by the Breit-Rabi equation.	12
2.3 Degenerate Fermi gas energy characteristics. (a) Two-spin degenerate Fermi gas at zero temperature in a harmonic trap. (b) Fermi-Dirac distribution at zero temperature. At zero temperature the chemical potential equals the Fermi energy.	14
2.4 Two-channel Feshbach resonance of scattering length. (a) Lennard-Jones like potentials for the two-channel Feshbach resonance model. The resonance occurs when the open channel entrance energy is tuned to a bound state in the closed channel. (b) The scattering length enhancement as function of magnetic field. The insets show the BEC region for $a < 0$, the BCS region at $a > 0$ and the unitary region for $a \rightarrow \pm\infty$	20
2.5 Energy states and Feshbach resonance profiles for ${}^6\text{Li}$. (a) Energy shifts due to applied magnetic field for the three lowest energy states of ${}^6\text{Li}$. (b) Scattering length dependence on magnetic field in terms of the Bohr radius for the lowest spin states. The narrow Feshbach resonance centered at 543 G for $ 1\rangle$ - $ 2\rangle$ is not pictured.	21
3.1 Vacuum system design. Not pictured is the non-evaporable getter material.	23
3.2 Oven side vacuum setup. The arrow indicates the atomic beam from the oven. An angle valve used during loading of ${}^6\text{Li}$ into the oven is shown to the left of the oven. An all-metal angle valve is used to connect a turbo pump into the system during initial pumping stages and baking. The differential pumping tube shown in copper color is used to keep the science chamber side at higher vacuum.	25
3.3 Vacuum system baking. Only the science chamber side is pictured; the same method of heating with heat tapes and aluminum foil was performed on the oven side.	26
3.4 Pressure and temperature curves during bakeout.	27

Figure	Page
3.5 Lithium oven design and implementation. (a) ${}^6\text{Li}$ oven design with a rotatable flange on the oven nozzle and 1.33" flange on the top for lithium loading. (b) Oven mounted on apparatus with heating sections. Layers of high-temperature cement are used to separate the nichrome wires from the thermocouples.	30
3.6 Zeeman slower magnetic field profile. A current of 9.6 A was used in all cases.	32
3.7 Zeeman slower. The left flange is mounted to the oven side and right flange is mounted on the science chamber giving the slower a decreasing magnetic field profile.	32
3.8 Electronic transistions used with the Zeeman slower.	33
3.9 Frequency locking and beam generation for the slowing and MOT beams. (a) TA 100 optical layout for frequency locking, slowing, and MOT beams. (b) Locking signal from Digilock. The yellow curve is the signal from the probe beam and the red curve is the error signal.	36
3.10 Vapor cell used for TA 100 frequency locking.	37
3.11 Offset-locking schematic and electronic circuit. (a) Offset-locking diagram. The input is the signal from the photodiode and the outputs go to the piezotransducer and current controls of the DL Pro. (b) Offset-locking electronics. 1: photodiode in, 2: PIDs out, 3: signal generator in, 4: delay line in, 5: delay line out, 6: spectrum Analyzer out.	38
3.12 Optical layout for the imaging beam from DL Pro.	39
3.13 MOT operation description. (a) Counter-propagating beams and anti-Helmholtz coils. (b) Circularly polarized beams with frequency ω and detuning from resonance δ create a radiation pressure force on the atoms that is spatially dependent due to the magnetic field gradient.	41
3.14 MOT transitions. The hyperfine splitting of the $2^2P_{3/2}$ states is smaller than the natural linewidth of the D_2 transition.	42
3.15 ODT control and optical layout.	44
3.16 Optical and atomic beams in the science chamber. Beam sizes are not to scale.	45
3.17 Trap potential of the crossed-beam ODT	45
3.18 Trap frequency measurement in z -direction at $0.1U_0$. (a) is the cloud size obtained via a Gaussian distribution fit and (b) is the atom number. . . .	47

Figure	Page
3.19 Schematic of coil and housing design. Water cooling of coils uses a water flow of about 3 gallons/minute.	48
3.20 H-bridge circuit for the down coil. Each MOSFET has its own optoisolator and power supply. The optoisolators are used to protect the DAQ card from over current.	49
3.21 Measurement (blue points) and theoretical prediction (black lines) of one of the coils used for the MOT and Feshbach resonance magnetic fields. (a) Vertical measurement. (b) Horizontal measurement. The vertical magnetic field was measured using 120A current and distance was measured from the center of MOT (6.2 cm). The horizontal field was measured at a 7.6 cm vertical distance from the bottom with a 10 A current	50
3.22 RF antenna. (a) Antenna with impedance matching circuit. (b) Circuit diagram for impedance matching circuit.	51
3.23 Main DAQ timing control for experiments. A timing file read by Labview sets the timing sequences.	53
3.24 Sample image capturing and data analysis with LabView.	54
3.25 Absorption imaging scheme.	55
3.26 Absorption imaging of trapped atomic cloud in the horizontal direction. The cloud size is $42 \mu\text{m} \times 198 \mu\text{m}$ with $2\theta = 14^\circ$	56
3.27 Measurement of cloud size for magnetic field calibration.	56
4.1 Cooling methods used in magnetic and/or optical traps. Black plots are the initial trap potential and red plots final. (a) By moving one of the cross-dipole trap beams, the waist at the location of the cloud is increased, which increases the trap frequency and reduces the trap volume. (b) A beam of much smaller power and waist is added to the trapping beams to create a “dimple” in the potential. (c) The addition of a bias magnetic field gradient tilts the trap potential to “spill” atoms from trap. (d) Unlike the other methods, the RF-knife removes atoms based on their position in the magnetic trap without lowering the confinement depth.	62
4.2 Parametric driving characteristics for a harmonic oscillator. (a) A child swinging at frequency ω_0 , being pushed at frequency $\omega(t)$. (b) Simulation of Eq. 4.1 with $\delta = 0.15$, $\omega_0 = 2\pi \times 10$ Hz, and $t_m = 2\pi/\omega_m$	65
4.3 Deviation of the harmonic approximation from the actual trap in the x -direction as a function of position in the z -axis. (a) Harmonic approximation using the $\omega_x(z)$ calculated from Eq.4.7. (b) Harmonic approximation using the ω_x calculated from the trap depth as in Eq. 3.11.	69

Figure	Page	
4.4	The x -axis trap frequency $\omega_x(x, 0, z)$ is plotted in the x - z plane in term of the harmonic frequency $\omega_{x0} = 2\pi \times 760$ Hz (the calculated value from the trapping potential). The radial and axial atom densities $n(x)$ and $n(z)$ are plotted in the left and bottom frames for a Fermi gas of 1.6×10^5 atoms per spin state at $T/T_F = 0.6$ using a 1D Thomas-Fermi distribution. The red dashed lines show the positions of the Fermi radii in the radial (σ_x) and axial (σ_z) directions, where the local trapping frequency drops to $\omega_x(\sigma_x, 0, 0) = 0.89\omega_{x0}$ and $\omega_x(0, 0, \sigma_z) = 0.55\omega_{x0}$	69
4.5	Experimental timing sequence. The sequence starts at the MOT loading stage where the ODT beam is first turned on, and ends after the two shots are taken for absorption imaging.	71
4.6	The dependence of the radial and axial energies on the modulation amplitudes. (a) The absorption images of the atom clouds show a dramatic decrease of the axial cloud sizes with an increase of modulation amplitudes, where $\omega_m = 1.5\omega_{x0}$. (b) The dependence of the radial energies on the modulation amplitude. (c) The dependence of the radial energies on the modulation amplitude. In both (b) and (c), blue triangles are at the modulation frequency $1.5\omega_{x0}$, and red squares are at $2.0\omega_{x0}$. The solid lines represent the simulation of the anharmonic oscillator model using the same simulation parameters for the frequency dependence.	73
4.7	The dependence of parametric excitation on the modulation frequency. The radial and axial NIMS, the normalized atom number, and the radial and axial energies are shown from the top to the bottom. The harmonic frequency $\omega_{x0} = 2\pi \times 740$ Hz is the measured value. The dashed lines indicate the average value without parametric modulation ($\delta = 0$). The solid lines show the simulation results.	75
4.8	Time modulation with $\delta = 0.5$ and $\omega_m = 1.45\omega_x$. (a) The absorption images of the atomic clouds of various modulation times. (b) The dependence of $E(x, z)/E_F$ on modulation time (blue circles are for E_z/E_F and the red squares are for E_x/E_F). The inset figure is the atom number versus modulation time. Error bars represent one standard deviation. . . .	76
5.1	Stoner model properties for a three-dimensional system. (a) Total energy as a function of polarization. (b) Polarization, kinetic energy and volume. The kinetic energy is normalized to the total energy and the volume is normalized to the ideal gas volume. The dashed lines in (b) are for $k_F a = \pi/2$ and $k_F a = 3\pi/4\sqrt[3]{2}$	82

Figure	Page
5.2 Stoner model properties for a two-dimensional system. (a) Total energy as a function of polarization. (b) Polarization, kinetic energy and volume. The kinetic energy is normalized to the total energy and the volume is normalized to the ideal gas volume. The dashed line in (b) indicates $a/l_z = \sqrt{\pi/2}$	84
5.3 Characterization of molecule formation at short and long hold times, and at different values of the interaction strength. The closed symbols—circles (black) at 790 G with $k_F a = 1.14$, squares (blue) at 810 G with $k_F a = 2.27$, and diamonds (red) at 818 G with $k_F a = 3.5$, represent the normalized number of free atoms, while the open symbols represent the total number of atoms, including those bound in Feshbach molecules (open circles at 790 G with $k_F a = 1.14$). The crosses (green) show the molecule fraction. Image taken from Ref. [30]	87
5.4 Phase diagram for strongly interacting Fermi gas in two dimensions. Image taken from Ref. [102].	88
5.5 Three-dimensional polaron characteristics. (a) Energy spectrum. (b) Quasiparticle weight. (c) Lifetime of polaron against attractive polaron decay. The plots are based on theory from Refs. [108, 110].	93
5.6 Two-dimensional polaron characteristics. (a) Energy spectrum . (b) Quasiparticle weight. (c) Lifetime of polaron against attractive polaron decay. The interaction parameter is $\ln(k_F a_{2D}) = -\ln(E_b/E_F)/2$. The plots are based on theory from Refs. [113, 116].	94
5.7 First Brillouin zone energy bands for a one-dimensional optical lattice created with laser of wave vector $k = 2\pi/\lambda$. The increasing trap depth creates smaller energy band depths with larger energy gaps.	96
5.8 Lattice potential illustrating the relevant energies for confined two-dimensional motion.	97
5.9 Tunneling time to adjacent pancake with $2\theta = 35^\circ$, and $w_0 = 100 \mu\text{m}$	99
5.10 The region to the left of solid line does not satisfy the Fermi energy criterion; between the solid and dashed lines both conditions are satisfied; and region to the right of the dashed line does not satisfy the tunneling criterion.	99
5.11 Ferromagnetic instability threshold in the gray region.	100

Figure	Page
6.1 ${}^6\text{Li} - D_2$ Diagram. A π -polarized, monochromatic light stimulates both $ 1\rangle \rightarrow 3\rangle$ and $ 2\rangle \rightarrow 3\rangle$ transitions. The full level model in (a) is simplified to the composite level model in (b). δ is the laser detuning from the transition between average of ground states to excited state. Energy levels are not drawn to scale.	102
6.2 Description of the velocity-changing collisions effect on the light absorption. For the inset, the resonant transition is $2^2S_{1/2} F = 3/2\rangle \leftrightarrow 2^2P_{3/2}$.	106
6.3 Experimental setup for absorption measurement. TA: taper-amplified diode laser; FC: fiber couplers and optical fiber in between; P: linear polarizer; T: telescope; I: adjustable iris; BS: beam splitter; VC: vapor cell; L: lens; PD1 and PD2: signal and reference photodiodes. The laser light is sent through a fiber coupling scheme to improve the Gaussian beam profile quality. Then the beam is enlarged and split between PD1 and PD2 paths. In the vapor cell, A,B and C are places we put thermocouples on, and the temperatures are 340 °C, 320 °C and 320 °C respectively. AB and AC are both 5 cm long.	111
6.4 Gaussian beam shape with different beam profiles. The black line is the full input beam intensity distribution in the radial direction. The radius unit is the e^{-1} radius (2.5 mm) of the Gaussian beam and the intensity unit is normalized to the central intensity at $r = 0$. The radii of profiles corresponding to the transmitted power of 100%, 80%, 60%, 40%, 20%, 10%, and 5% of the full beam power are indicated by the red lines. The iris filters out optical power outside the red lines to obtain the desired profiles.	112
6.5 Experimental results for 340 °C, $I=10I_{sat}$, 40% power transmitted through iris. (a) Green dots: measurement data, blue curve: fitting by Eq. 6.12, and (b) red dots: residual of fitting.	114
6.6 Transmission ratio vs. central beam intensity for different beam sizes. Beam size is expressed as the percentage of full beam power transmitted through iris. Markers are experimental results, where red squares are 40% power transmitted, green up-triangles are 20%, gray down-triangles are 10%, and magenta diamonds are 5%. The four solid curves in the upper part of the figure are simulations based on our model, and the four dashed curves in the lower part are calculated based on two-level model in Sec. VIII of Ref. [54].	114
6.7 RMS deviation for simulated velocity-changing collision decay rate where γ_N is the decay rate of the D_2 transition. Each curve is calculated for all seven I/I_{sat} values for each power percentage.	116

Figure	Page
6.8 Simulation and experimental results at fixed beam power for (a) 5% transmitted power and (b) 10% transmitted power.	117
6.9 Simulation and experimental results at fixed beam power for (a) 20% transmitted power and (b) 40% transmitted power.	118
6.10 Simulation and experimental results at fixed beam power for (a) 60% transmitted power and (b) 80% transmitted power	119
6.11 Simulation and experiemental results at 100% transimitted power.	120
6.12 Simulation and experimental results at fixed beam power for (a) $0.1I/I_{sat}$ transmitted power and (b) $0.32I/I_{sat}$ transmitted power.	121
6.13 Simulation and experimental results at fixed beam power for (a) $0.5I/I_{sat}$ transmitted power and (b) $1I/I_{sat}$ transmitted power.	122
6.14 Simulation and experimental results for (a) $3.2I/I_{sat}$ and (b) $5I/I_{sat}$. . .	123
6.15 Simulation and experimental results at $10I/I_{sat}$	124
7.1 Magnet design and implementation. (a) Design for magnets to fit inside recessed window for closer proximity to trapped atoms with the red rectangles indicate the region of square wire windings. (b) Implementation of design on a water-cooled copper mount.	127
7.2 MOSFET mount design and implementation. (a) Mounting on copper plates for current distribution and cooling. (b) Implementation of design on a water-cooled aluminum plate.	128

ABSTRACT

de Melo, Leonardo F. Ph.D., Purdue University, December 2018. Parametric Cooling and Itinerant Ferromagnetism in a Degenerate Fermi Gas. Major Professor: Ruihua Cheng.

Presented in this thesis is the construction of an apparatus to produce optically trapped ${}^6\text{Li}$ atoms in the two lowest hyperfine states, the observation of cooling the trapped atoms by parametric excitation, and a study on the searching for itinerant ferromagnetism in a two-dimensional Fermi gas.

In the parametric cooling experiment, a technique is developed to cool a cold atomic Fermi gas by parametrically driving atomic motions in a crossed-beam optical dipole trap. This method employs the anharmonicity of the optical dipole trap, in which the hotter atoms at the edge of the trap feel the anharmonic components of the trapping potential, while the colder atoms in the center of the trap feel the harmonic one. By modulating the trap depth with frequencies that are resonant with the anharmonic components, hotter atoms are selectively excited out of the trap while keeping the colder atoms in the trap, generating a cooling effect.

An analytical study of itinerant ferromagnetism in a two-dimensional atomic Fermi gas is presented, based on the past experiments done with three-dimensional Fermi gases. Here, the formation of repulsive polarons in a strongly-interacting Fermi gas is used as an initial condition. Then the observation of itinerant ferromagnetism is realized by detection of ferromagnetic domains in the two-dimensional gas.

Additionally, an experiment and simulation is performed on the effect of velocity-changing collisions on the absolute absorption of ${}^6\text{Li}$ vapor in an Ar buffer gas. The dependence of probe beam absorption is observed by variation of beam intensity and spatial evolution. The simulation of an effective three-level energy model with

velocity-changing collisions determines a collision rate that agrees with transmission data collected.

1. INTRODUCTION

The search for the structural composition of the universe has intrigued mankind since the time of the Atomists in the fifth B.C., with Democritus formulating the first atomic theory based on philosophical reasoning. Not until the nineteenth century, was an atomic theory developed based on scientific observation by John Dalton. It was not until 1932 when James Chadwick discovered the neutron, that the complete internal structure of what we now call an atom was found. Although the definition of an atom given by Democritus of the smallest indestructible amount of matter differs from the modern definition, the study of atoms through atomic physics is still very much involved in fundamental research, and application of discoveries in atomic physics are used in various scientific fields [1, 2].

Quantum theory, which was created to explain observed phenomena which classical theories failed to explain [3], has led to enormous discoveries in atomic physics. One such development was the invention of the laser [4], which is widely used in atomic physics research. Further advancement of quantum theory led to the development of laser cooling and trapping techniques such as the Zeeman slower [5] and magneto-optical trap (MOT) [6]. These are two techniques among many others essential to ultracold atoms research that has led to the groundbreaking creation of the Bose-Einstein condensate (BEC) [7–9] and the degenerate Fermi gas (DFG) [10] on table top experiments.

The experimental techniques used in achieving an atomic DFG have grown since the first was achieved in 1999 [10] to produce trapped gases deep in the degenerate regime for probing new physics [11]. This dissertation explores a cooling technique to lower the temperature of a DFG and increase its degeneracy, and how an ultracold Fermi gas can be used to explore itinerant ferromagnetism.

Atomic physics based on a hot vapor is also explored in this thesis with a study of absolute absorption of a buffer-gas filled lithium vapor cell. Many techniques used in cold atom research were first developed using gases at high temperatures, like laser frequency locking, magnetometry and atomic clocks [12–14]. Here the absolute absorption of a ${}^6\text{Li}$ -Ar filled vapor cell is measured as a function of probe beam intensity and beam diameter to examine the effects of velocity-changing collisions on the transmitted beam.

1.1 Overview

1.1.1 Ultracold Fermi Gas

Quantum effects begin to appear in an atomic ensemble when the phase-space density $n\lambda_{dB}^3$ reaches values on the order of 1. This occurs in disparate systems in nature, like the electron gas in metals and superfluid helium. The phase-space density is dependent on the density n and the de Broglie wavelength of the particles $\lambda_{dB} = \sqrt{h^2/2\pi mk_B T}$, where m is the mass of the particle and T is the temperature of the gas. In a dilute trapped atomic gas with typical density of $\sim 10^{13} \text{ cm}^{-3}$, the phase-space requirement leads to a necessary temperature of $\sim 10^{-5} \text{ K}$, whereas for superfluid helium the temperature is about 1 K. In these systems, the average interparticle spacing in the gas is of the same order as the de Broglie wavelength, and classical mechanics no longer describes the dynamics of the atoms correctly.

The advent of table-top ultracold atomic Fermi gas experiments has been used to observe the BEC-BCS crossover [15]. It describes the fermion pairing on the repulsively interacting BEC side, the weak coupling of Cooper pairs on the Bardeen-Cooper-Schrieffer (BCS) side, along with the strongly interacting region in between. This has also led to the creation of molecular BEC from fermion pairs that form dimers via tunable interactions using Feshbach resonance [16], and Cooper pairs. The tunability of repulsive and attractive interactions has been a breakthrough that allows for the study of universal phenomena in strongly interacting fermions like

the quark-gluon plasma and neutron stars [17]. Other quantum effects first seen in condensed matter like the spin-Hall effect and topological effects have been observed in DFG systems with the emergence of synthetic magnetic fields [18] and optical lattices [19, 20].

1.1.2 Cooling and Trapping Fermi Gases

Laser cooling and trapping techniques, such as the Zeeman slower and MOT that were developed in the 1980's, have been greatly improved. This has allowed experiments to start with hot alkali atomic vapors with temperatures in the order of 100 K and reach final temperatures in the hundreds of μK [5, 6], with gray molasses recently showing success in cooling below the Doppler limit of the MOT [21]. These cooling and trapping methods take advantage of the Zeeman splitting of hyperfine energy levels to drive transitions from ground to excited states using optical wavelengths. Although the achieved temperatures of $\sim 10 \mu\text{K}$ are not appropriate for the formation of degenerate quantum gases as the phase-space density is orders of magnitude too low, these techniques are still a required starting point for experiments. After the initial cooling and trapping in a MOT, the atoms are then transferred either to a magnetic trap that uses the interaction between the magnetic moment of the atoms and a bias magnetic field [22], or an optical trap utilizing the interaction between the electric dipole moment of the atoms and the electric field of a far-detuned laser [23]. The last stage in the creation of a degenerate quantum gas in a magnetic or optical trap is the application of evaporative cooling [7, 8].

The use of evaporative cooling leading to the creation of trapped degenerate quantum gases differs substantially in magnetic and optical traps due to the generation of the trapping potential and how the atoms react to changes in the trap. In magnetic traps, RF-induced evaporation generates an “anti-trapping” potential for atoms depending on an atom’s location and hyperfine state [9], while the trapping potential

produced by the trapping coils remains constant. In optical traps, the trap potential is lowered by decreasing the trapping laser intensity to expel hot atoms from the trap.

1.1.3 Parametric Cooling in Cold Atoms

Cooling of trapped atomic gases with parametric excitation has been accomplished with spatial [24] and amplitude modulation [25, 26] of the trap, but not with a degenerate Fermi gas as shown in this thesis. In an optical trap, this cooling method employs the anharmonicity of the ODT, in which the hotter atoms at the edge of the trap feel the anharmonic components of the trapping potential, while the colder atoms in the center of the trap feel the harmonic one. By modulating the trap depth with frequencies that are resonant with the anharmonic components, hotter atoms are selectively excited out of the trap while keeping the colder atoms in the trap, generating parametric cooling. The cooling effect is determined by observation of atom number loss, cloud size reduction and temperature reduction, while the trap depth before and after the modulation remain the same. Maintaining the trap depth the same and selectively expelling atoms from the trap are the key differences between parametric cooling and the standard evaporative cooling.

1.1.4 Itinerant Ferromagnetism in Cold Atoms

The creation of ultracold fermionic gases initiate interest in simulating the behavior of mobile electrons in ferromagnetic materials, by seeking to observe domain formation in repulsive two-spin Fermi gases. Observation of itinerant ferromagnetism is of interest for the study of ferromagnetic high-temperature superconductors for its possible application in novel solid state devices [27].

While the atomic fermion system offers tunable dimensionality, spin imbalance and repulsive interactions, the pairing instability in competition with ferromagnetism [28] remains an obstacle in the attempted observation of ferromagnetic domain formation. Experimental results supporting evidence provided by the Stoner model were

observed in an experiment using a three-dimensional gas of ${}^6\text{Li}$ atoms [29], but a later experiment showed that the formation of dimers impeded the ferromagnetic phase from occurring [30]. Predicted results based on the Stoner model were observed in an experiment using ${}^6\text{Li}$ atoms [29], but later the gas was shown to be in a paramagnetic phase with the formation of dimers impeding the ferromagnetic phase from occurring. My work is to show that a two-dimensional repulsively interacting Fermi gas is a more stable system to observe itinerant ferromagnetism.

Two other experiments have been conducted by indirect methods: One using atomic bosons in an optical lattice observed effective ferromagnetic domains in momentum space by shaking the optical lattice, leading to band structure engineering [31]. Another started with spatially separated spins to observe the spin dynamics of the system [32]. Although it did not achieve direct observation of domain formation from a balanced spin gas, the metastable domain separation retains interest in this area.

1.1.5 Absolute Absorption of ${}^6\text{Li}$ in an Ar Buffer Gas

Optical absorption of an atomic vapor has been a subject of interest in a variety of experiments with diverse emphases [33, 34], such as atomic clock [35], sensitive magnetometer [36], spin polarized gas [37, 38], laser frequency stabilization [39, 40], measurements of atomic collision [41, 42], measurements of Boltzmann constant [43–45], and quantum repeaters [46]. Particularly, the absolute value of absorption can provide direct measurements of atomic transition strength [47], atomic collision interaction [48], and atomic number density [49]. It provides a tool to study atomic collision kernel [50, 51], detect chemical compounds of trace amount [52, 53], and can be used to test sophisticated atomic models with minimal restrictive assumptions [54, 55].

1.2 Significance of Research

There has been interest in applying parametric excitation to trapped atoms in order to achieve cooling in magnetic and optical traps with amplitude and position modulation of the trapping potential for over a decade [24, 25]. Our demonstration of the parametric excitation method to cool a DFG for the first time presents the potential of being able to cool a thermal gas into degeneracy in an ODT without lowering the trap frequency as in evaporative cooling. This method is also much simpler to implement than other cooling techniques using an ODT because it does not require additional optomechanical components, laser beams or magnetic fields as required by other cooling methods. The tunability of trap anharmonicity made possible with trap geometries utilizing multiple Gaussian beams or a single Gauss-Laguerre beam allows the parametric excitations to create temperature anisotropy due to the cooling of the gas only in the excited trap frequency direction. In particular, “box-like” potentials [56, 57] provide greater anharmonicity on multiple axes, which would provide better cooling than what was shown in our ODT.

In itinerant ferromagnetism research, simulating electron dynamics in solid state materials with controllable interaction strength and dimensionality of an atom trap is desirable for better control of experimental parameters than is available in solid state systems. Many theoretical models and proposals have been developed to look for a ferromagnetic phase in the gas with predictions made with various interaction strengths in multiple dimensional configurations [58–60]. Here, a repulsive two-dimensional Fermi gas of polarons is used as a model system for the observation of ferromagnetic domains following the Stoner model.

Previously, the absolute absorption of atomic vapor cell has been studied both experimentally and theoretically. On the experimental side, the precise measurement of the absorption of an atomic vapor cell had been implemented in the weak-probe regime [61], strong-probe regime [48, 62], and with magnetic fields [63]. In the weak-probe regime, the atomic population is in thermodynamic equilibrium in terms of

both atomic energy states and velocity so that the absolute value of a frequency dependent absorption reveals the atomic distribution in both internal and external states. In the strong-probe regime, the light intensity affects the distribution of atomic population, resulting a nonlinear dependence of the absolute absorption on the input light intensity. In the presence of a magnetic field, the effects of Zeeman splitting makes the absolute absorption strongly polarization dependent. Here a study covering the weak and strong probe regime is realized with a theoretical model including the effects of velocity-changing collisions on the absorption spectrum of the gas.

1.3 Organization

The remainder of this thesis is organized as follows:

- Chapter 2 describes the internal atomic structure of ${}^6\text{Li}$ required for cooling, trapping and probing ${}^6\text{Li}$ atoms, along with collisional properties of ultracold gases necessary for production of an atomic DFG.
- Chapter 3 describes the experimental apparatus constructed to create a two-spin DFG in an all-optical trap.
- Chapter 4 discusses the main result of this thesis: parametric cooling of a DFG in an all-optical trap.
- Chapter 5 explores itinerant ferromagnetism in a two-dimensional atomic Fermi gas.
- Chapter 6 reports the absolute absorption study of a hot ${}^6\text{Li}$ gas in an Argon buffer gas to probe for velocity changing collisions.
- Chapter 7 concludes the work presented in the previous chapters and presents the future work to be done in improving the current apparatus for forthcoming experiments.

2. ${}^6\text{Li}$ FERMI GAS PROPERTIES

With all ultracold atom experiments, the known electronic structure of the atomic species allows the use of electromagnetic fields to interact with the atom, allowing control over energy states needed for cooling, trapping, probing, and interaction control. The necessary atomic theory for use in experiments, with emphasis on ${}^6\text{Li}$ are covered in this section.

2.1 Electronic States of ${}^6\text{Li}$ in a Magnetic Field

As true for all alkali atoms, ${}^6\text{Li}$ is a “hydrogen-like” atom with one electron in the $n = 2$ state orbiting around a charged core. The interaction of the valence electron with the inner core, together with the interaction between the spin of the electron and the angular momentum of its orbit is known as *spin-orbit* coupling. This coupling is described with the Hamiltonian [64]

$$H_{SO} = \frac{1}{2m_e c^2} \frac{1}{r} \left(\frac{d\Phi}{dr} \right) \mathbf{L} \cdot \mathbf{S} \quad (2.1)$$

where Φ is the potential of the inner core, r is the radial coordinate and \mathbf{L} and \mathbf{S} are the orbital angular momentum and spin operators respectively. Working in the $J = L + S$ total electronic angular momentum basis, and following the triangle rule $|L - S| \leq J \leq (L + S)$ the fine structure splits the 2^2P level into 2 levels with $J = 3/2$ and $J = 1/2$. The transition energy for $2^2S_{1/2} \rightarrow 2^2P_{3/2}$, known as the D_2 transition is an initial guide to tuning the external cavity-diode lasers (ECDL) wavelength for the necessary cooling, trapping and probing wavelengths used during experiments, as used in Sec. 3.3.

2.1.1 Hyperfine States

In determining the hyperfine structure of an alkali atom, the interaction is between the spin \mathbf{I} of the nucleus due to its constituents, and the magnetic field at the position of the nucleus that is created by the valence electron. Also required is the electric quadrupole expansion of the charge distributions of the electron and nucleus for the $L = 1$ state (important for the D_2 transition with $J=3/2$) where the angular wavefunction of the valence electron is asymmetric. Working in the $\mathbf{F} = \mathbf{J} + \mathbf{I}$ basis for the total angular momentum of the atom, the quantum number F follows the triangle rule $|J - I| \leq F \leq (J + I)$. The hyperfine energy shift from the fine-structure energy for F values is given by [65]

$$\Delta E_{hf} = \frac{A_{hf}K}{2} + B_{hf} \frac{\frac{3}{2}K(K+1) - 2I(I+1)J(J+1)}{2I(2I-1)2J(2J-1)}, \quad (2.2)$$

where the first term is the nuclear-electronic spin interaction $A_{hf}\mathbf{I}\cdot\mathbf{J}$, $K = F(F+1) - J(J+1) - I(I+1)$ and the constants A_{hf} and B_{hf} are the magnetic dipole hyperfine structure constant and electric quadrupole hyperfine constant respectively. A partial hyperfine energy structure diagram of ${}^6\text{Li}$ is shown in Fig. 2.1.

Table 2.1.
 ${}^6\text{Li}$ properties for hyperfine interactions

Quantity	Value	Property
$2^2S_{1/2}, g_J$	2.0023010	Electron Spin g -factor
$2^2P_{3/2}, g_J$	1.335	Electron Spin g -factor
g_I	-0.0004476540	Total Nuclear g -factor
S	1/2	Total Electronic Spin
I	1	Total Nuclear Spin
A_{hf}	-1.155 MHz	$2^2P_{3/2}$ Magnetic Dipole Constant
B_{hf}	-0.01 MHz	$2^2P_{3/2}$ Electric Quadrupole Constant

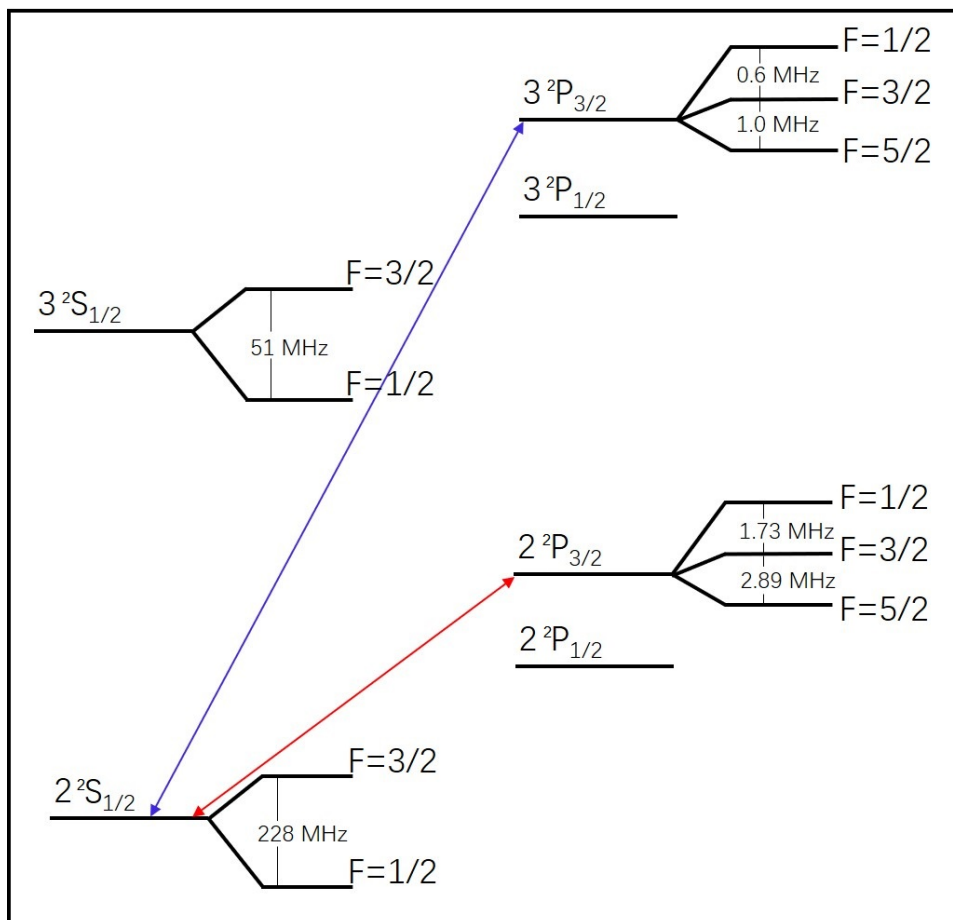


Figure 2.1. Partial hyperfine energy structure of ${}^6\text{Li}$. The $2^2S_{1/2} \leftrightarrow 3^2P_{3/2}$ transition (blue arrow) has wavelength 323.361168 nm, and the $2^2S_{1/2} \leftrightarrow 2^2P_{3/2}$ (red arrow) is the D_2 transition with 670.97738 nm wavelength.

2.1.2 Hyperfine States in Magnetic Fields

When an atom is placed in a magnetic field, the nuclear and electronic spins interact with the external field giving rise to the Zeeman effect. The interaction has the Hamiltonian

$$H_{B,ext} = \frac{\mu_B B}{\hbar} (g_J \mathbf{J} + g_I \mathbf{I}) \quad (2.3)$$

with Landé g -factors g_J and g_I listed in Table 2.1. Now including the electric quadrupole moment and nuclear spin terms, the full Hamiltonian is

$$H_B = A_{hf} \mathbf{I} \cdot \mathbf{J} + B_{hf} \frac{3(\mathbf{I} \cdot \mathbf{J})^2 + \frac{3}{2} \mathbf{I} \cdot \mathbf{J} - \mathbf{I}^2 \cdot \mathbf{J}^2}{2I(2I-1)J(J-1)} + \frac{\mu_B}{\hbar} (g_J m_J + g_I m_I) B, \quad (2.4)$$

where the first term is the nuclear-electronic spin interaction, the second term is the electric quadrupole interaction, and the last term is due to the atomic interaction with the external field. A full analytical treatment of the $2^2S_{1/2}$ energies and numerical calculation for the 2^2P states has been done for the full range of magnetic field values [66]. Here only the most relevant cases will be discussed.

For the $2S_{1/2}, |J = 1/2, F = 1/2, 3/2\rangle$ states, the second term in Eq. 2.4 is zero because $L = 0$, and to include all external field strengths, the energy states are written as a superposition of the $|F, m_F\rangle$ and $|m_I, m_J\rangle$ basis. This system is solved algebraically with splittings given by the Breit-Rabi formula,

$$E(m_F) = -\frac{\Delta E_{hf}}{2(2I+1)} + g_I \mu_B m_F B \pm \frac{\Delta E_{hf}}{2} \sqrt{1 + \frac{4m_F}{2I+1} x + x^2} \quad (2.5)$$

with $x = \frac{(g_J - g_I) \mu_B B}{\Delta E_{hf}}$ for $F = I \pm 1/2$ and for ground state $2S_{1/2}$, $\Delta E_{hf} = 228.20527$ MHz. The hyperfine energy splitting of the $2^2S_{1/2}$ states is described by the Breit-Rabi formula is shown in Fig. 2.2.

In the high-field regime, the Zeeman interaction term in eqn. 2.4 is much larger than the others, and the energies can be well approximated by

$$\Delta E = \frac{\mu_B}{\hbar} (g_J m_J + g_I m_I) B \quad (2.6)$$

using the $|J, m_J\rangle |I, m_I\rangle$ basis states. For each m_J , the allowed m_I states form a triplet with small energy splitting not accessible experimentally since $g_J \gg g_I$.

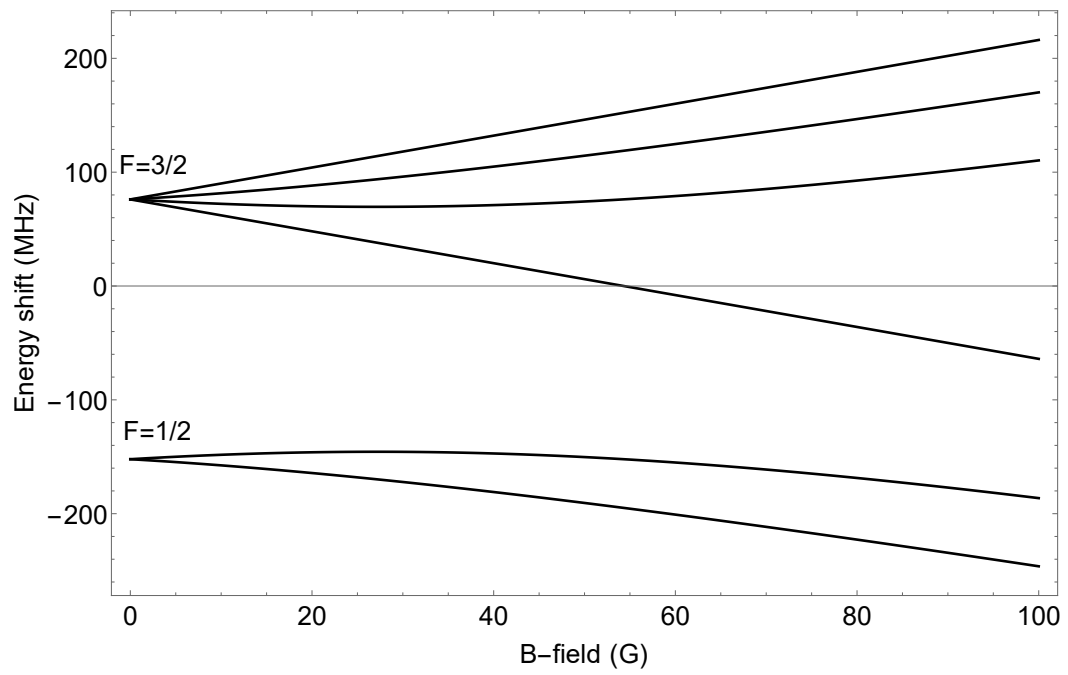


Figure 2.2. $2^2S_{1/2}$ hyperfine energy splitting description by the Breit-Rabi equation.

2.1.3 Optical Electronic Transitions

The interaction of atoms with external electric fields, including laser light can drive transitions in the optical range for near-resonant light via electric-dipole transitions. The transition is mediated by the interaction $H = -\boldsymbol{\mu} \cdot \mathbf{E}$, where $\boldsymbol{\mu}$ is the electric-dipole operator and \mathbf{E} is the electric field. The electric-dipole operator is a first-rank spherical tensor operator $\boldsymbol{\mu}_q^{(1)}$ with spherical basis labels $q = -1, 0, 1$ corresponding to light polarization σ^- , π and σ^+ respectively. The dipole matrix element for a transition between hyperfine states is $\langle F, m_F | \boldsymbol{\mu}_q^{(1)} | F', m'_F \rangle$ [67]. Using the Wigner-Eckart theorem, the transition matrix element is

$$\langle F, m_F | \boldsymbol{\mu}_q^{(1)} | F', m'_F \rangle = (-1)^{2F' - m_F + F + 1} \langle F || \boldsymbol{\mu}^{(1)} || F' \rangle \begin{pmatrix} F & 1 & F' \\ m_F & q & -m'_F \end{pmatrix} \quad (2.7)$$

where the term in the round brackets is the Wigner 3-j symbol and the term in double vertical bars is the reduced matrix element. The transition selection rules are $\Delta F = \pm 1, 0$ and $\Delta m_F = q$, which in eqn. 2.7 are enforced by the Wigner 3-j symbol. In the J basis the reduced matrix element is

$$\langle F || \boldsymbol{\mu}_q^{(1)} || F' \rangle = (-1)^{F' + I + J + 1} \sqrt{(2F + 1)(2F' + 1)} \begin{Bmatrix} J' & J & 1 \\ F & F' & I \end{Bmatrix} \langle J || \boldsymbol{\mu}^{(1)} || J' \rangle \quad (2.8)$$

where the term in braces is the Wigner 6-j symbol. Combining eqns. 2.7 and 2.8, the transition matrix elements are

$$\begin{aligned} \langle F, m_F | \boldsymbol{\mu}_q^{(1)} | F', m'_F \rangle &= (-1)^{3F' + J + F} \sqrt{(2F + 1)(2F' + 1)} \\ &\times \begin{pmatrix} F & 1 & F' \\ m_F & q & -m'_F \end{pmatrix} \begin{Bmatrix} J' & J & 1 \\ F & F' & I \end{Bmatrix} \langle J || \boldsymbol{\mu}^{(1)} || J' \rangle. \end{aligned} \quad (2.9)$$

with selection rules $\Delta J = \pm 1, 0$, $\Delta m_J = \pm 1, 0$, $\Delta L = 1$.

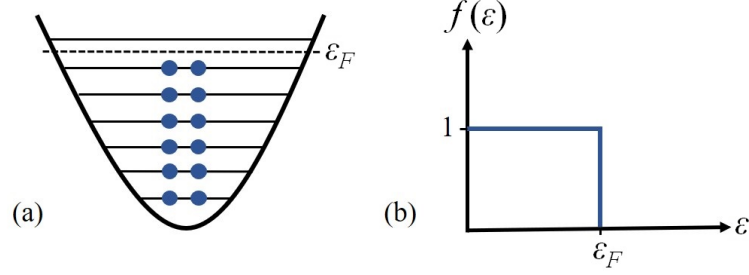


Figure 2.3. Degenerate Fermi gas energy characteristics. (a) Two-spin degenerate Fermi gas at zero temperature in a harmonic trap. (b) Fermi-Dirac distribution at zero temperature. At zero temperature the chemical potential equals the Fermi energy.

2.2 Properties of Trapped Fermi Gas

2.2.1 Ideal Fermi Gas in Harmonic Trap

When the phase-space density of a non-interacting Fermi gas is on the order of unity, quantum effects occur and the gas tends to degeneracy. The gas obeys Fermi-Dirac statistics, with the grand canonical ensemble treatment leading to the occupation distribution

$$f(E) = \frac{1}{e^{(E-\mu(N,T))/k_B T} + 1} \quad (2.10)$$

for each particle with energy $E = \mathbf{p}^2/2m + V(\mathbf{r})$, where $V(\mathbf{r})$ is the external trapping potential (as in Fig. 2.3(a)) and $\mu(N, T)$ is the chemical potential depending on total particle number N and temperature T .

At $T = 0$, the gas is in its ground state and the occupation distribution takes the values

$$f(E) = \begin{cases} 1 & E < E_F \\ 0 & E > E_F \end{cases} \quad (2.11)$$

as shown in Fig. 2.3(b). Here the chemical potential $\mu(N, 0)$ is the highest energy an occupied state can have, which is the Fermi energy E_F . Based on the Fermi energy, the Fermi temperature is given as $T_F = E_F/k_B$, and the Fermi wave vector

is $k_F = \sqrt{2mE_F/\hbar^2}$. These two quantities are used experimentally for determining degeneracy and interaction strength, respectively.

For an ideal Fermi gas in a harmonic trap with the potential

$$V(x, y, z) = \frac{m}{2}(\omega_x^2 x^2 + \omega_y^2 y^2 + \omega_z^2 z^2), \quad (2.12)$$

the density of states is $D(E) = E^2/2(\hbar\bar{\omega})^3$ with mean harmonic trap frequency $\bar{\omega} = \sqrt[3]{\omega_x\omega_y\omega_z}$. At $T=0$, the maximum number of particles is

$$N = \int_0^{E_F} D(E)dE, \quad (2.13)$$

which determines the Fermi energy as $E_F = (6N)^{1/3}\hbar\bar{\omega}$, as a function of the trap parameter $\bar{\omega}$ and number of particles.

2.2.2 Density Profile

The spatial density distribution of a Fermi gas is found by integrating the occupation distribution over momentum space. The integration at finite temperature $T \lesssim T_F$ in the Thomas-Fermi model [68] leads to

$$n(x, y, z) = \frac{-6N}{\pi^{3/2}\sigma_x\sigma_y\sigma_z} \left(\frac{T}{T_F}\right)^{3/2} \text{Li}_{3/2} \left[-\exp\left(\frac{\frac{\mu}{E_F} - \frac{x^2}{\sigma_x^2} - \frac{y^2}{\sigma_y^2} - \frac{z^2}{\sigma_z^2}}{T/T_F}\right) \right], \quad (2.14)$$

where $\text{Li}_{3/2}$ is a polylogarithmic function and the Thomas-Fermi radius $\sigma_i \equiv \sqrt{2E_F/m\omega_i^2}$, is a measure of the degenerate cloud size, corresponding to the distance from the center of the trap to the distance where $E_F = V(\boldsymbol{\sigma})$.

At higher temperatures, the gas is well described by the Boltzmann distribution with density [68]

$$n(x, y, z) = \frac{N}{\pi^{3/2}\sigma_x\sigma_y\sigma_z} \left(\frac{T}{T_F}\right)^{3/2} e^{-\frac{x^2}{\sigma_x^2} - \frac{y^2}{\sigma_y^2} - \frac{z^2}{\sigma_z^2}}. \quad (2.15)$$

As seen in eqns. 2.14 and 2.15, the density profile of the harmonically trapped gas is dependent on the degeneracy parameter T/T_F , atom number and cloud size. Details on how to extract the cloud parameters from fitting functions using absorption imaging are given in in Sec. 3.8.3.

2.3 Ultracold Atoms Interactions

Part of what makes the trapped atomic gas system versatile for simulation of disparate phenomena is the tunability of interactions. Here we can tune not only the strength, but also whether the interaction is attractive or repulsive by tuning a bias magnetic field strength to control a Feshbach resonance between two fermions of opposing spins. This can be done experimentally in ultracold atom systems optically or magnetically. In this section the magnetic control of the Feshbach resonance is presented, with focus on ${}^6\text{Li}$ atoms.

2.3.1 s -wave Scattering

Described here is a simplified quantum mechanical model used for elastic collisions between two hard spherical particles in the low-energy regime with momentum $k \rightarrow 0$. This scattering is treated in the center-of-mass frame with reduced mass $m_r = m_1 m_2 / (m_1 + m_2)$. For an incoming particle described by a plane wave $\psi_{k,in} \propto e^{ikz}$, the scattered wavefunction from a spherically symmetric potential with finite range r_0 at large distances $r \gg r_0$ is

$$\psi_{k,sc}(\theta, r) \propto e^{ikz} + f_k(\theta) \frac{e^{ikr}}{r}, \quad (2.16)$$

where $f_k(\theta)$ is the scattering amplitude and theta the angle between z and \mathbf{r} . For a spherically symmetric potential, the Schrödinger equation for the radial component $R(r)$ of the wavefunction is simplified in the form

$$-\frac{\hbar^2}{2m_r} \frac{d^2 u(r)}{dr^2} + \left[V_{int}(r) + \frac{\hbar^2 l(l+1)}{2m_r r^2} \right] u(r) = E u(r), \quad (2.17)$$

with $u(r) \equiv rR(r)$. The second term in brackets is the centrifugal barrier term which vanishes for s -wave collisions with $l = 0$ in the partial wave expansion. Now expanding the scattered wavefunction in terms of angular momentum l using Legendre polynomials $P_l(\cos(\theta))$, the scattering amplitude in Eq. 2.16 is [69]

$$f_k(\theta) = \frac{1}{2ik} \sum_{l=0}^{\infty} (2l+1) (e^{2i\delta_l(k)} - 1) P_l(\cos(\theta)) \quad (2.18)$$

and $\delta_l(k)$ is the phase shift acquired by a partial wave due to scattering. In the s -wave scattering regime, keeping only the first term ($l = 0$) of the partial wave expansion,

$$f_k = \frac{1}{k \cot(\delta_0(k)) - ik}, \quad (2.19)$$

where now the scattering amplitude is independent of θ . For $k \rightarrow 0$, $\delta_0(k)$ can be expanded so that up to second order [70]

$$k \cot(\delta_0(k)) = -\frac{1}{a} + \frac{1}{2}k^2 r_e, \quad (2.20)$$

where a is the scattering length, which is a measure of the scattering sphere diameter, and r_e is the effective range of the scattering potential, which is on the order of the interatomic potential r_0 [71]. Keeping only the first term in Eq. 2.20 and using the relation between differential scattering cross-section and the scattering amplitude

$$\frac{d\sigma}{d\Omega} = |f_k(\theta)|^2, \quad (2.21)$$

the scattering amplitude is found by integrating over the solid angle and given as

$$\sigma = \frac{4\pi a^2}{1 + k^2 a^2} = \begin{cases} 4\pi/k^2 & ka \gg 1 \\ 4\pi a^2 & ka \ll 1 \end{cases} \quad (2.22)$$

The interaction parameter ka defines the strength of interactions with $ka \ll 1$ as the weakly interacting regime that makes the scattering cross-section independent of k . For strong interactions with $a \rightarrow \pm\infty$, the gas reaches the unitarity limit, where $a \gg r_0$.

2.3.2 Feshbach Resonance

Tuning of interaction strength in cold atoms systems is due to the resonant enhancement of the scattering length through a Feshbach resonance. The theoretical treatment of the scattering length enhancement includes what is termed the “open-channel”, which is the scattering between two atoms of the same spin state $|m_s\rangle$ ($\uparrow\uparrow$) forming a spin triplet and a “closed-channel” for the spin singlet system ($\uparrow\downarrow$). A

full description of Feshbach resonance in alkali atoms can be found in Refs. [16, 72]. The molecular potential through which the s -wave scattering happens is dependent on the internal spin of the scattering atoms. As seen in Fig. 2.4(a) the spin singlet potential has a higher entrance energy with available bound state with energy closer to the the open channel continuum. The energy difference between the two collision channels is tunable via the magnetic moment difference between the two channels. The Zeeman effect tunes the energy of hyperfine states as a function of magnetic field strength, which gives the energy difference as $\Delta E = \Delta\mu \cdot B$. The resonance occurs when the entrance energy of the open channel is tuned to a bound state energy in the closed channel. Tuning ΔE controls the magnitude and sign of the scattering length as shown in Fig. 2.4(b). If the bound state energy is lower than the triplet entrance, the scattering length is positive and the system is in the BEC side where loosely bound diatomic molecules can form with binding energy $E_b = -\hbar/ma^2$. If the bound state energy is higher than the triplet entrance energy, then a is positive and the system is in the BCS side where Cooper pairs are formed. In the unitarity region, $(k_F|a|)^{-1} \rightarrow 0$ between the BEC and BCS regions, where the scattering length $a \rightarrow \pm\infty$, the pair size is on the order of the interparticle spacing [73].

2.3.3 Tuning Interactions

In ${}^6\text{Li}$ experiments, the Feshbach resonances between the three lowest energy states are used, with magnetic fields above 30 G considered a high field where the energy estates are treated in the $|m_s, m_I\rangle$ basis with all the lowest states with $m_s = -1/2$ having only a different nuclear spin projection. A relative ease of tuning the scattering length with magnetic field strengths is achievable with water-cooled magnet coils to include a weakly attractive interaction, zero crossing and the unitarity region for the $|1\rangle$ - $|2\rangle$, $|2\rangle$ - $|3\rangle$ and $|1\rangle$ - $|3\rangle$ resonances. ${}^6\text{Li}$ Feshbach resonances have an overlap, partly due to the broadness of the resonances along with their positions as shown in Fig 2.5(b). This allows for the creation of strongly interacting to weakly interacting

gases without a magnetic field sweep, and instead using RF-excitation to flip the atomic state.

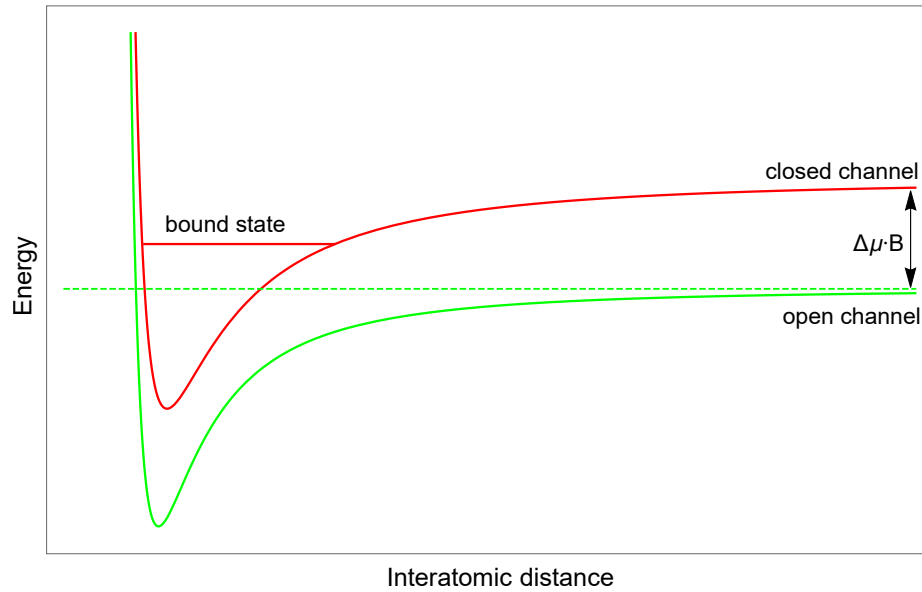
For ${}^6\text{Li}$, the tuning of the energy difference between the continuum of the open channel with spin $S = 1$ and the bound state in the closed channel with $S = 0$ is $\Delta E \approx 2\mu_B\Delta S = h \times 3 \text{ MHz/G}$ and the scattering length is tuned around the resonance center as [74]

Table 2.2.
 ${}^6\text{Li}$ Feshbach resonance parameters, values taken from Ref. [74].

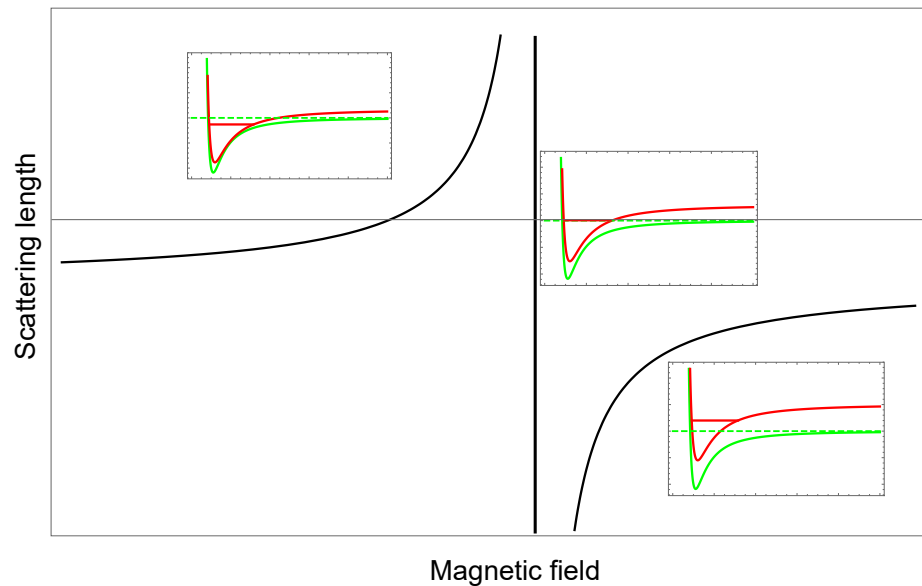
Scattering states	$a_b(a_0)$	$\Delta(G)$	$B_0(G)$	$\alpha(G^{-1})$
$ 1\rangle\text{-} 2\rangle$	-1405	300	834.149	0.0011
$ 2\rangle\text{-} 3\rangle$	-1490	222.3	811.22	0.001
$ 1\rangle\text{-} 3\rangle$	-1727	122.3	690.43	0.0012

$$a(B) = a_{bg} [1 - \Delta B / (B - B_0)] (1 - \alpha(B - B_0)), \quad (2.23)$$

where a_{bg} is the background scattering length, B_0 is the field where the resonance occurs, ΔB is the resonance width and α is an experimentally determined parameter. The numerical values used in Eq. 2.23 are listed in Table 2.2.

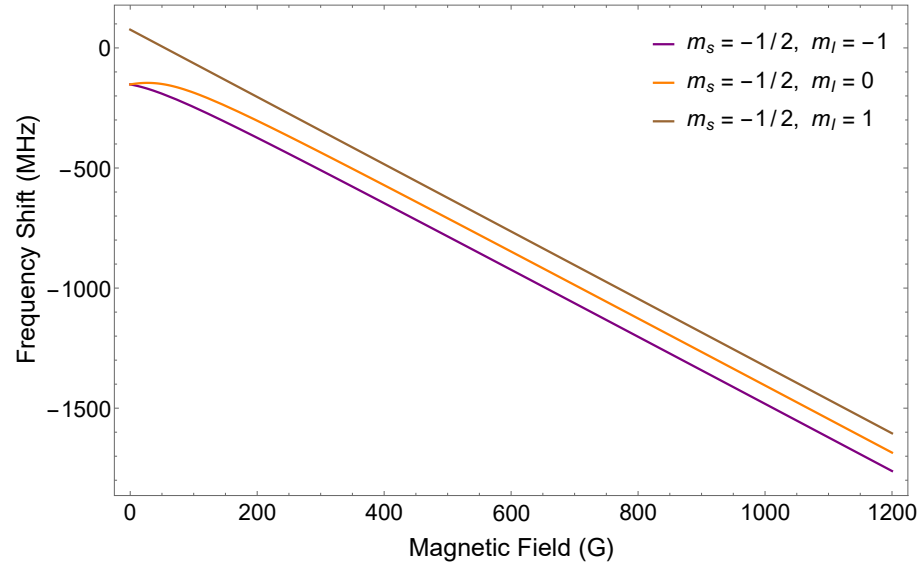


(a)

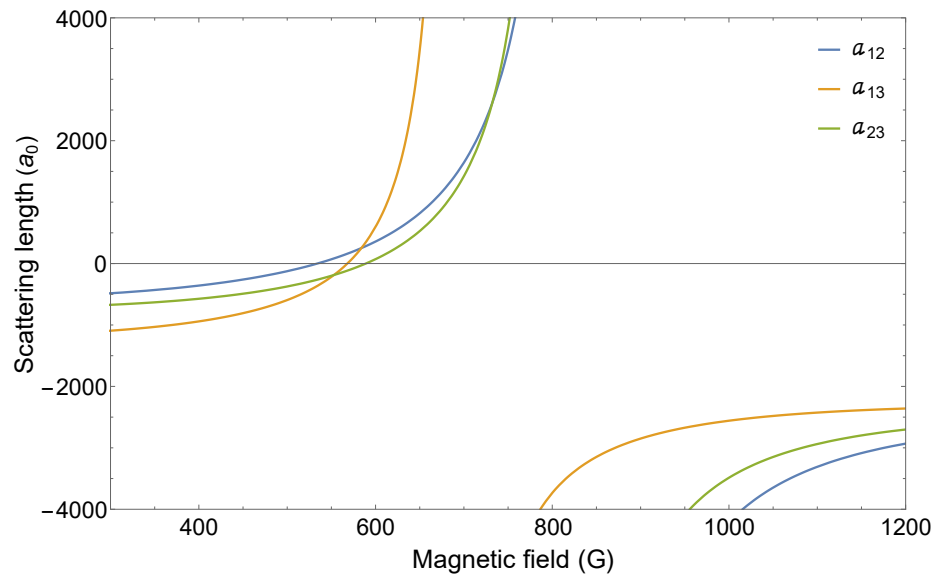


(b)

Figure 2.4. Two-channel Feshbach resonance of scattering length. (a) Lennard-Jones like potentials for the two-channel Feshbach resonance model. The resonance occurs when the open channel entrance energy is tuned to a bound state in the closed channel. (b) The scattering length enhancement as function of magnetic field. The insets show the BEC region for $a < 0$, the BCS region at $a > 0$ and the unitary region for $a \rightarrow \pm\infty$.



(a)



(b)

Figure 2.5. Energy states and Feshbach resonance profiles for ${}^6\text{Li}$. (a) Energy shifts due to applied magnetic field for the three lowest energy states of ${}^6\text{Li}$. (b) Scattering length dependence on magnetic field in terms of the Bohr radius for the lowest spin states. The narrow Feshbach resonance centered at 543 G for $|1\rangle$ - $|2\rangle$ is not pictured.

3. EXPERIMENTAL APPARATUS

Cold atom research uses many experimental techniques and instrumentation first developed in other fields of physics and engineering. Some of the research techniques include ultra-high vacuum (UHV), laser frequency locking, generation and precise control of magnetic fields, and digital instrument timing control. In the parametric cooling experiments in this thesis, all of the above techniques must come together to produce a stable optically trapped gas of ^6Li atoms at temperatures below $1\ \mu\text{K}$. This chapter describes the design, assembly, and operation of the apparatus built for my research.

3.1 Vacuum System

The apparatus used in the parametric cooling experiments requires the ^6Li source to be kept under UHV while no experiments are being performed and to generate an atomic beam at temperatures around 450°C while the experiments are conducted. Also required are a Zeeman slower for decelerating atoms from the atomic source, space for mounting magnet coils used to generate magnetic fields, and optical access for the slowing, MOT, and ODT beams. Due to the UHV requirements, all of the tubing and CF flanges used for connecting tubing and viewports are made from either 304 or 316 stainless steel. A schematic of the vacuum part of the apparatus is in Fig 3.1.

3.1.1 Design

On the oven side of the vacuum system pictured in Fig. 3.2, a gas tubing entrance that is closed off using an inline valve is included for argon gas loading of the system

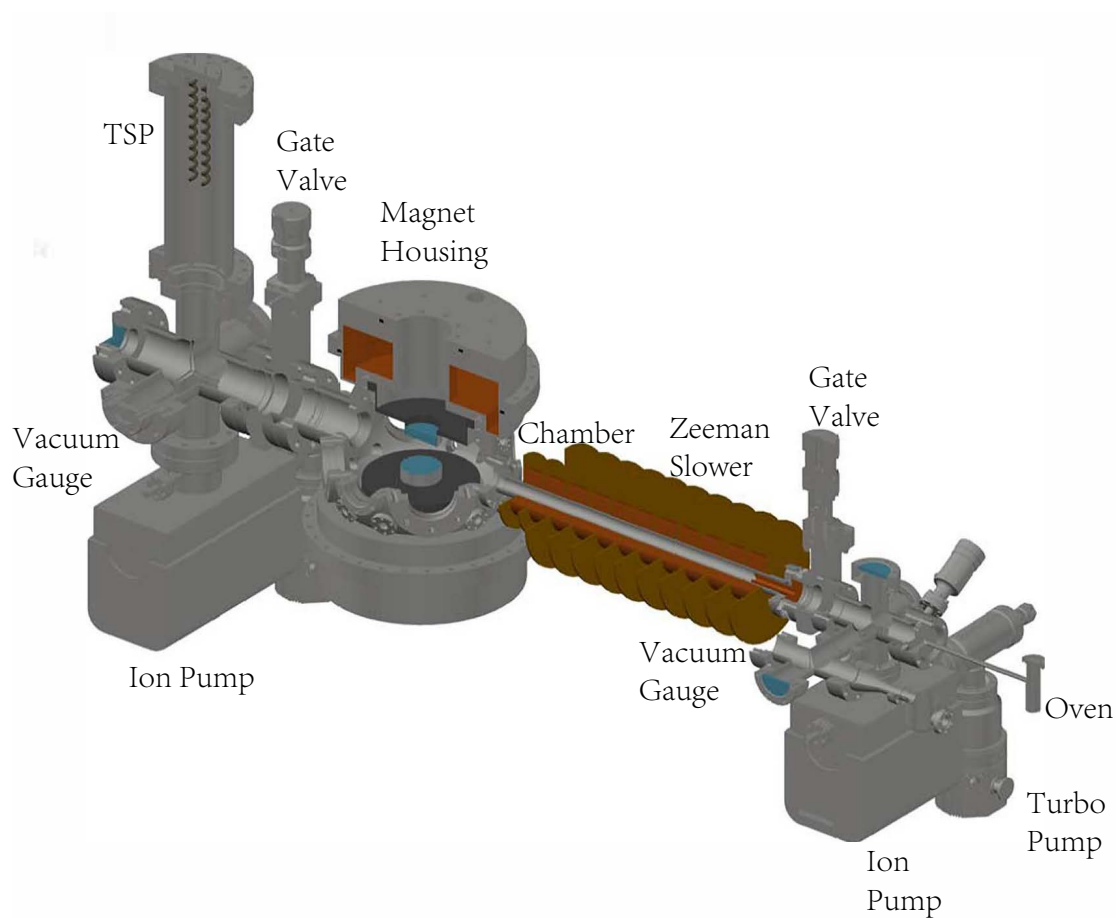


Figure 3.1. Vacuum system design. Not pictured is the non-evaporable getter material.

required during installation of the oven to reduce lithium contamination. During UHV operation of the system, a 40 liter/s (Gamma Vacuum 45s) ion pump is used to keep the vacuum on the oven side at vacuum two orders of magnitude lower than the chamber side. For low vacuum operation, a turbomolecular pump backed by a rotary vane pump is attached to the ion pump via an all-metal valve. As a safety measure, there is a gate valve installed before the Zeeman slower to protect the lithium in case of a vacuum problem on the science chamber side.

While the oven is in operation and lithium gas flows out, the vacuum is lowered on this side, but cannot affect the science chamber side, so there is a differential pumping tube of 7 mm diameter to keep a vacuum difference between the two sides. Between the oven side and the science chamber, a Zeeman slower with a decreasing magnetic field profile and forced-air cooling mounted on a 50 cm long tube that is attached to one of the 2.75" ports the science chamber. Following the oven nozzle, a viewport shutter with electronic control is used to block the atomic beam if needed to reduce coating on the viewport used for the slowing beam.

The science chamber is a Kimball Physics MCF800-SphSq customized with a 2.55" diameter tube on the opposing side of the Zeeman slower to increase the pumping efficiency between the chamber and vacuum pumps. The chamber side contains a six-way tee to attach all the instrumentation and viewports required for operation of the system. A 75 liter/s (Gamma Vacuum 75s) ion pump, a titanium sublimation pump (TSP), and some NEG (Non-Evaporative Getter) strip inside one of the sides of a six-way tee are used for vacuum pumping. The vacuum is measured by a hot-cathode gauge (Varian UHV-24), along with the gauge included with the ion pump. A viewport is installed on the opposing side of the chamber, to allow the slowing beam to pass through the chamber and be used with the Zeeman slower. As a safety precaution in case of loss of vacuum in the six-way tee side, a gate valve is installed between the six-way tee and the science chamber.

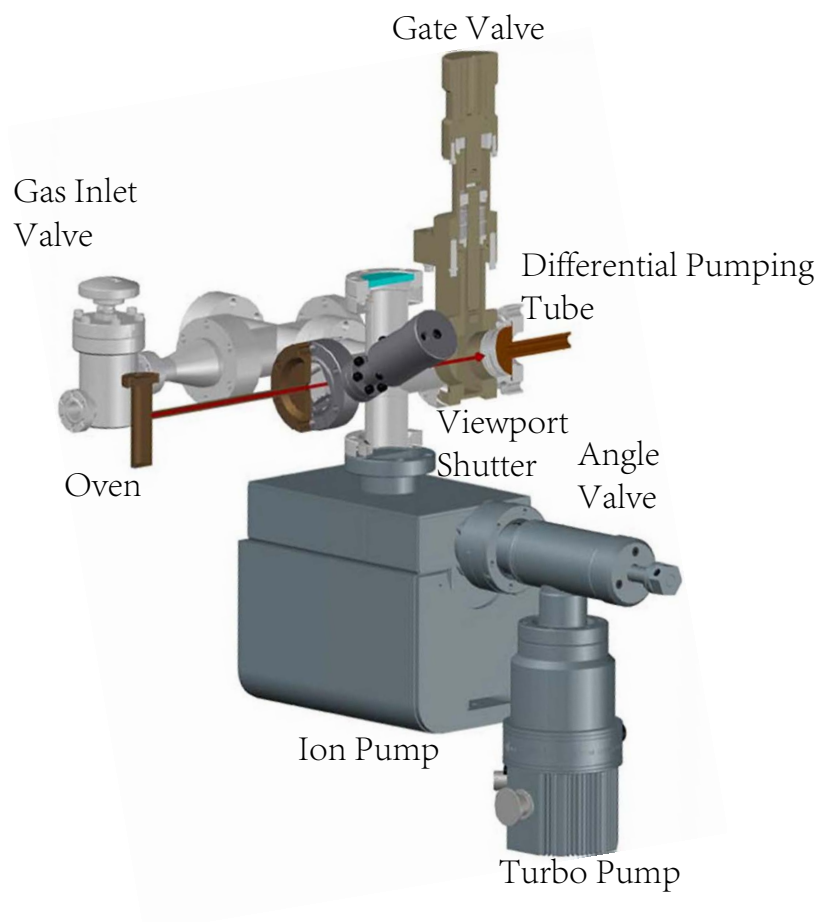


Figure 3.2. Oven side vacuum setup. The arrow indicates the atomic beam from the oven. An angle valve used during loading of ${}^6\text{Li}$ into the oven is shown to the left of the oven. An all-metal angle valve is used to connect a turbo pump into the system during initial pumping stages and baking. The differential pumping tube shown in copper color is used to keep the science chamber side at higher vacuum.

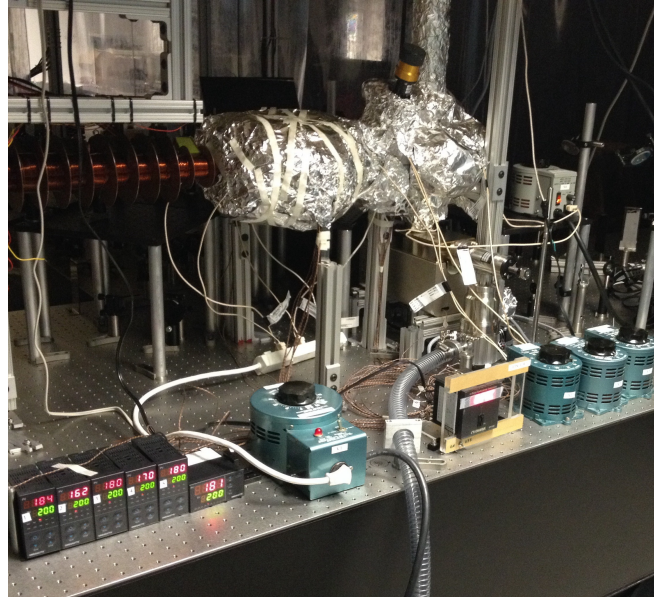


Figure 3.3. Vacuum system baking. Only the science chamber side is pictured; the same method of heating with heat tapes and aluminum foil was performed on the oven side.

3.1.2 Preparation

The vacuum system is mounted on slotted aluminum framing with some special homemade mounts for the chamber mounted on two of the 2.75” ports for extra support due to the weight of the top coil that is mounted on the chamber.

To reach the desired 10^{-11} Torr vacuum, a bake-out was performed at 200 °C for two weeks, including using the built-in heater on the ion pumps, and using the turbomolecular and rotary vane pumps, since the vacuum drops to around 10^{-5} Torr. The bake-out process (shown in Fig. 3.3) is necessary to remove contaminants on the inside surfaces of the vacuum parts that would otherwise outgas during the experiments and not allow a final vacuum of 10^{-11} Torr to be reached. The bake-out also acts to activate the NEG material inside the six-way tee.

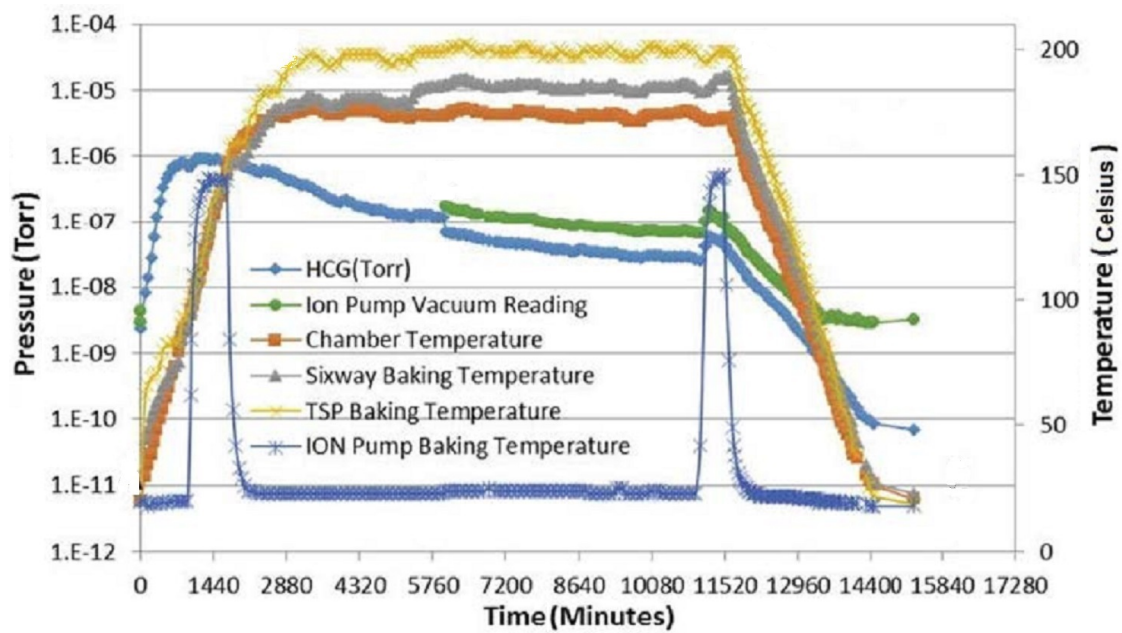


Figure 3.4. Pressure and temperature curves during bakeout.

3.1.3 Performance

Prior to the bake-out, the equilibrium vacuum in the system reached 3×10^{-9} Torr, which is not enough vacuum for experiments. During the bake-out, vacuum as low as 10^{-6} Torr was reached during the initial outgassing as the temperature reached 150° . After the bake-out and TSP use, the final vacuum reached 1.3×10^{-11} Torr, as seen in Fig. 3.4. This vacuum is roughly kept on the science chamber side, as experiments are being performed with the ${}^6\text{Li}$ beam out of the oven reducing the vacuum on the oven side to 3.9×10^{-9} Torr.

This UHV has been kept for the five years that apparatus has been used, with the only problem being a malfunction of the inline valve on the oven side which lowered the vacuum by about a factor of 10 on the oven side, but has not affected the chamber side.

3.2 ${}^6\text{Li}$ Oven

The volatility of lithium when in contact with air requires special care when handling it. Before loading about 3 grams of ${}^6\text{Li}$ to the oven, small pieces of lithium that were kept in mineral oil were rinsed with acetone while in a glovebox filled with argon.

The design of the oven must consider the experimental requirements of producing a flux of lithium collimated to reach the science chamber, with velocity in the proper range that can be used with a Zeeman slower and with enough lifetime for experiments to be conducted. The oven used for the experiments in this thesis follow the design of Ref. [75]. As shown in Fig. 3.5(a), the lithium is loaded into the vertical cylinder through a 1.33" flange on the top, and installed to the apparatus with a 2.75" rotatable flange. To seal the oven, on the 1.33" flange a nickel gasket is used because of its higher temperature rating to prevent any vacuum leaks due to heating the oven.

To increase the lifetime of the oven, a stainless steel mesh is used to line the inside of the reservoir and nozzle to incorporate the "wicking" effect that allows any of the

Table 3.1.
Operating temperatures of the oven sections.

Section 1	Section 2	Section 3	Section 4	Section 5
340°C	340°C	430°C	400°C	360°C

lithium that does not make it out of the nozzle to flow back into the reservoir. At the end of the nozzle, the temperature is kept high enough to ensure that any liquid lithium can flow back into the reservoir.

Five independent heating sections are used for heating the oven. Each section is composed of several turns of nichrome wire that are independently controlled by a current supply circuit for heating, as shown in Fig. 3.5(b). Each heating section is monitored by a K-type thermocouple, with the temperature for each section set for optimal MOT loading and oven lifetime. The current on each nichrome wire (Omega, NI80-020-200) section is commanded on a keyboard through a microcontroller (ATmega16), through a digital to analog converter (DAC7715) to control the gate voltage on the MOSFETs (IRFP4368). The operational temperatures optimized for the experiments are listed in Table 3.1.

3.3 Laser Cooling and Trapping

Starting with a beam of atoms with velocities up to 1100 m/s, cooling of the atoms is necessary before trapping can be realized. Resonant light scattering is used for laser cooling of the atomic beam by a Zeeman slower, which, along with a counter propagating laser beam, slows the atoms down to be captured by the MOT. At the MOT stage, the temperature and phase-space density ($\sim 10^{-5}$) are not adequate for the formation of a degenerate Fermi gas. Therefore a conservative potential in the form of an ODT is applied to further lower the temperature of the trapped atoms and increase the phase-space density.

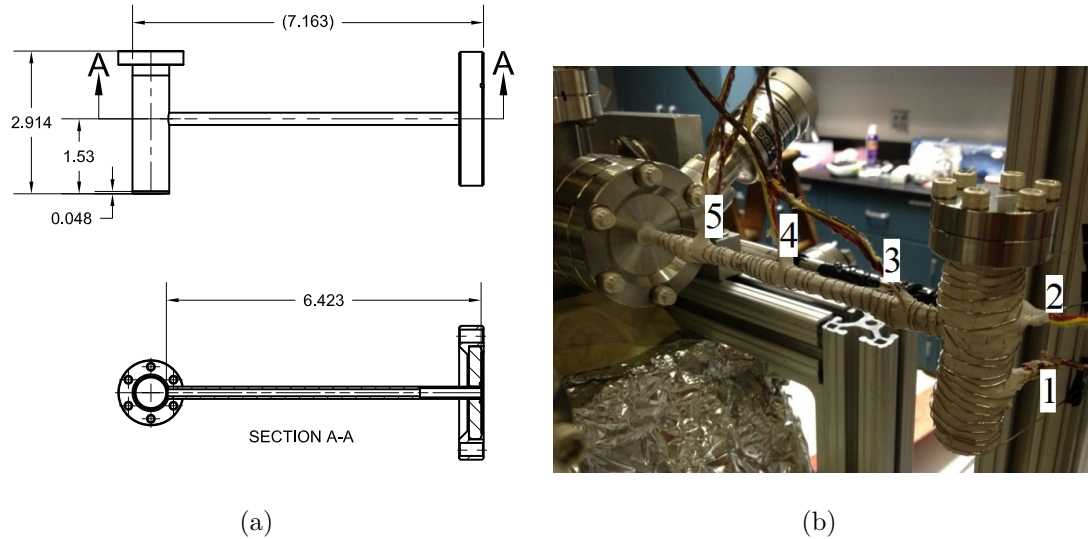


Figure 3.5. Lithium oven design and implementation. (a) ${}^6\text{Li}$ oven design with a rotatable flange on the oven nozzle and 1.33" flange on the top for lithium loading. (b) Oven mounted on apparatus with heating sections. Layers of high-temperature cement are used to separate the nichrome wires from the thermocouples.

3.3.1 Zeeman Slower

A moving atom encountering a counterpropagating beam of photons with energies resonant with an atomic transition will absorb a photon and gain its momentum, then subsequently spontaneously emit a photon in a random direction. As many photon scatterings occur, a net momentum decrease slows down the atom, leading to a cooling effect. The maximum force associated with the deceleration of the atoms is $F_m = \hbar k \Gamma / 2$, where $\hbar k$ is the momentum of the photons and Γ is the decay rate of the atomic transition. As the atoms decelerate, they will fall out of transition with the incoming photons and the deceleration will cease, unless a scheme to keep the incoming photons on resonance is implemented.

Using a spatially varying magnetic field to induce a Zeeman shift on the transition energies of the moving atoms, a single frequency counterpropagating laser beam can be kept on resonance with the atoms to cause a velocity decrease of nearly two orders

of magnitude [76]. To keep the atoms decelerating as they travel down the Zeeman slower, the total detuning from resonance must be

$$\delta = \delta_0 + v/\lambda - \frac{\Delta\mu B(z)}{h} \quad (3.1)$$

where δ_0 is the detuning at zero-field for an atom at rest, λ is the wavelength of the laser light, and $\Delta\mu$ is the change in magnetic moment from the ground to excited states. Our Zeeman slower operates on the $2^2S_{1/2} |m_s = 1/2, m_I = \pm 1, 0\rangle \leftrightarrow 2^2P_{3/2} |m_J = 3/2, m_I = \pm 1, 0\rangle$ transitions, so $\Delta\mu = \mu_B$. The magnetic field profile required to keep the laser light on resonance with the constantly decelerating atoms is then

$$B(z) = \frac{h}{\mu_B} \left(\delta_0 + \frac{1}{\lambda} \sqrt{v_i^2 - 2az} \right) \quad (3.2)$$

where v_i is the velocity of an atom entering the slower and a is the constant deceleration.

The slower has a decreasing magnetic field profile with eleven separate coil winding sections made with 14 AWG wire and connected in series to a power supply to provide the operating current of 10.6 A. The coils are wound on a 50 cm long, 2.1cm inner diameter stainless steel tube as shown in Fig. 3.7. Each coil has 22 horizontal windings and is separated by a 1.3 cm thick copper plate that is soldered onto the tube to increase heat dissipation from the coils. Fan cooling is used to keep the coils from overheating since the estimated power consumption is 200 W during operation. The simulated and measured magnetic field curves are shown in Fig. 3.6.

The slowing beam has about 100 mW of σ^+ with a beam diameter of about 20 mm light generated by a Toptica TA 100. The beam has $\delta_0 = 192$ MHz generated by an AOM in double-pass configuration. The measured velocity of the slowed atoms at the center of the MOT is 100 m/s.

3.3.2 671 nm Laser Systems

To generate the laser light used in the slowing beam and MOT beams, a Toptica TA 100 with 450 mW output power is used, and a Toptica DL Pro with about 25 mW

Table 3.2.
Zeeman slower coil vertical windings.

Section	1	2	3	4	5	6	7	8	9	10	11
Windings	18	13	13	12	11	10	9	8	7	6	6

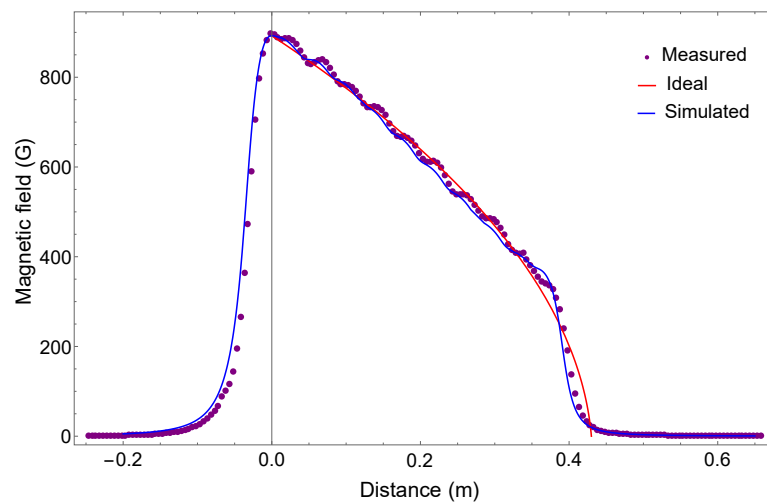


Figure 3.6. Zeeman slower magnetic field profile. A current of 9.6 A was used in all cases.

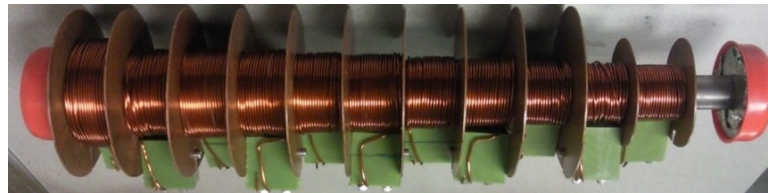


Figure 3.7. Zeeman slower. The left flange is mounted to the oven side and right flange is mounted on the science chamber giving the slower a decreasing magnetic field profile.

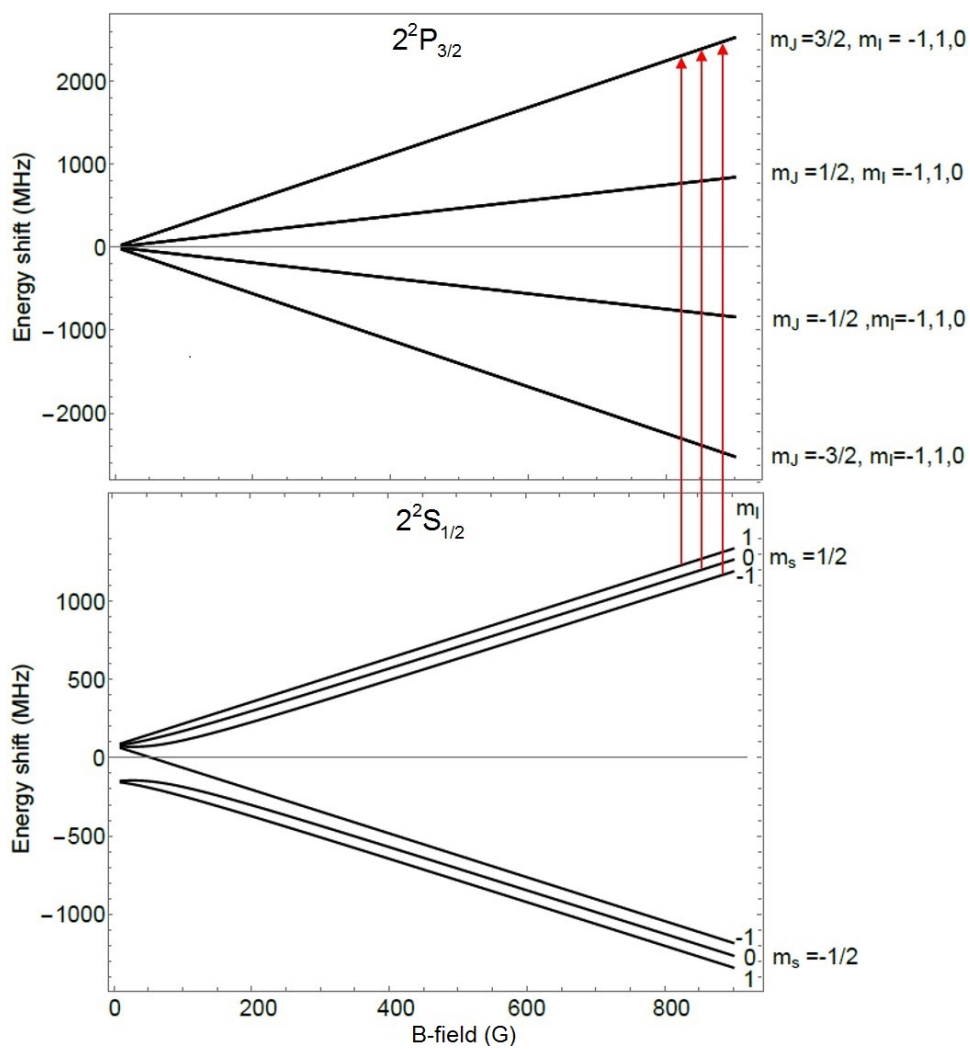


Figure 3.8. Electronic transitions used with the Zeeman slower.

output is used for the imaging beam. These are ECDLs (the TA 100 uses a tapered amplifier) with tunable single frequency outputs meeting the required linewidth and power outputs required, and can be stabilized and locked for hours. The TA 100 operates locked to the D_2 line, with frequency shifts required by the MOT and slowing beams provided by AOMs (Isomet, 1204C). The DL Pro beam frequency for imaging requires a large frequency shift for imaging atoms at various interaction strengths. An offset-locking system described in Sec. 3.3.3 is used for imaging the atoms for various magnetic field strengths.

In the optical setup of the beams generated by the TA 100, after the optical isolator only 380 mW is left for all usage, with 150 mW used for the Zeeman slower and the rest going to the MOT beams. Fig. 3.9(a) shows the optical layout for the slowing and MOT beam generation.

The MOT beams contain a cooling beam and a repumping beam. The cooling beam gets 2/3 the total MOT beam power with the rest used for the repumping beam for all phases of the MOT process. The repumping beam has a frequency upshift of 228 MHz from the cooling beam at all times to repump the atoms that fall out of resonance with the cooling beam back to the cycling transition. The slowing beam has 100 mW and is σ^+ polarized with an initial detuning of 192 MHz from the D_2 line done with a double-pass configuration with an AOM.

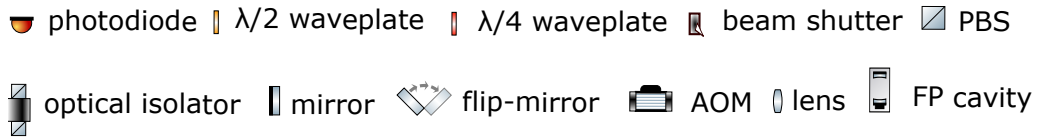
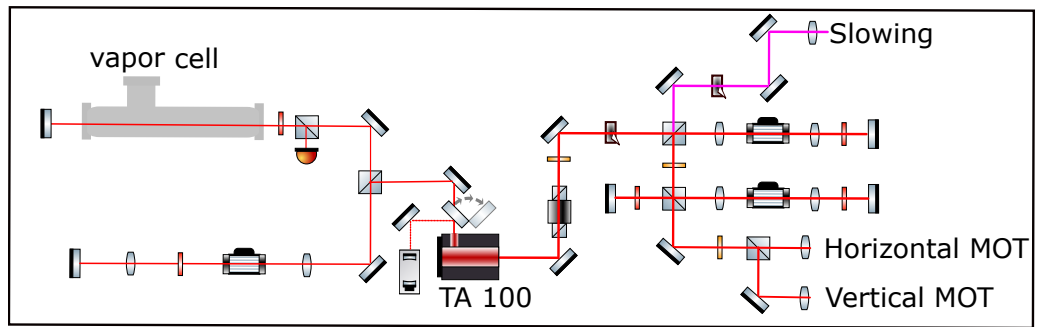
The DL Pro power is split between the offset-locking setup and the imaging beam, with most of the power going to the imaging beam. On the imaging beam optical path, the beam is first frequency shifted by an AOM in double-pass configuration. This is used in low magnetic field imaging requiring frequency shifts of less than about 100 MHz and in switching the imaging atoms from $|1\rangle$ to $|2\rangle$. Then the beam is linearly polarized and launched into a polarization- maintaining fiber that exits the fiber and is circularly polarized σ^- to excite the $2^2S_{1/2} |m_s = -1/2\rangle \rightarrow 2^2P_{3/2} |m_s = -3/2\rangle$ transitions for absorption imaging. The optical layout for the DL Pro is shown in Fig. 3.12.

3.3.3 671 nm Lasers Frequency Locking

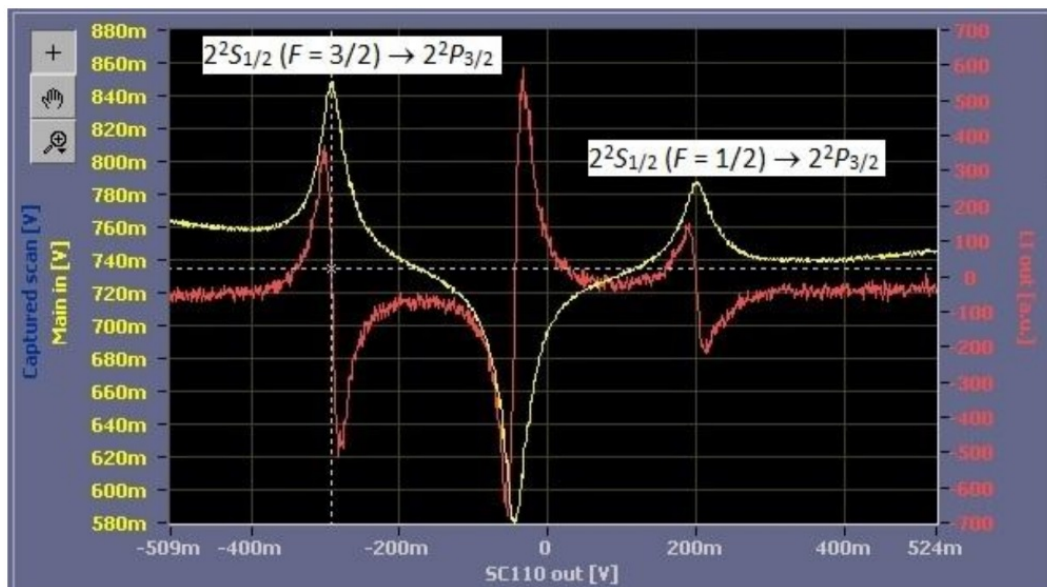
The laser output frequency of TA pro needs to be locked at the frequency required by the Zeeman reducer laser. This is achieved using laser current modulation [77] using the reference beam output from the TA, which has about 2 mW. The frequency is locked using Doppler-free saturated absorption spectroscopy [78] with a ${}^6\text{Li}$ vapor cell. The optical setup used in our locking system is shown in Fig. 3.9(a). Laser current modulation of the pump and probe beams is done via the Digilock 110 module with a modulation amplitude of 800 KHz and modulation frequency of 100 KHz. After passing the vapor cell, the probe beam is detected by a photodiode and the signal is demodulated with the Digilock 110 module to produce the error signal used for the frequency locking. The error signal goes to two separate control feedback loops after passing through a low-pass filter: one controls the piezotransducer in the external cavity of the diode laser and the other goes to the current control. The laser frequency is locked to the $2^2S_{1/2} |F = 3/2, m_F = 3/2\rangle \rightarrow 2^2P_{3/2} |F = 5/2, m_F = 5/2\rangle$ transition. A linewidth of approximately 800 kHz is obtained, and is monitored using a Fabry-Perot cavity. The beam from the TA Pro amplified beam is then used as the reference signal to offset-lock the DL Pro frequency. Frequency locking signal from the Digilock module is shown in Fig. 3.9(b).

The pump and probe beams' frequencies are upshifted with an acousto-optical modulator (AOM) set in a double-pass configuration for the Zeeman slower required shift. The probe beam diameter is slightly smaller than the pump beam to ensure that all the atoms in the path of the probe beam have been pumped into an excited state.

The vapor cell used in the Doppler-free saturated absorption spectroscopy has a stainless steel tee structure with a 50 cm long tube of 6.35 cm diameter with CF flanges on either end, as seen in Fig. 3.10. On other side of the tee, an angle valve (MDC 31209) is used for filling the vapor cell with argon and sealing. The solid lithium is loaded into the center of the pipe and 20 mTorr of argon fills the pipe. Heat tape is



(a)



(b)

Figure 3.9. Frequency locking and beam generation for the slowing and MOT beams. (a) TA 100 optical layout for frequency locking, slowing, and MOT beams. (b) Locking signal from Digilock. The yellow curve is the signal from the probe beam and the red curve is the error signal.



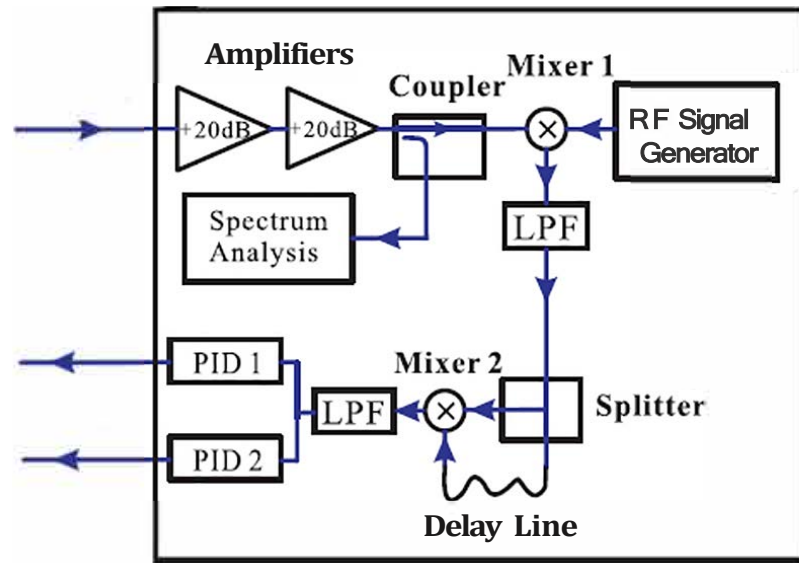
Figure 3.10. Vapor cell used for TA 100 frequency locking.

used to keep the cell operating at 340 °C, with the tape wound in a configuration to minimize the magnetic field produced by applied current on the wires.

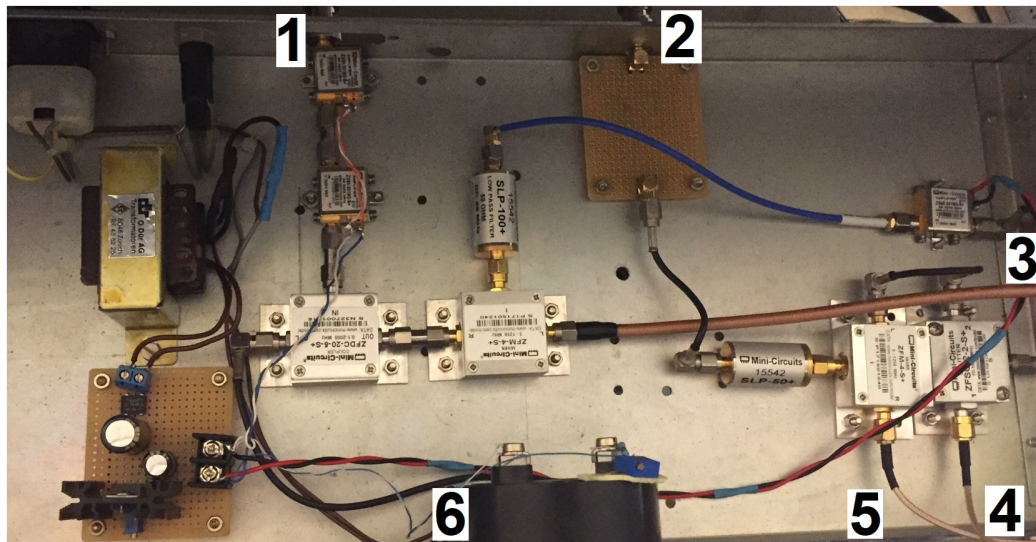
Absorption imaging of the atomic cloud requires a beam at frequency resonant with the atoms for detection. To cover the range of interactions used in experiments, requires using magnetic fields up to 1000 G, which due to Zeeman shifts in the energy states of the atoms would cause the transition frequency needed for imaging to shift up to 1.5 GHz. Here we use an offset-locking technique to shift the DL Pro output frequency in reference to the locked TA 100 signal [79], with the design shown in Fig. 3.11(a) and the experimental setup shown in Fig. 3.11(b). The DL Pro and TA 100 signals are first coupled into an optical fiber, with the beat signal between them detected by an avalanche photo-detector. Our setup has a frequency switch response time of 2.5 ms for the 1.5 GHz range.

The applied magnetic fields used to tune interaction between $|1\rangle$ - $|2\rangle$ atoms, causes Zeeman shifts to the hyperfine energy levels that must be accounted for in the imaging beam. At a field of 841 G, the shift in imaging transition frequency is around 1.1 GHz, which makes the use of offset locking a good option [79].

Fig. 3.12 shows the optical layout of the imaging beam. The AOM used with a maximum shift of about 100 MHz is used for fast switching of low frequencies. After the AOM double-pass, the beam is coupled with the reference beam of the TA 100 through a PBS, passed through a quarter-waveplate, and sent into a polarization-maintaining fiber (Thorlabs, P3-630PM-FC-5). The beams exiting the fiber are de-



(a)



(b)

Figure 3.11. Offset-locking schematic and electronic circuit. (a) Offset-locking diagram. The input is the signal from the photodiode and the outputs go to the piezotransducer and current controls of the DL Pro. (b) Offset-locking electronics. 1: photodiode in, 2: PIDs out, 3: signal generator in, 4: delay line in, 5: delay line out, 6: spectrum Analyzer out.

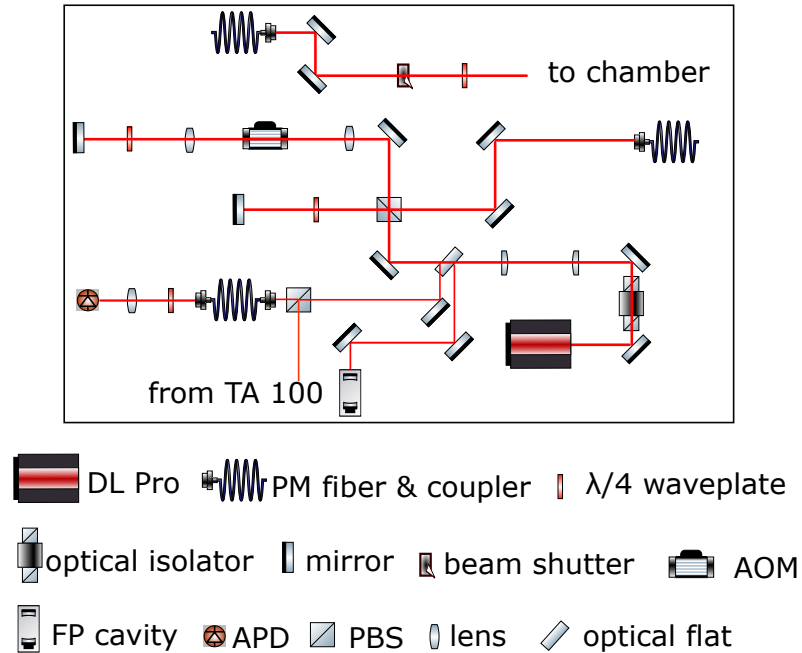


Figure 3.12. Optical layout for the imaging beam from DL Pro.

tected by an avalanche-photodiode (Newport, 877) that sends a signal to the offset locking circuit. The beat signal between the locked TA 100 frequency and the DL Pro is mixed with a frequency from the function generator (Agilent, E4422B). This signal is then split into two: one goes through a delay line and picks up a phase difference from the other signal. After a low-pass filter, a frequency-dependent DC error signal is generated and used with a PID to lock the frequency of the DL PRO. The offset-locking system has a response time 2.5 ms and a laser line width of about 500 kHz.

3.3.4 MOT

After the atoms are decelerated in the Zeeman slower, they are captured during the loading phase of the MOT. The MOT is composed of three orthogonal pairs of counter-propagating beams of opposing σ^\pm polarization and red detuning δ , and electromagnetic coils that produce a magnetic field gradient. The spatial change in

magnetic field changes the transition energies due to the Zeeman effect, causing the atoms moving away from the center of the MOT to absorb more photons from a counter-propagating beam because of the Doppler effect. This creates a cooling effect and spatial confinement in three-dimensions. A depiction of the MOT action is shown in Fig. 3.13. In the center of the MOT the cooling effect is reduced because atoms are equally likely to absorb σ^+ or σ^- photons. This gives the lowest temperature reached by the MOT as the Doppler temperature [80]

$$T_D = \frac{\hbar\Gamma}{2k_B} \quad (3.3)$$

where Γ is the D_2 decay rate and $\delta = -\Gamma/2$.

In our experimental setup for the MOT, the TA Pro outputs the cooling and repump beams for the MOT along with the slowing beam. The repumping beam is used for the optical transition corresponding to the $F=1/2$ ground state and the cooling beam is for the optical transition corresponding to the $F=3/2$ ground state, as shown in Fig. 3.14. The repumping beam is used to repump the atoms that fall out of resonance with the cooling beams back to the cycling transition. The detuning and power of the MOT beams vary during each phase of MOT operation. The detuning and power are controlled via Labview program and multiplexer circuits. Loading the MOT with atoms is the first phase of the MOT operation which captures atoms coming from the Zeeman slower. This is the phase that has the highest number of atoms in the MOT, and the detuning of the cooling beams is at about 5 linewidths below resonance, with the linewidth of the D_2 transition being 5.87 MHz. In the second phase the atoms are cooled by lowering the detuning to about 2 linewidths away from resonance, which decreases the trap depth of the MOT. Here the physical size of the MOT is decreased and the number of atoms also decreases. The last phase is the pumping phase, where the repumping beam is turned off and only the cooling beams are on to lower the atoms into the ground state to be loaded into the ODT. Table A.2 lists the dynamic MOT properties.

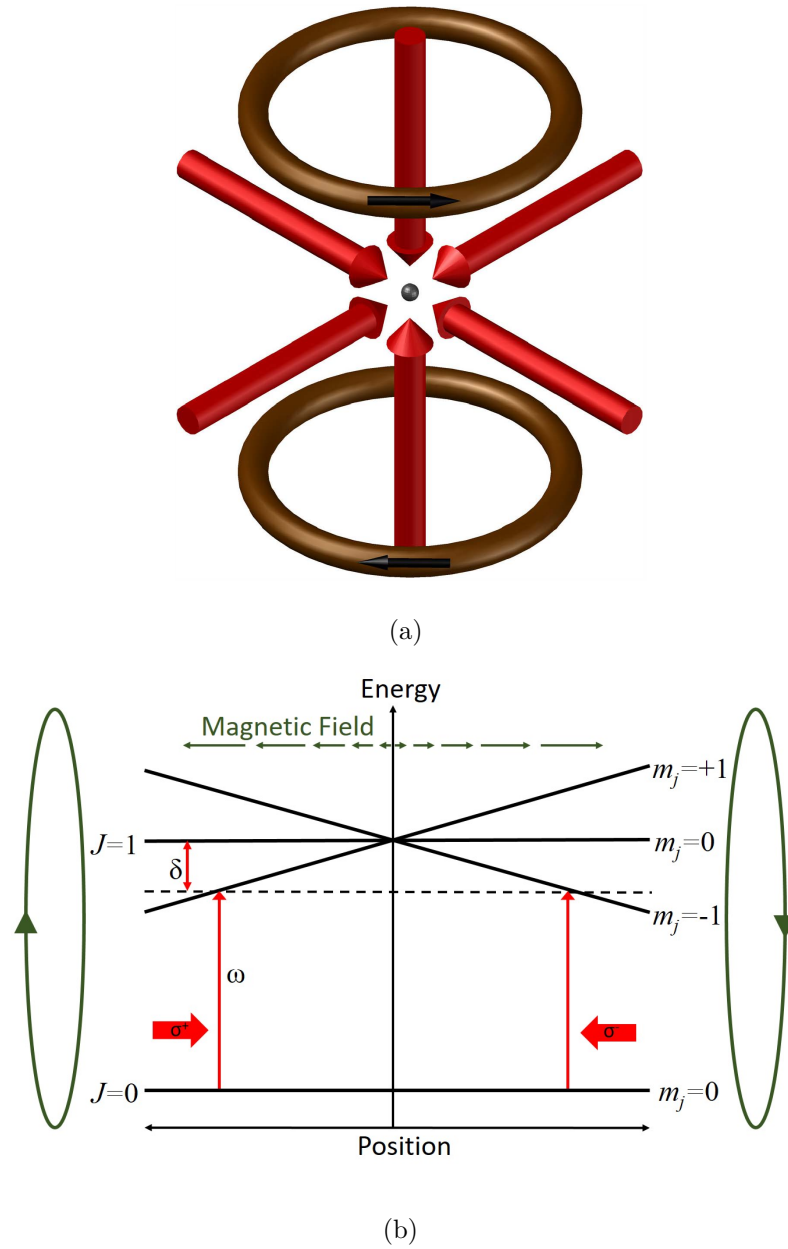


Figure 3.13. MOT operation description. (a) Counter-propagating beams and anti-Helmholtz coils. (b) Circularly polarized beams with frequency ω and detuning from resonance δ create a radiation pressure force on the atoms that is spatially dependent due to the magnetic field gradient.

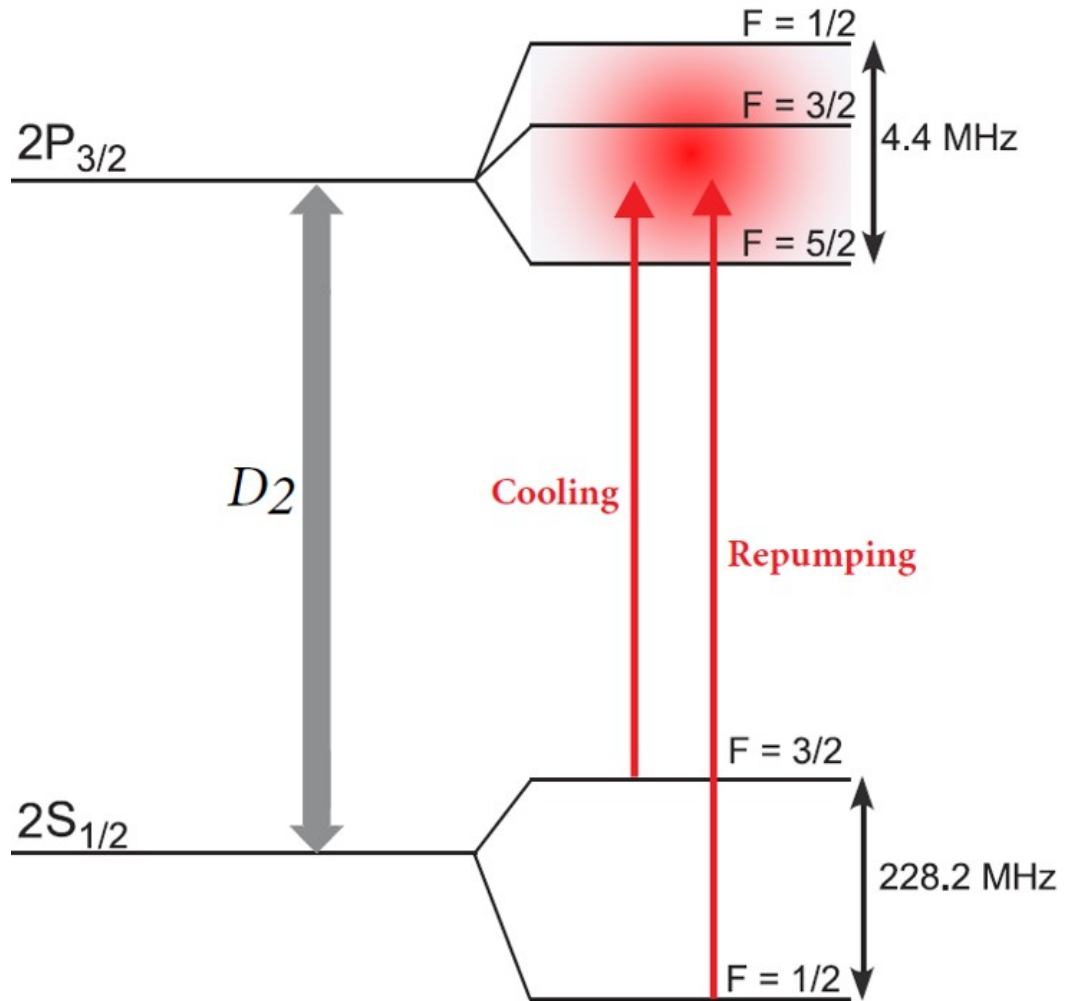


Figure 3.14. MOT transitions. The hyperfine splitting of the $2^2P_{3/2}$ states is smaller than the natural linewidth of the D_2 transition.

Table 3.3.
Dynamic MOT properties

Stage	I/I_{sat}	Detuning (MHz)	Atom number
Loading	2	-28	2×10^9
Cooling	0.1	-8	2×10^8
Pumping	0.08	-5	N/A

3.4 Optical Dipole Trap

In a semi-classical description of atom-light interaction, the electric field of a light wave induces an electric dipole moment $\mathbf{d} = \alpha\mathbf{E}$, where α is the complex polarizability of the atom. An off-resonance light beam of frequency ω and detuning $\Delta = \omega - \omega_0$ from resonance with inhomogeneous spatial light-field creates a conservative potential

$$U_d = -\frac{1}{2} \langle \mathbf{d} \cdot \mathbf{E} \rangle_t = -\frac{1}{2} \langle \alpha \cdot \mathbf{E}^2 \rangle_t = -\frac{1}{2\epsilon_0 c} \text{Re}[\alpha] I \quad (3.4)$$

where I is the intensity of the beam. For $\Delta < 0$, α is positive and the trapping region occurs in the high-intensity region of the beam. Even for large detuning, there is a spontaneous scattering rate Γ_d . The trapping potential and scattering rate for moderate detuning are [81]

$$U_d(r) = -\frac{3\pi c^2}{2\omega_0^2} \left(\frac{\Gamma}{\omega - \omega_0} + \frac{\Gamma}{\omega + \omega_0} \right) I(r) \quad (3.5)$$

$$\Gamma_d(r) = -\frac{3\pi c^2}{2\hbar\omega^3} \left(\frac{\omega}{\omega_0} \right) \left(\frac{\Gamma}{\omega - \omega_0} + \frac{\Gamma}{\omega + \omega_0} \right)^2 I(r) \quad (3.6)$$

where Γ is the decay rate of the D line transition for alkali atoms.

3.4.1 Beam Generation

The beam for the ODT is from an IPG Photonics, YLR-100-LP fiber laser with 100 W at 1064 nm. The main power control in the beams of the ODT is done with a function generator controlling the laser driver. Out of the collimator the beam radius is 1.25 mm, which is reduced to about 0.7 mm to pass through the AOM (Intraaction, ATM-804DA6B) that is used for smaller power control. As shown in Fig. 3.17, the first order output from the AOM then passes a thin-film polarizer (CVI Laser Optics,TFPN-1064-PW-1025-UV) and is picked up by a mirror and sent to the chamber. The zero-order beam is terminated by a water cooling beam dump (Kentek,ABD-2C). All other orders are blocked by homemade air cooling beam dumps. The AOM driver (Intraaction, ME805-EH) allows us to modulate the intensity of the

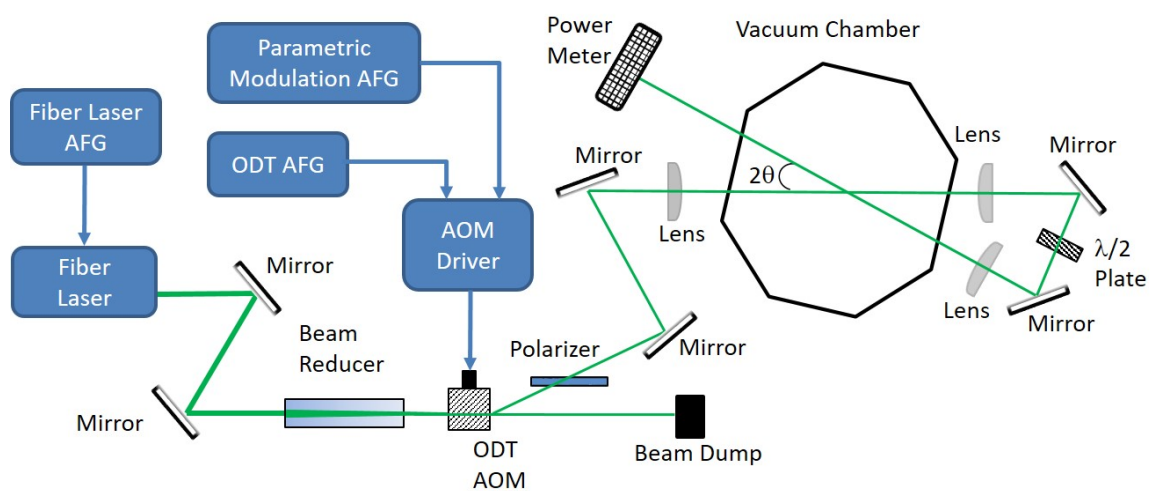


Figure 3.15. ODT control and optical layout.

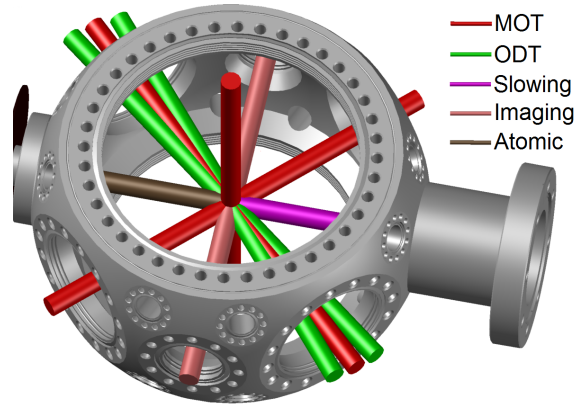


Figure 3.16. Optical and atomic beams in the science chamber. Beam sizes are not to scale.

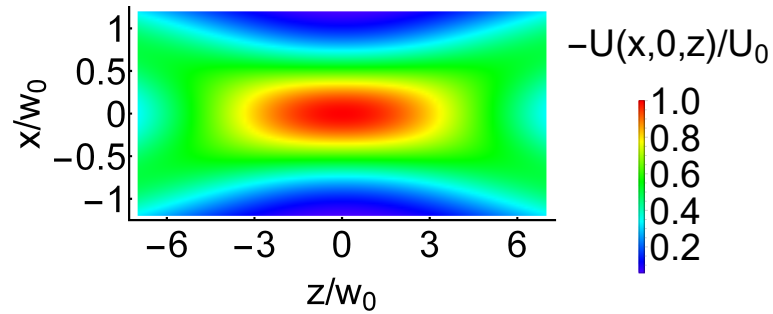


Figure 3.17. Trap potential of the crossed-beam ODT

first-order output with DC voltage values of 0-10 V. The polarization of the crossed beams is linear and made perpendicular to each other by use of a half-wave ($\lambda/2$) plate. The beam diameter at the chamber center is $37 \mu\text{m}$, with the lenses of $f = 300$ mm keeping the beam collimated at the location of the atoms. The crossed beams layout in the science chamber, along with all other beams used in the experiment, is shown in Fig. 3.16.

3.4.2 Optical Dipole Trap Design

For a single beam, the trapping potential is [82]

$$U(r, z) = -\frac{U_0}{1 + (z/z_R)^2} \exp\left(-2\frac{r^2}{w_0^2}\right) \quad (3.7)$$

with

$$U_0 = \frac{\alpha I}{2\epsilon_0 c} \quad (3.8)$$

where I is the beam intensity, ϵ_0 is the permittivity of free space, c is the speed of light, $z_R = \pi w_0^2/\lambda$ is the Rayleigh range of a beam and w_0 is the beam waist. and $\alpha = 4.43 \times 10^{-39} \text{A}^2 \text{s}^4/\text{kg}$ is the polarizability of ${}^6\text{Li}$ for 1064nm wavelength. The lasers create a trapping potentials

$$U_1 = -U_0 \frac{e^{\left(-\frac{2(y^2 + (z\sin(\theta) + x\cos(\theta))^2)}{w_0^2(1 + (z\cos(\theta) - x\sin(\theta))^2/z_R^2)}\right)}}{1 + (z\cos(\theta) - x\sin(\theta))^2/z_R^2} \quad (3.9)$$

$$U_2 = -U_0 \frac{e^{\left(-\frac{2(y^2 + (-z\sin(\theta) + x\cos(\theta))^2)}{w_0^2(1 + (z\cos(\theta) - x\sin(\theta))^2/z_R^2)}\right)}}{1 + (z\cos(\theta) + x\sin(\theta))^2/z_R^2}.$$

In our case $w_0 \ll z_R$, so the total trapping potential reduces to approximately

$$U_T \simeq -2U_0 \left[1 - \left(\frac{\cos^2(\theta)}{z_R^2} + 2\frac{\sin^2(\theta)}{w_0^2} \right) x^2 - \left(\frac{\sin^2(\theta)}{z_R^2} + 2\frac{\cos^2(\theta)}{w_0^2} \right) y^2 - 2\frac{z^2}{w_0^2} \right] \quad (3.10)$$

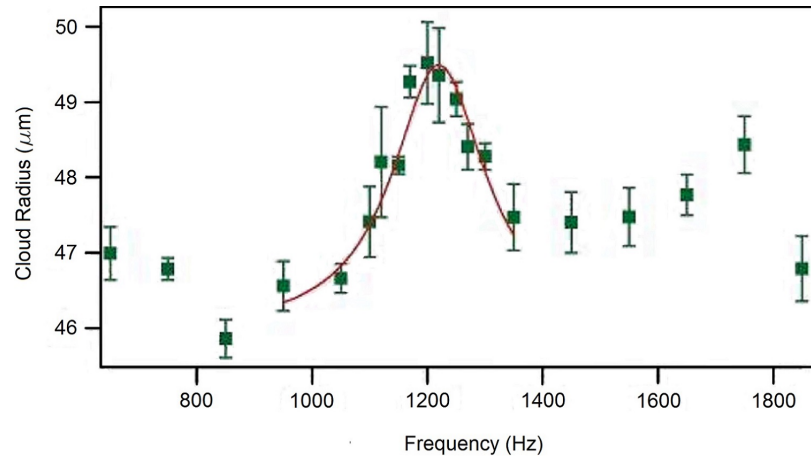
which in the harmonic oscillator approximation gives trapping frequencies

$$\omega_x = \sqrt{\frac{U_0}{m} \left(\frac{8\cos^2\theta}{w_0^2} + \frac{4\sin^2\theta}{z_R^2} \right)}, \omega_z = \sqrt{\frac{U_0}{m} \left(\frac{4\cos^2\theta}{z_R^2} + \frac{8\sin^2\theta}{w_0^2} \right)}, \omega_y = \sqrt{\frac{8U_0}{mw_0^2}} \quad (3.11)$$

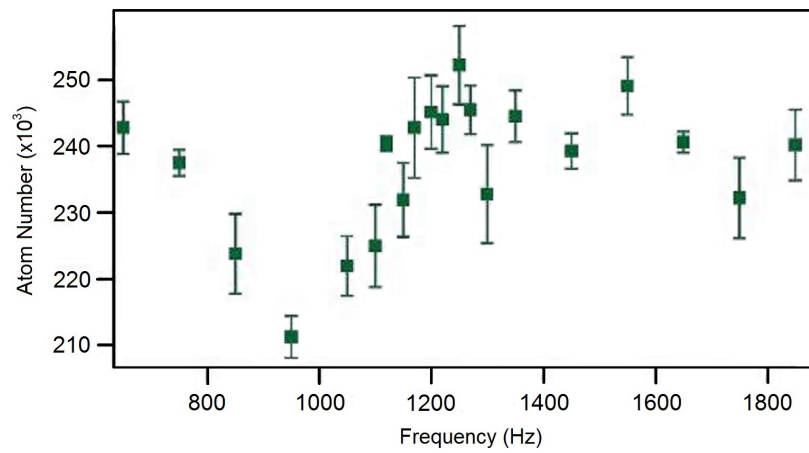
that are used in calculating thermodynamic quantities from the atomic cloud. Fig. 3.17 shows the trap potential generated by the crossed-beam ODT.

3.4.3 Measured Trap Characteristics

Applying the parametric excitation method of shaking the trap, the measured trap frequency in the axial-direction is shown in Fig. 3.18. Shaking for 4 s at trap depth $0.1U_0$ results in measure trap frequencies $\omega_z = 6.37$ KHz and $\omega_x = 6.96$ KHz.



(a)



(b)

Figure 3.18. Trap frequency measurement in z -direction at $0.1U_0$. (a) is the cloud size obtained via a Gaussian distribution fit and (b) is the atom number.

Fig. 3.18 shows that using the atom number in the trap is not quite as accurate as using the atomic cloud size to measure the trap frequency. The Gaussian nature of the trap allows atoms to populate the edges of trap, which have lower trap frequency than at the center. Therefore, a more accurate method is to measure the cloud size, which is dependent on the temperature of the gas.

The measured lifetime of the trap at 527 G is 24.3 s, which gives us enough time to conduct experiments without being concerned with atom loss due to heating.

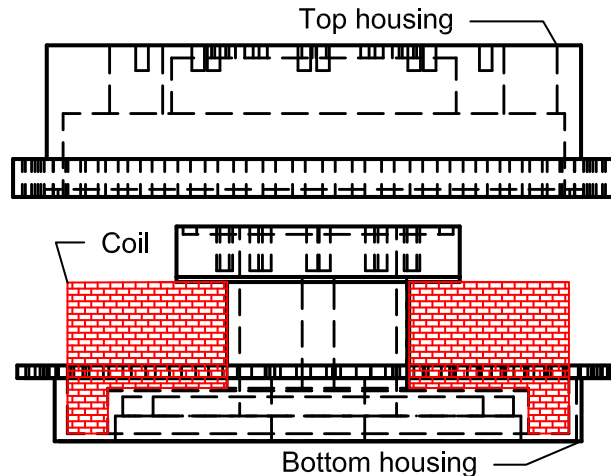


Figure 3.19. Schematic of coil and housing design. Water cooling of coils uses a water flow of about 3 gallons/minute.

3.5 Electromagnets

3.5.1 Design

The MOT requires a magnetic field gradient of about 30/cm with 20 A current for each coil at the location of the atoms. Feshbach resonance magnetic fields must be uniform with strengths of up to 1200 G to reach far enough into the BCS side. Two water-cooled electromagnetic coils—one above, the other below the science chamber, each with its own high-current power supply (Agilent 6684A)—and an H-bridge supply all the magnetic field requirements.

The design of the magnetic coil follows the methods in Ref. [83] with 8 AWG enamel-coated square wire wound on the bottom section of a coil housing made of acetal copolymer. The coil housing is used for water-cooling the magnets since up to 120 A can be used with power dissipation over 1 kW, and starch paper is used to separate each wind and increase that water-cooling performance. The coil winding and housing schematic is shown in Fig. 3.19.

The magnetic field in each coil is controlled by a commanding voltage that can be set on a Labview program and sent through a 16-bit DAC (Measurement Computing

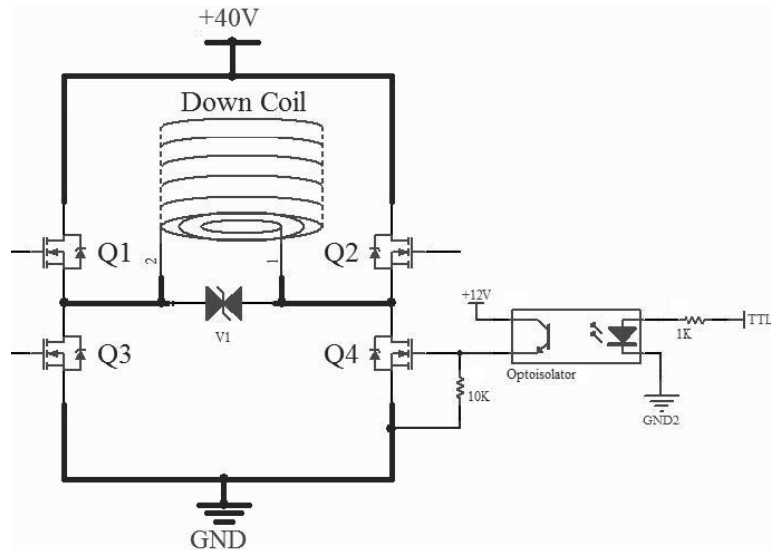


Figure 3.20. H-bridge circuit for the down coil. Each MOSFET has its own optoisolator and power supply. The optoisolators are used to protect the DAQ card from over current.

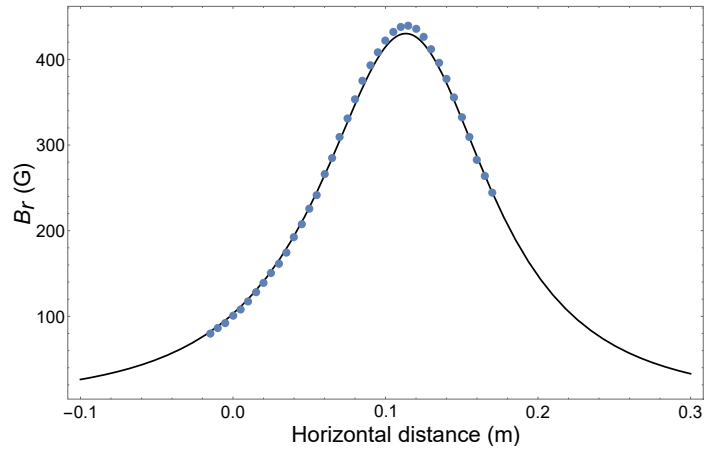
USB-3103), or via TTL signals that control the output voltage of a 2×4 multiplexer. The down coil current direction is controlled by an H-bridge also controlled via Labview.

The H-bridge has four separate banks of ten MOSFETs (IRFP4368PbF) that act as switches to change the direction of the current flowing through the bottom coil. Each MOSFET bank is controlled via a TTL signal that activates a power supply to turn on the MOSFETS via an optocoupler. The switching of current direction leads to voltage spikes due to the inductance of the coils, so transient voltage suppressors (TVS) are installed parallel to the coils to protect the coil power supplies and the MOSFETs. The schematic of the H-bridge design is in Fig. 3.20.

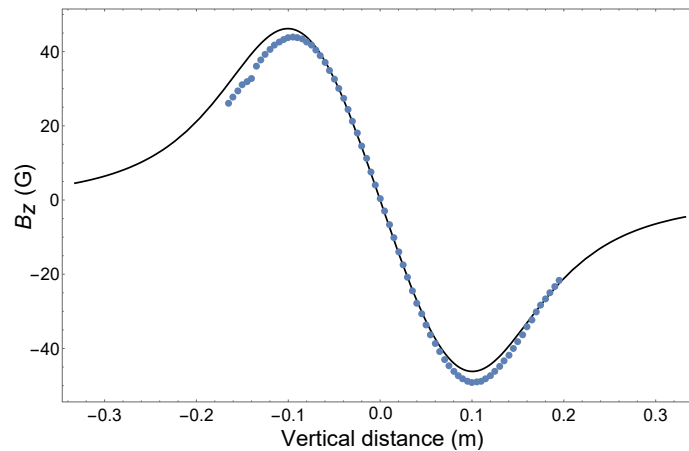
3.5.2 Performance

The magnetic field profile of each coil was measured with a gauss meter (LakeShore 425) at various currents, with one result shown in Fig. 3.21.

Due to the lag time in the TTL signal, the inductance of the coil, the current stability time of the power supply, and the magnetic materials in the stainless steel chamber and tubing around the coils, the switch time from anti-Helmholtz configuration at 20 A to 128 A in Helmholtz configuration is about 350 ms.



(a)



(b)

Figure 3.21. Measurement (blue points) and theoretical prediction (black lines) of one of the coils used for the MOT and Feshbach resonance magnetic fields. (a) Vertical measurement. (b) Horizontal measurement. The vertical magnetic field was measured using 120A current and distance was measured from the center of MOT (6.2 cm). The horizontal field was measured at a 7.6 cm vertical distance from the bottom with a 10 A current

3.6 Radio-Frequency Antenna

In the high field regime used while tuning interactions via Feshbach resonance, transitions between the three lowest states $|1\rangle \leftrightarrow |2\rangle$ and $|2\rangle \leftrightarrow |3\rangle$ can be driven with RF pulses of about 80 MHz. When the RF pulse is used with white noise applied to the center frequency for transitions, population balance can be achieved.

For this purpose, we built an antenna made from a loop of 12 AWG wire soldered onto an sma connector, as shown in Fig. 3.22(a). The impedance matching circuit in Fig. 3.22(b) has a variable capacitor with 2-10 pF and about 50 pF in parallel with the antenna, to match the $50\ \Omega$ output impedance of a 100 W RF amplifier (Minicircuits ZHL-100W-GAN+). The RF signal is generated by a function generator (Rigol DG4162) operated via LabVIEW. The antenna is placed off-center near the bottom reentrant window and supplies Rabi frequency for $|1\rangle$ - $|2\rangle$ transitions of 1 KHz.

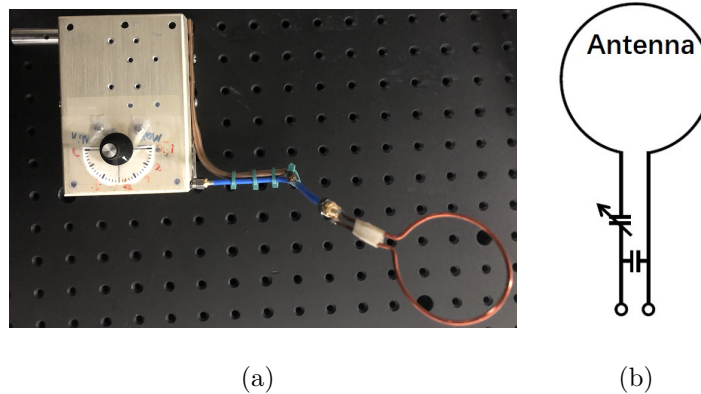


Figure 3.22. RF antenna. (a) Antenna with impedance matching circuit. (b) Circuit diagram for impedance matching circuit.

3.7 Control and Data Acquisition

In order to control experimental instruments operations and gather data in pre-defined, user-modifiable timing sequences, we implemented a computer control system for our apparatus.

3.7.1 Timing System

One computer (“Control”) with an Intel Core Duo 2 3.0GHz CPU controls all I/O except the Hamamatsu ORCA-R2 camera, and the other computer (“Imaging”) with an AMD A8-3850K APU hosts the camera. In a typical experimental run, we use digital I/O card (UEIDAQ PD2-DIO-128) to generate Transistor-Transistor Logic (TTL) patterns in 100 μ s precision. Analog I/O card and multiplexers are used to generate programmable analog signals, and GPIB communication for Standard Commands for Programmable Instruments (SCPI)-compatible instruments. At the same time, the absorption images captured from the camera are automatically acquired and instantly analyzed, all by NI LabVIEW. An example of the control system in use is seen in Sec. 4.3.

The “Control” computer LabVIEW operation panel is shown in Fig. 3.23. This program reads a timing file where the timing sequence for each control signal is written, then outputs the commands to the I/O card to send TTL signals to the corresponding channels used to control the instruments.

The timing sequence for the imaging beam and CCD camera is controlled with a Delay Pulse Generator (Quantum Composer 9000). It controls the AOM operation to turn the imaging beam on/off and triggers the CCD camera to acquire images with sub- μ s precision. This timing output can be seen in the imaging sequence of Fig. 4.5.

3.7.2 Absorption Imaging

We use a Hamamatsu Orca-R2 camera with a cooled CCD array of 1344×1024 pixels to capture the absorption images of the atomic clouds. Each pixel’s photoelectron count can be digitalized in a 16-bit number. The pixels can be binned (treating 2×2 , 4×4 , or 8×8 pixels as one) to increase the sensitivity and frame rate in trade-off with spatial resolution. The camera also has Particle Image Velocimetry (PIV) function installed, which can output two photographs in quick succession.

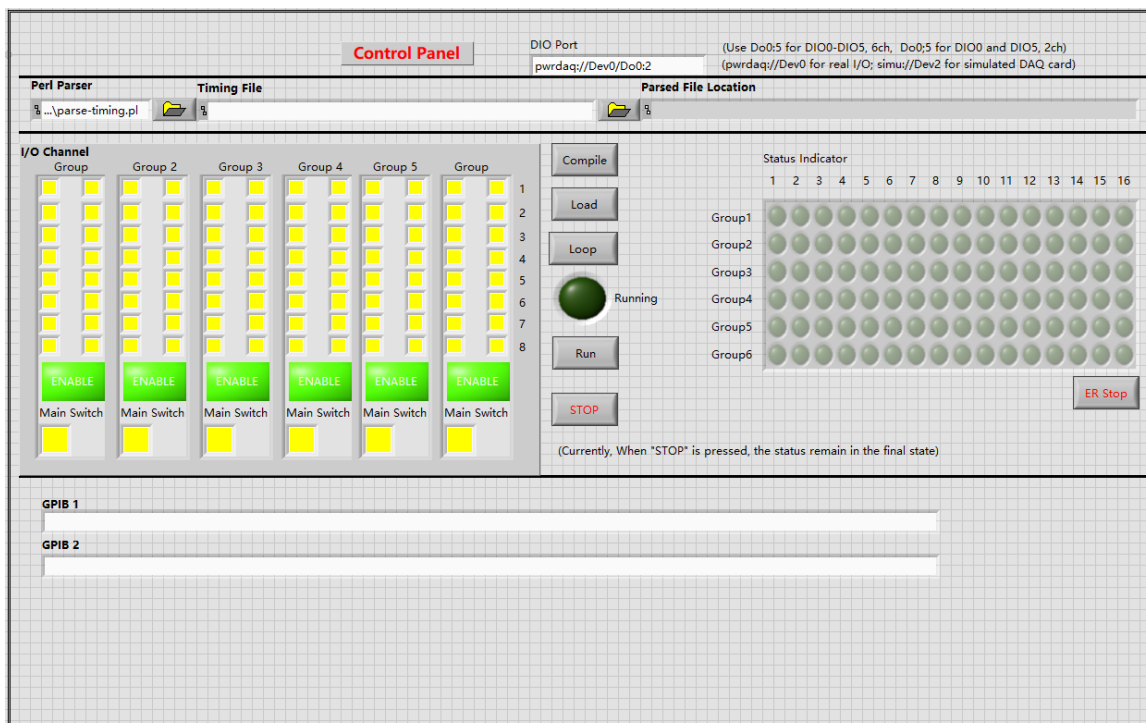


Figure 3.23. Main DAQ timing control for experiments. A timing file read by Labview sets the timing sequences.

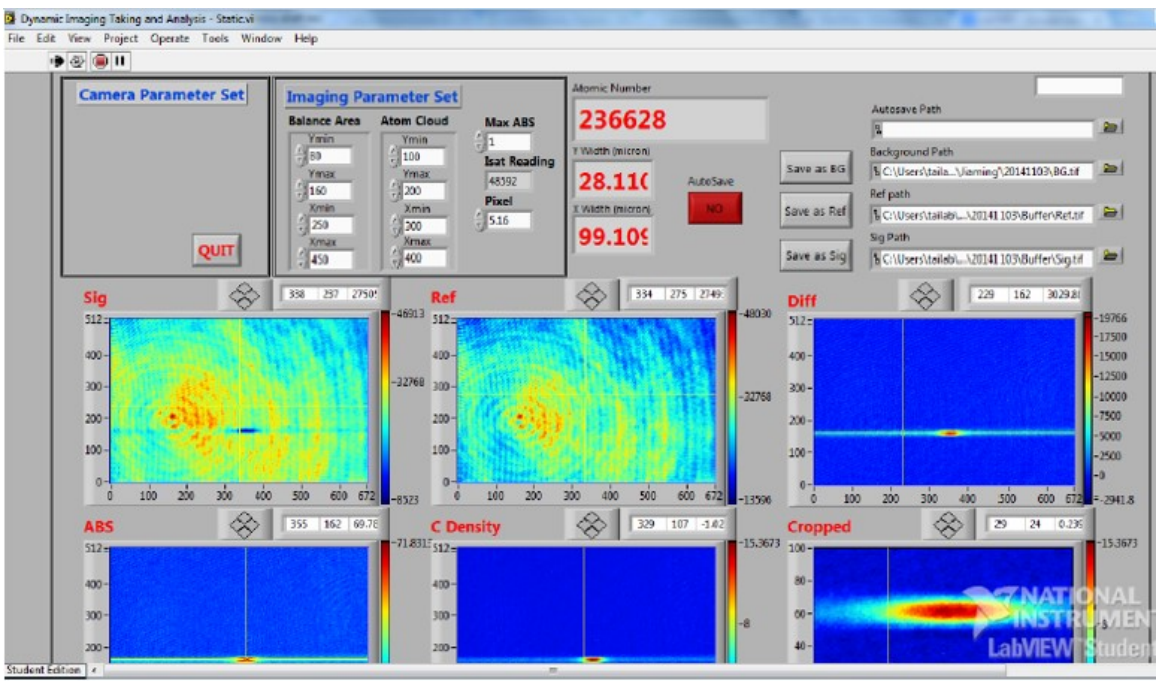


Figure 3.24. Sample image capturing and data analysis with LabView.

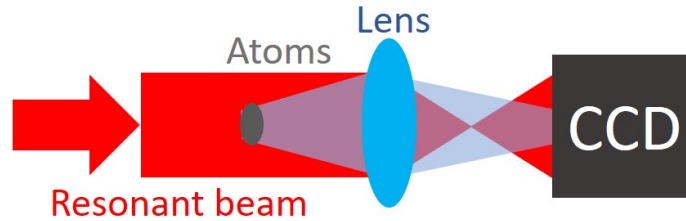


Figure 3.25. Absorption imaging scheme.

Absorption imaging of the atomic clouds is the detection method used to extract physical information from the atoms. Fig. 3.25 shows a schematic of the absorption imaging method. In our setup, the camera has a $6.45 \mu\text{m}$ pixel size and the imaging system magnification is 2.5.

When taking absorption images it is customary to take three pictures in quick succession: The first is the actual absorption image of the atomic cloud with the incident beam, the second one is the reference picture which is taken under conditions identical to the first picture, with the only exception being that there are no atoms present. The third one is a background picture without the absorption beam, which is subtracted from the other pictures. An experimental image of an atomic cloud taken by our apparatus is shown in Fig. 3.26.

The imaging beam comes from the DL Pro laser to probe the atomic clouds and is able to selectively image atoms at the two trapped ground states. This comes from the Zeeman splitting of the hyperfine states $2^2P_{3/2}$ and $2^2S_{1/2} |m_s = -1/2, m_I = 1, 0\rangle$ in high fields where the atoms are imaged. Applying a σ^- beam to the trapped cloud to probe the transition $2^2S_{1/2} |m_s = -1/2, m_I = 1, 0\rangle \leftrightarrow 2^2P_{3/2} |m_J = -3/2, m_I = 1, 0\rangle$, imaging of the states $|1\rangle$ and $|2\rangle$ is possible due to the splitting of about 80 MHz between the states.

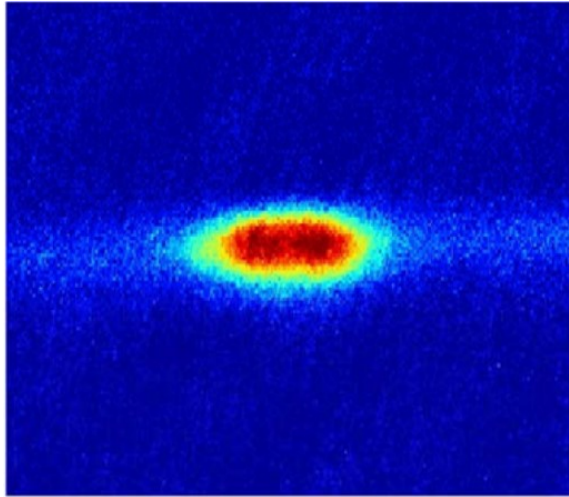


Figure 3.26. Absorption imaging of trapped atomic cloud in the horizontal direction. The cloud size is $42 \mu\text{m} \times 198 \mu\text{m}$ with $2\theta = 14^\circ$.

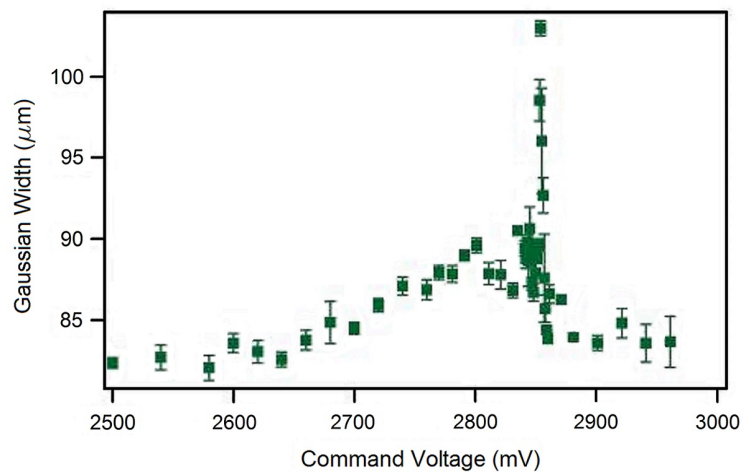


Figure 3.27. Measurement of cloud size for magnetic field calibration.

3.8 Experimental Methods

With the apparatus complete and ready to perform experiments, key techniques must be used for calibration of the system, reaching degeneracy and extracting information from the atomic clouds.

3.8.1 Magnetic Field Calibration

To calibrate the magnetic field produced by the Helmholtz coil configuration of the magnets, a method similar to Ref. [84] is used to find the zero-crossing point of the broad Feshbach resonance of the $|1\rangle$ - $|2\rangle$ the center of the narrow Feshbach resonance at 543.286 G [85]. With this method, the scattering length of collisions between atoms is found by lowering the trap potential for a given command voltage and measuring the cloud size afterward, which is a thermometry method. At the zero-crossing, no cooling effect is present in the gas due to the scattering length $a = 0$ so no elastic collisions occurs to exchange energy between atoms. Fig. 3.27 shows the result of magnetic field calibration.

The test results show that we have two proofs of the calibration magnetic field, one of which can be selected as the benchmark magnetic field, the other one can be used to verify its accuracy. By entering data near 527.32 G, a Gaussian fitting can be used to obtain a voltage at the center point of 2790.2(4) mV, which is combined with our calibration before this. The formula for linear relationship between system voltage and power supply output current, $I = 25.35V - 15.151$ with V in millivolts and I in amperes.

$$B = \frac{V - 598.85}{4.1522} \quad (3.12)$$

The voltage of the narrow-band Feshbach resonance calculated by the formula Eq. 3.12 is in good agreement with previous results, indicating that our magnetic field calibration accuracy is about ± 0.05 G.

3.8.2 Evaporative Cooling

Following the last phase of the dynamic MOT, the ODT is turned on with high laser power to capture as many of the atoms in the MOT as possible. At this point the temperature of the gas is still in the μK range, evaporative cooling is applied by lowering the intensity of the laser beams (therefore lowering the trap potential). The theoretical model used below was first described in Ref. [86], and I will briefly summarize the main points and their use in my experimental work.

The evaporative cooling process is set by the initial trap depth U_0 , which limits the energy the trapped atoms can have. The cooling process is truncated by parameter $\eta = U_0/k_B T$, with atom loss during evaporation scaling as $\dot{N} \propto e^{-\eta}$. The application of evaporative cooling is dependent on setting an appropriate value for η due to the long cooling times required to achieve low temperatures. Also present during cooling is the exponential reduction of cooling efficiency as the atoms thermalize.

Forced evaporative cooling is then used as an effective method to cool the atoms further. By lowering the trap depth exponentially, the truncation parameter remains nearly constant at close to 10 for efficient cooling into degeneracy. Thermalization of the atoms is assisted by increased elastic collision rate between states $|1\rangle$ and $|2\rangle$ given as [87]

$$\gamma = \frac{8\pi^2 N m \bar{\nu}^3 a^2}{k_B T}, \quad (3.13)$$

where a is the scattering length, $\bar{\nu}$ is the mean trap frequency and N is the number of atoms interacting at the end of evaporation.

The evaporative cooling sequence used during experiments is shown in Fig. 4.5 with starting $U_0 \approx 3 \text{ mK}$ and, a constant scattering length of $-280a_0$.

3.8.3 Image Processing

After acquiring the images of the atomic cloud through absorption imaging as described in Sec. 3.7.2, image processing is used to find physical parameters of the cloud.

For a beam traveling in the z -axis, the column density of the atomic cloud is given by [68]

$$n(x, y) = \frac{-1}{\sigma_R} \left\{ \ln \left[\frac{I_s(x, y) + I_r(x, y)}{I_r(x, y)} \right] + \frac{I_s(x, y) - I_r(x, y)}{I_{sat}} \right\} \quad (3.14)$$

where I_s is the intensity of the beam and atomic cloud, I_r is the intensity of the beam, $I_{sat} = 2.54\text{mW}/\text{cm}^2$ is the saturation intensity of the D_2 line, and $\sigma_R = 3\lambda^2/2\pi$ is the scattering cross-section of an atom in the cloud. By integrating eqn. 3.14 over y , the number of atoms can be found as

$$N = \sum_0^{x_0} n(x) \left(\frac{\text{Pixel size}}{M} \right)^2 \quad (3.15)$$

where M is the magnification of the optical system.

To extract the temperature of the atomic cloud, we use time-of-flight absorption imaging to increase the signal-to-noise ratio since a dense cloud will absorb too much of the imaging beam. A non-interacting gas will undergo ballistic expansion when released from the trap, and the density of a degenerate gas is described approximately by a Thomas-Fermi distribution [88]

$$n(x, y) = \frac{N}{\pi b_x b_y} \frac{\text{Li}_2 \left\{ -\text{Exp} \left[\frac{U_0 - \mu}{k_B T} - \left(\frac{x^2}{b_x^2} + \frac{y^2}{b_y^2} \right) \right] \right\}}{\text{Li}_3 \left\{ -\text{Exp} \left[\frac{U_0 - \mu}{k_B T} \right] \right\}} \quad (3.16)$$

where $b_i = a_i \sqrt{k_B T / U_0}$ is the cloud width coefficient in the i -direction with a_i as the $1/e$ width of the trap potential, and μ is global chemical potential of the trap which is defined as the chemical potential at the center of the trap. For the ground state,

$$\mu = E_F = \hbar \bar{\omega} (3N)^{1/3} \quad (3.17)$$

where E_F is the Fermi energy and $\bar{\omega}$ is the geometric mean trap frequency. With the atom number N found using eqn. 3.15, a curve fitting routine based on eqn. 3.16 will need only b_x and T/T_F as free fitting parameters.

The signal-to-noise ratio limits the atomic expansion of the column density; the solution to this problem is to turn off the trap and let the atomic cloud expand ballistically. When an atom is released from a trap, it ignores the velocity impact of other collisions and all atoms are ejected isotropically at the initial velocity, following a trajectory

$$x(\tau) = x_0 + \frac{p_x}{m}\tau \quad (3.18)$$

where τ is atomic ballistic flight time time-of-Flight, p_x is the momentum of an atom which remains constant during expansion. In the ballistic expansion, the Fermi radius expands as [82]

$$\sigma_x(\tau) = \sigma_{0x}\sqrt{1 + \omega_x^2\tau^2}. \quad (3.19)$$

Igor Pro is used for image processing, where the three images taken first read by a function to calculate the absorption of the imaging beam by the atomic cloud, then outputs the atom number. Then the one-dimensional column density is determined for the x and y axes via fitting to a zero-temperature Thomas-Fermi or Gaussian shape. Finally the cloud width and temperature are also obtained via fitting functions.

4. PARAMETRIC COOLING

4.1 Introduction

Parametric excitations in cold atoms research was first applied to trapped ^{87}Rb atoms in an optical lattice to probe their vibrational frequencies [89]. The intensity of the trapping beams was modulated at frequencies in the range of the harmonically approximated radial ω_r and axial ω_z frequencies of the lattice. At the parametrically resonant frequencies in the axial or radial directions, it was observed that the largest number of atoms left the trap. This is attributed to the atoms gaining kinetic energy due to the exponential rise in harmonic motion amplitude during the beam intensity modulation. This procedure is now standard in cold atoms experiments to determine the central trap frequencies in optical, and magnetic traps, and has also been shown in a MOT [89]. More techniques with parametric cooling have been developed prior to this work, and this chapter describes some of their methods and results. Also included is a brief description of other cooling methods developed for optically trapped neutral atoms.

4.1.1 Cooling Techniques for Ultracold Atoms

Evaporative cooling by trap weakening as described in Sec. 3.8.2 remains the most widely used and well known method for cooling an optically trapped gas down to degeneracy. For optical traps, the loading and evaporation phases have opposite dependence on the trapping beam power, with beam power decrease necessary for reaching degeneracy, though it lowers the collision rate and limits phase-space density. To overcome these problems, other cooling techniques have been developed, whereby not lowering the trap frequency during evaporation increases the phase space density

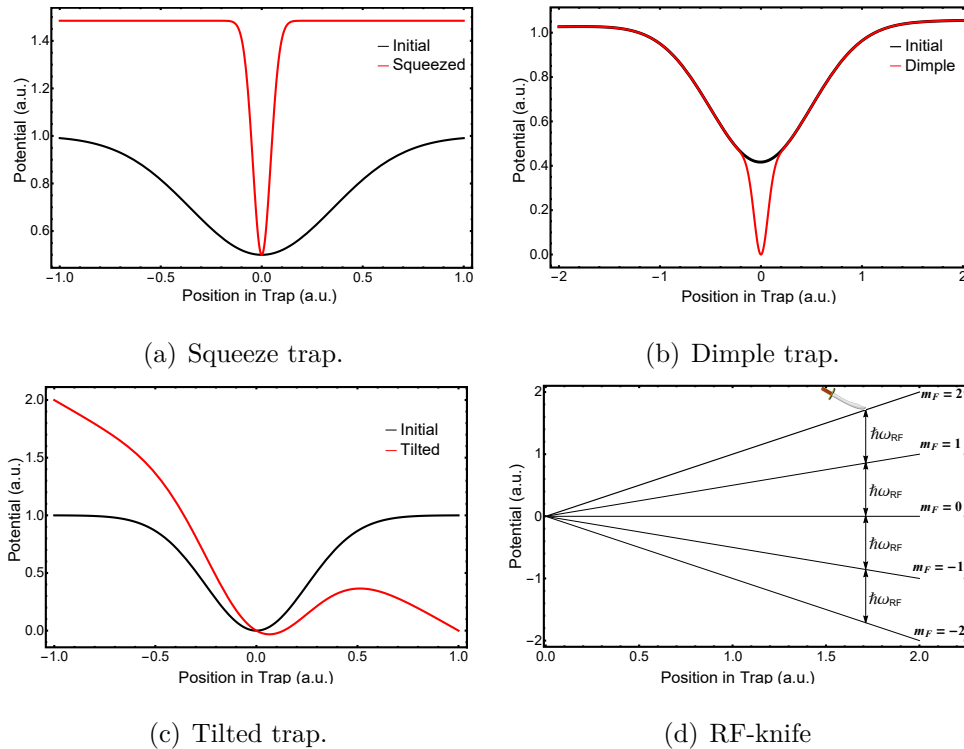


Figure 4.1. Cooling methods used in magnetic and/or optical traps. Black plots are the initial trap potential and red plots final. (a) By moving one of the cross-dipole trap beams, the waist at the location of the cloud is increased, which increases the trap frequency and reduces the trap volume. (b) A beam of much smaller power and waist is added to the trapping beams to create a “dimple” in the potential. (c) The addition of a bias magnetic field gradient tilts the trap potential to “spill” atoms from trap. (d) Unlike the other methods, the RF-knife removes atoms based on their position in the magnetic trap without lowering the confinement depth.

according to the scaling laws [86]. These “expelling” techniques use a variety of optical and magnetic trapping schemes, some of which are quite complex experimentally. The goal of these techniques is to decouple the trap depth from the trap frequency to keep the confinement nearly constant during evaporation. Below is a review of cooling methods using trap modification for evaporation cooling without trap depth lowering, with the trap potentials plotted in Fig. 4.1.

In the trap compressing (squeeze) method [90,91] atoms are loaded into a crossed-beam trap of equal beam waists and power, then one of the beam waists at the location of the atom cloud is decreased by moving the beam center away from the cloud location. The trapping potentials for the squeeze trap are shown in Fig. 4.1(a). This technique increases the spatial density of the trap by making the trap volume decrease more than the number of atoms lost and increases the trapping frequency, which for an optical trap goes as \sqrt{P}/w_0 . The increase in trap frequency leads to the increase of phase-space density, but because of increased heating due to the compression, degeneracy cannot be reached without simultaneous trap weakening. In order for degeneracy to be achieved, the power of the trapping beams must also be lowered. The optical setup here is technically challenging because of the precise alignment of optics required for beam focusing while the moving beam is adjusted with an opto-mechanical stage.

The “dimple” trap technique decouples the trap depth and frequency by applying a second beam at much lower beam power and waist to a crossed beam trap [92,93]. The dimple is at higher trap frequency than the trapping potential, so the phase-space density and collision rates in the dimple are dramatically increased, but this is not enough for degeneracy on its own, and must be combined with trap-depth lowering to achieve degeneracy. In the case of Ref. [93], beams in all three axes are required, making the dimple trap configuration technically more complex than the standard optical trap design with two beams.

For the trap tilting scheme [94], an applied magnetic field gradient creates an asymmetric potential allowing atoms to “spill” out from one side of trap, as shown in Fig. 4.1(c). Here the tilted trap frequency dependence on trap depth is much smaller than in the trap weakening scheme. This is the only optical trapping method that does not require trap-depth lowering by optical means to achieve degeneracy. Experimentally this requires the use of multiple electromagnets to create the bias field and the magnetic field gradient. The use of magnetic fields for trap tilting also

affects the scattering length and can lead to unwanted interactions in a degenerate gas through Feshbach resonance.

The first cold atom BECs and DFGs were created in magnetic traps using electromagnets [7, 8, 10]. Various electromagnet configurations have now been used [72], but all use the interaction between the dipole moment $\boldsymbol{\mu}$ of the atom and the applied magnetic field B to have trapping potential $U_{mag}(\vec{r}) = -\boldsymbol{\mu} \cdot \mathbf{B}(\mathbf{r})$. For the magnetic quadrupole trap [95], the trapping potential is linear in space, with the slope dependent on the $|F, m_F\rangle$ level. For the $5^2S_{1/2}$ ground states of ^{87}Rb [96], only the $m_F = 1, 2$ states of $F = 2$ are low-field seeking hyperfine states to be trapped, as seen in Fig. 4.1(d). The RF evaporation method uses the hyperfine splitting due to the Zeeman effect to spin-flip atoms according to their position in the trap [97], down to anti-trapped m_F states. This evaporation technique was successful in producing the first degenerate Fermi gas, but as more optical traps are used in experiments, a position-dependent cooling technique is yet to be developed. This is the motivation for the parametric cooling technique described in Sec. 4.1.3.

4.1.2 Parametric Excitation

For a harmonic oscillator, applying an external driving force at a frequency different from the natural frequency will cause the amplitude of the oscillations to respond depending on the driving frequency. This parametric excitation can be seen when a person on a swing is pushed by person on the ground, as in Fig. 4.2(a). If the person pushes at twice the swing frequency, the amplitude of the swinging motion increases, but this is not the only driving frequency that will increase the amplitude of the swing. Likewise, pushing at other odd frequencies will cause the amplitude to vary, sometimes increasing and other times decreasing.

The model [98] for this driven motion in one-dimension uses the equation of motion

$$\ddot{x} + \omega^2(t)x = 0 \tag{4.1}$$

with $\omega^2(t) = \omega_0^2(1 + \delta\cos(\gamma t))$ where δ is positive and $\delta \ll 1$. By letting γ vary by some small amount ϵ , the parametric resonance regions for the driving frequency are found to be

$$-\frac{1}{2}\gamma\omega_0 < \epsilon < \frac{1}{2}\gamma\omega_0 \quad (4.2)$$

with $\gamma = 2\omega_0$. This stability region is shown in Fig. 4.2(b).

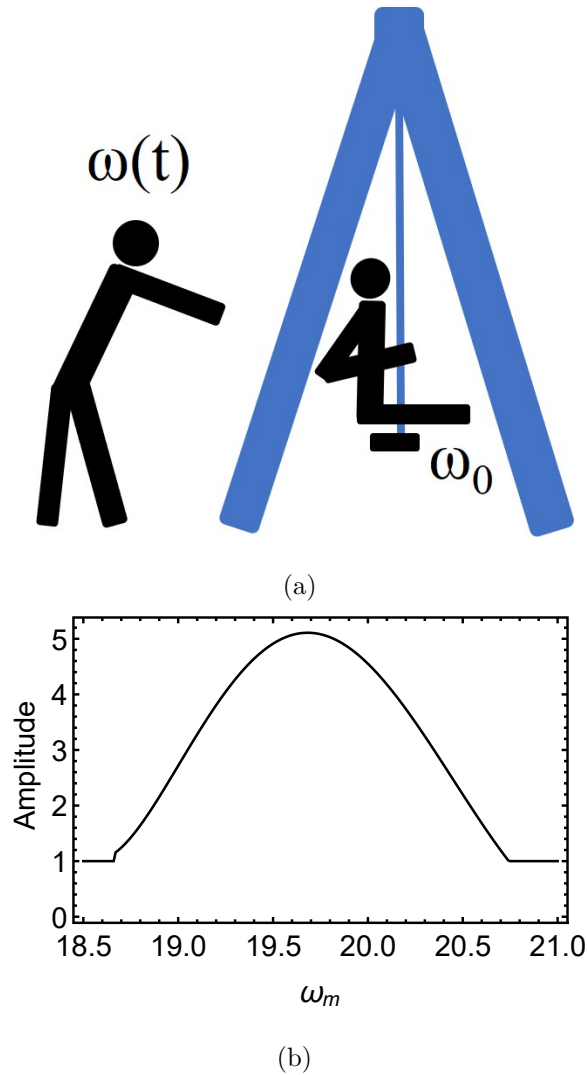


Figure 4.2. Parametric driving characteristics for a harmonic oscillator. (a) A child swinging at frequency ω_0 , being pushed at frequency $\omega(t)$. (b) Simulation of Eq. 4.1 with $\delta = 0.15$, $\omega_0 = 2\pi \times 10$ Hz, and $t_m = 2\pi/\omega_m$.

The use of parametric excitation in cold atoms research leads to useful results in completely opposite directions. In magnetic or optical traps, many of the trapped atomic properties like atom number and temperature are dependent on the trap frequency ω_0 or the mean trap frequency $\bar{\omega} = \sqrt[3]{\omega_x\omega_y\omega_z}$. The technique used to determine the trap frequencies is to scan the modulation frequency of the trap depth and observe the atom loss from the cloud. When the modulation frequency is at $2\omega_0$, parametric resonance occurs, so the atoms at the bottom of the trap gain enough kinetic energy to leave the trap and the observed atom number left in the cloud reaches its minimum, while also heating the trap. This technique takes advantage of the harmonic approximation of the trapping potential to excite atoms occupying the lowest energy region of the trap. In the following section the application of parametric excitation to cool the atomic cloud is discussed.

4.1.3 Parametric Cooling in Cold Atoms

In all of the parametric excitation work done in cold atoms, the center region of the trapping potentials is Taylor expanded to find the harmonic approximated trapping frequencies. When the trapping potential is treated as harmonic, parametric excitation of the trapping potential amplitude in one dimension is described by the Hamiltonian

$$H = \frac{p^2}{2m} + \frac{1}{2}m\omega_x^2x^2(1 + f(t)) \quad (4.3)$$

where ω_x is the harmonic frequency and $f(t) = \delta\sin(\omega t)$ is the modulating function with amplitude δ and modulation frequency ω . Alternatively, modulation of the trapping potential center position has been used for parametric excitation of cold atoms and this is described by

$$H = \frac{p^2}{2m} + \frac{1}{2}m\omega_x^2(x + f(t))^2. \quad (4.4)$$

For cooling trapped atomic gases, both spatial and amplitude modulation have been applied, as shown in Table 4.1. Below is a review of the experiments and results:

In the spatial modulation work [24], the position of the center of the magnetic trap was modulated for 5 seconds in the x -direction with an amplitude of 0.5mm, and cooling was observed for multiple modulation frequencies $\omega \neq 2\omega_{r,z}/n$, with n an integer as predicted by the classical parametric excitation model [98]. Here the trapping frequencies were $\omega_r = 2\pi \times 210$ Hz and $\omega_z = 2\pi \times 16$ Hz. At modulation frequency $\omega = 2\pi \times 53$ Hz it was observed that the atoms located within the shaking amplitude length of 2×0.5 mm remain in the trap since they are not on resonance with the parametric excitation, showing that the anharmonicity of the trap potential, which in this experiment was $U(x) \propto x$ for the region away from the trap center, is crucial for the application of parametric cooling. At highest cooling efficiency, the cloud temperature was decreased from 0.36 mK to 0.16 mK.

The amplitude modulation of a magnetic trap work used a quadrupole-Ioffe electromagnet configuration [26] that was used for trapping a thermal gas with $\omega_x = \omega_y = 2\pi \times 230$ Hz and $\omega_z = 2\pi \times 20$ Hz trap frequencies. Parametric cooling was optimized at modulation frequency $\omega = 2\pi \times 34$ Hz, which is between the two expected classical resonances of $2\pi \times 20$ Hz and $2\pi \times 40$ Hz. The results of this experiment were not as conclusive as others, with possible explanation dependent on collision rate between atoms causing heating at rate of the same order of magnitude as the parametric cooling.

In the amplitude modulation of an optical lattice trap work [25], the potential in the axial direction is well approximated by $\cos(k_L z)$, where $k_L = 2\pi/\lambda$ and $\lambda = 787$ nm is the trapping beam wavelength. The center frequencies were $\omega_r = 2\pi \times 1.3$ kHz and $\omega_z = 2\pi \times 700$ kHz. Multiple frequencies were identified for cooling for modulation frequencies at values close to $2\omega_z/n$ with n odd.

4.2 Optical Trap Anharmonicity

In our cooling method, we take advantage of the anharmonicity of the cross-beam dipole trap described in Sec. 3.4. The deviation of the Gaussian trap created by

Table 4.1.
Parametric cooling in cold atoms.

Trap	Trap Modulation	Species
optical	amplitude	^{40}K , fermion
magnetic	spatial	^{87}Rb , boson
magnetic	amplitude	^{87}Rb , boson

crossed-beam configuration from the harmonic approximation in Eq. 3.10 is shown in Fig. 4.3. Classically, the motion of a particle moving in a potential well $U(x)$ is described by the Lagrangian [98]

$$L = \frac{1}{2}m\dot{x}^2 - U(x) \quad (4.5)$$

with the total energy being $E = \frac{1}{2}m\dot{x}^2 - U(x)$. By integrating the energy over time, the frequency of oscillation in a symmetric potential well is

$$\omega = \frac{\pi\sqrt{2/m}}{\int_{-x}^x [E - U(\tilde{x})]^{-1/2} d\tilde{x}}. \quad (4.6)$$

Applying the above method to the three-dimensional potential well created by the crossed-beam dipole trap potential from Eq. 3.11 and considering the motion up to turning points at positions in the direction of integration $\pm x$ (at these points $\dot{x} = 0$ so $E = 0$),

$$\omega_x(x, y, z) = \frac{\pi\sqrt{2/m}}{\int_{-x}^x [U(x, y, z) - U(\tilde{x}, y, z)]^{-1/2} d\tilde{x}}. \quad (4.7)$$

The dispersion of frequency $\omega_x(x, 0, z)$ in the $y = 0$ plane is shown in Fig. 4.4, where $\omega_{x0,y0,z0}$ are the frequencies at the center of the trap in the harmonic approximation. The atom densities $n(x), n(z)$ in the region of the trap occupied by atoms show a larger dispersion of ω_x in the z -direction. Therefore, parametric excitation along the z -axis can be used to selectively eject high-energy atoms from the trap. The large frequency drop along the z -axis allows applying parametric excitation to selectively remove high-energy atoms in a degenerate Fermi gas.

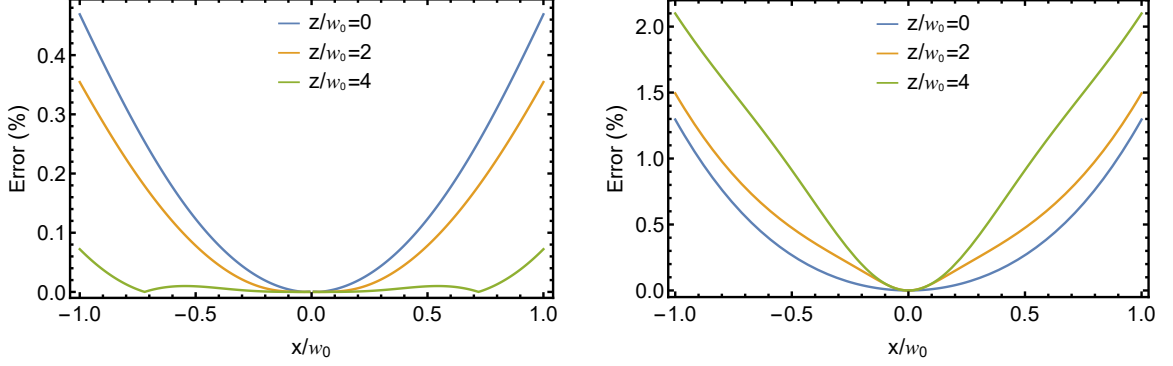


Figure 4.3. Deviation of the harmonic approximation from the actual trap in the x -direction as a function of position in the z -axis. (a) Harmonic approximation using the $\omega_x(z)$ calculated from Eq.4.7. (b) Harmonic approximation using the ω_x calculated from the trap depth as in Eq. 3.11.

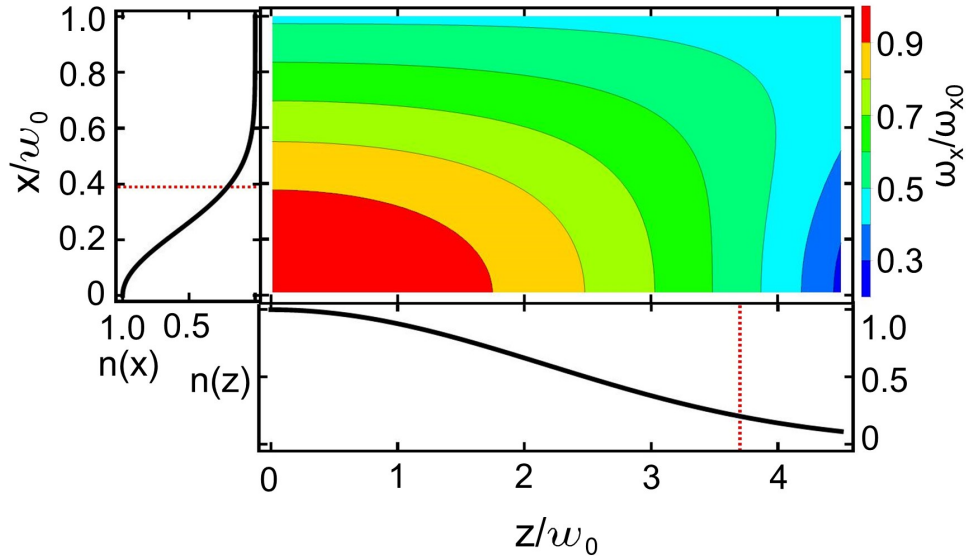


Figure 4.4. The x -axis trap frequency $\omega_x(x, 0, z)$ is plotted in the x - z plane in term of the harmonic frequency $\omega_{x0} = 2\pi \times 760$ Hz (the calculated value from the trapping potential). The radial and axial atom densities $n(x)$ and $n(z)$ are plotted in the left and bottom frames for a Fermi gas of 1.6×10^5 atoms per spin state at $T/T_F = 0.6$ using a 1D Thomas-Fermi distribution. The red dashed lines show the positions of the Fermi radii in the radial (σ_x) and axial (σ_z) directions, where the local trapping frequency drops to $\omega_x(\sigma_x, 0, 0) = 0.89\omega_{x0}$ and $\omega_x(0, 0, \sigma_z) = 0.55\omega_{x0}$.

4.3 Experimental Procedure

To prepare the Fermi gas for parametric cooling, ${}^6\text{Li}$ atoms in the two lowest hyperfine states of $|F = 1/2, m_F = \pm 1/2\rangle$ (as $|1\rangle$ and $|2\rangle$ states) are prepared in the final stage of the MOT, as described in Sec. 3.3.4. The pre-cooled atoms are then transferred into the crossed-beam ODT, where the beam power is set to 100 W, and at the same time the H-bridge is activated to switch the electromagnets to Helmholtz configuration. The bias magnetic field is quickly swept to 330 G to implement evaporative cooling in the weakly interacting regime. In the first part of evaporative cooling, the fiber laser beam power is linearly reduced to 10 W to generate a trapping potential of $0.1U_0$ in 0.5 s by electronic control of the laser head. Then the trap potential is further lowered exponentially to $0.01U_0$ via the AOM, which is controlled by an arbitrary function generator in 30 ms, giving a final trap depth of $5.6 \mu\text{K}$ (U/k_B) for the crossed-beam trap. A noisy radio-frequency pulse is then applied via an antenna placed below the vacuum chamber to prepare a 50:50 spin mixture. To prepare a noninteracting Fermi gas, the magnetic field is swept to 527.3 G, where the s-wave scattering length of $|1\rangle$ and $|2\rangle$ states is zero [16]. Typically we have a noninteracting Fermi gas of $N = 1.6 \times 10^5$ atoms per spin state at $T/T_F \simeq 0.6$ with $T_F \simeq 1.6 \mu\text{K}$ to start parametric modulation. The experimental sequence is illustrated in Fig. 4.5.

The trap potential oscillation is produced by sinusoidal modulation of the intensity of the ODT beam, which is done using an arbitrary function generator to control the signal commanding an AOM. The trap potential then goes as $U(t) = U_0(1 + \delta\cos(\omega_m)t)$, with $U_0 = 2.8 \mu\text{K}$ for 100 mW single trapping laser power. To verify the cooling effect, the atomic cloud is probed by absorption imaging. In this procedure, the arbitrary pulse generator is programmed to turn off the IPG beam and let the cloud ballistically expand for $300 \mu\text{s}$. The pulse generator then commands the CCD camera and probe beam AOM to acquire the signal and background shots for absorption imaging.

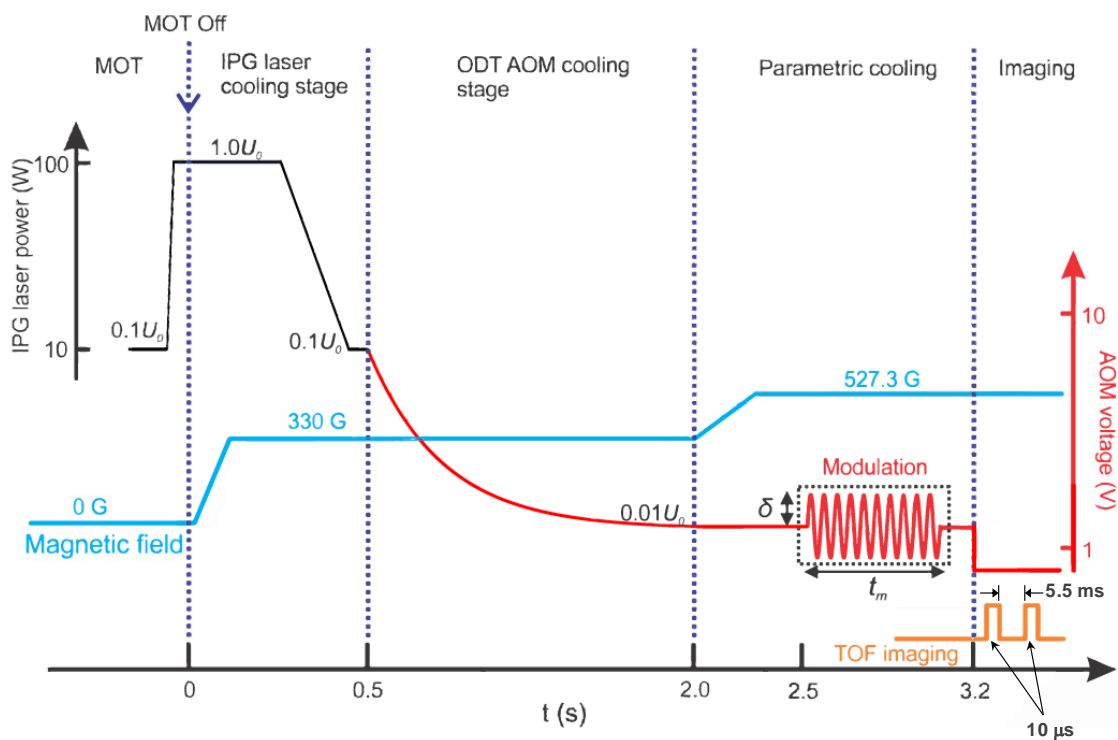


Figure 4.5. Experimental timing sequence. The sequence starts at the MOT loading stage where the ODT beam is first turned on, and ends after the two shots are taken for absorption imaging.

4.4 Results

The cloud properties, such as the atom number, energy, and temperature, are determined by the column density as described in Sec. 3.8.2. The total energy per particle is given by $E = E_x + E_y + E_z$ based on uncoupled atomic motions in different directions. For a noninteracting gas, the virial theorem gives $E_{x,y,z} = 2U_{x,y,z}$ by using a harmonic approximation for the trapping potential. U_x is the potential energy per particle along the x -axis, which can be determined by $U_x = N^{1/3}m\omega_x^2 \langle x \rangle^2 / 2$. The number-independent mean square size (NIMS) $\langle x^2 \rangle = N^{-1/3} \int x^2 n(x) dx$ can be obtained directly from the one-dimensional density profile of the atom cloud [99]. Finally the energy in the x -direction is given by $E_x/E_F = m\omega_x^2 \langle x^2 \rangle / 6^{1/3} \hbar \bar{\omega}$.

4.4.1 Modulation Amplitude

The dependence of the parametric excitation on the modulation amplitude with fixed modulation frequency $\omega_m = 1.5\omega_{x0}$ is shown in Fig. 4.6. For the modulation frequency $\omega_m = 2\omega_{x0} = 2\pi \cdot 1500$ Hz, E_x/E_F increases dramatically when the modulation amplitude increases, which is consistent with the parametric heating effect along the radial direction. For the modulation $\omega_m = 1.5\omega_{x0}$, E_z/E_F decreases significantly with an increase of the modulation amplitude, showing that a stronger cooling effect takes place when larger modulation expels more high-energy atoms out of the trap. The cooling effect saturates when δ increases to 0.25 due to the fact that the modulation becomes so strong that most atoms in the anharmonic region have already been expelled from the trap. We simulate the dependence on the modulation amplitude shown by the solid lines in Figs. 4.6(b) and 4.6(c). The simulations exhibit both heating and cooling features, which agree with the experimental results reasonably well.

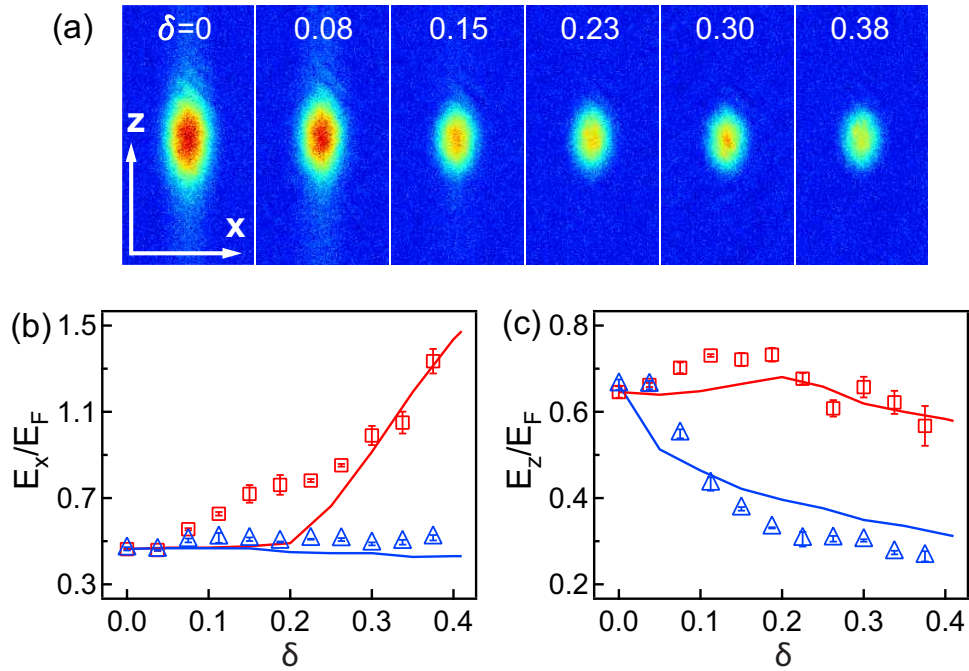


Figure 4.6. The dependence of the radial and axial energies on the modulation amplitudes. (a) The absorption images of the atom clouds show a dramatic decrease of the axial cloud sizes with an increase of modulation amplitudes, where $\omega_m = 1.5\omega_{x0}$. (b) The dependence of the radial energies on the modulation amplitude. (c) The dependence of the radial energies on the modulation amplitude. In both (b) and (c), blue triangles are at the modulation frequency $1.5\omega_{x0}$, and red squares are at $2.0\omega_{x0}$. The solid lines represent the simulation of the anharmonic oscillator model using the same simulation parameters for the frequency dependence.

4.4.2 Modulation Frequency

With modulation amplitude $\delta = 0.15$ and modulation time $t_m = 500$ ms, Fig. 4.7 shows the results of the parametric excitations of the atomic cloud and the theoretical results from our model. The simulation results of the atom number, E_x , and E_z are shown by the solid lines in Fig. 4.7, where we only adjust the harmonic frequency ω_{x0} to $2\pi \times 825$ Hz in our simulation for the best fit of the experimental data, while keeping all other simulation parameters as the experimental values.

4.4.3 Modulation Time

The results of the time-dependence experiment are shown in Fig. 4.8. After about 500 ms modulation, the E_z/E_F is reduced significantly from 1.80 to 0.90 and the E_x/E_F is slightly increased from 1.20 to 1.25. The decreasing atomic numbers in Fig. 4.8(b) inset indicate atoms are expelled out of the trap. We find that parametric cooling changes the atomic cloud energy in an anisotropic way, in which the energy in the axial direction is below the Fermi energy while the radial one is still above the Fermi energy. It is noted that the initial unequal energies in axial and radial direction are generated by the fast trap lowering during evaporative cooling. After the parametric cooling, the axial direction energy is significantly reduced while the radial energy is barely changed. This result indicates the way that parametric cooling changes the cloud energy is anisotropic. This anisotropic effect is due to the fact that the dominant anharmonicity of the crossed-beam ODT is along the axial direction.

4.5 Simulation of Parametric Cooling

For atoms in the x - z plane of the trap, the equation of motion with parametric excitation of the trap amplitude is

$$\frac{d^2x}{dt^2} + \frac{1 + \delta \cos(\omega_m t + \phi)}{m} \frac{dU(x, z)}{dx} = 0. \quad (4.8)$$

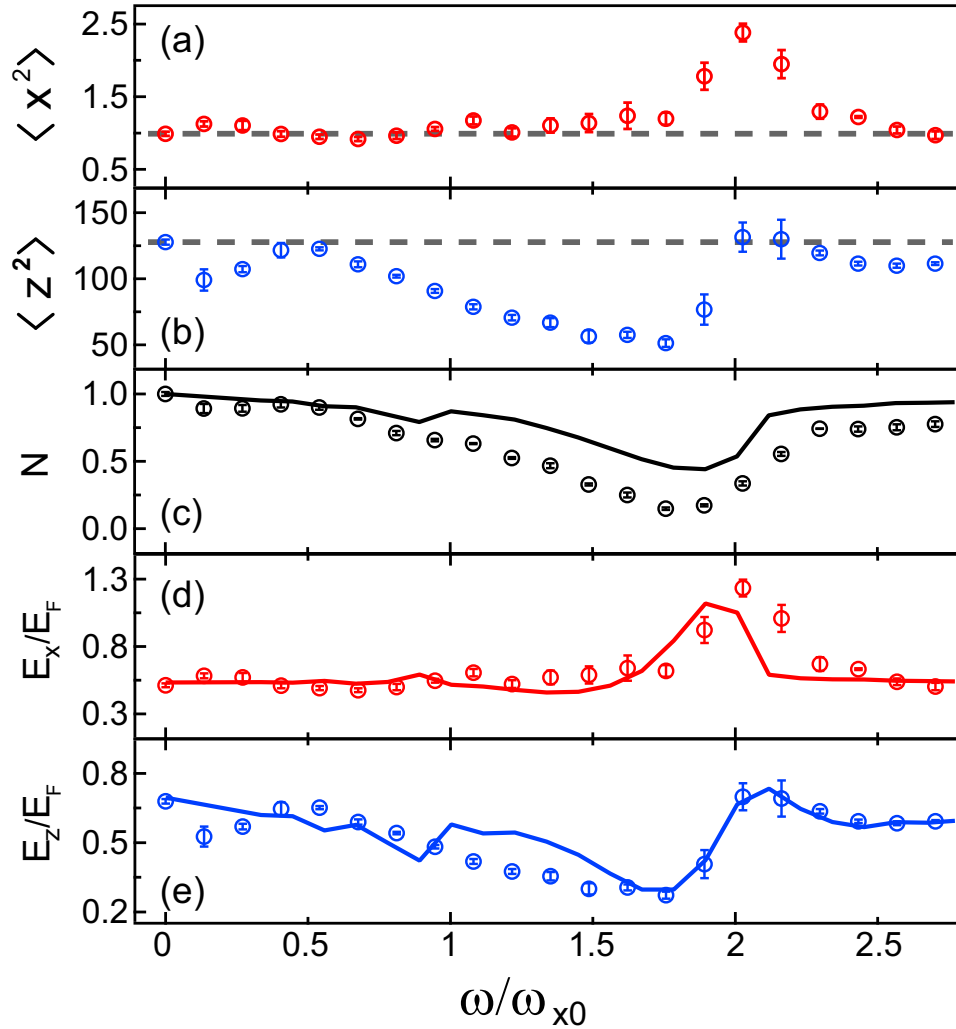


Figure 4.7. The dependence of parametric excitation on the modulation frequency. The radial and axial NIMS, the normalized atom number, and the radial and axial energies are shown from the top to the bottom. The harmonic frequency $\omega_{x0} = 2\pi \times 740$ Hz is the measured value. The dashed lines indicate the average value without parametric modulation ($\delta = 0$). The solid lines show the simulation results.

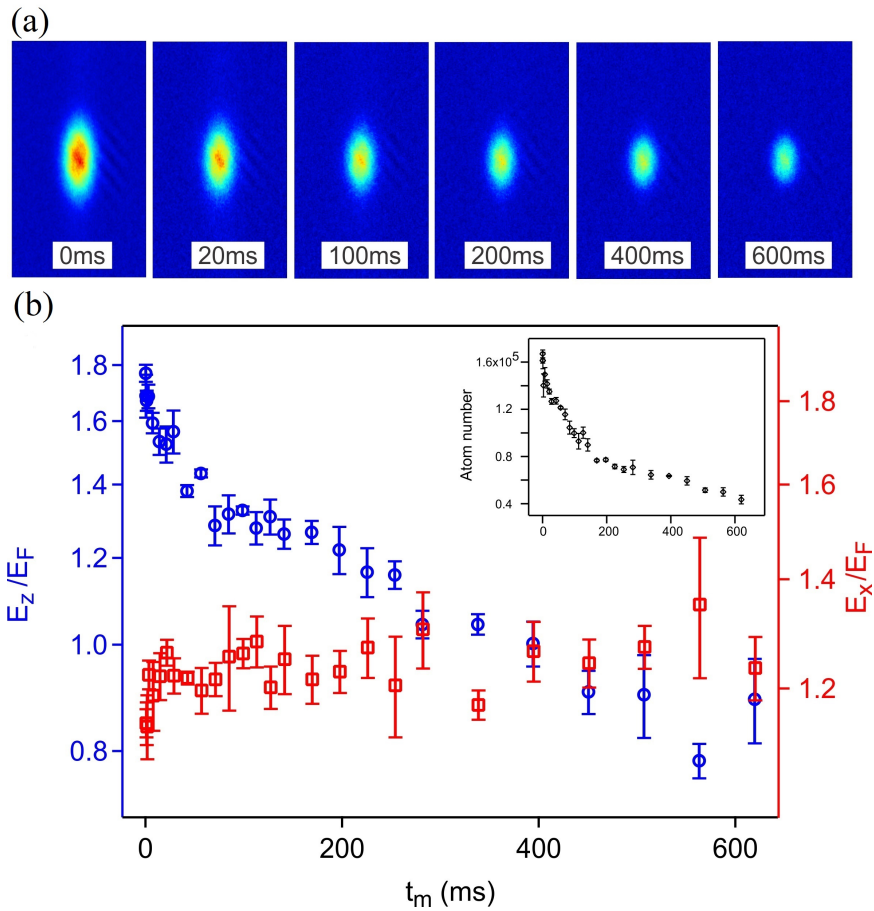


Figure 4.8. Time modulation with $\delta = 0.5$ and $\omega_m = 1.45\omega_x$. (a) The absorption images of the atomic clouds of various modulation times. (b) The dependence of $E(x, z)/E_F$ on modulation time (blue circles are for E_z/E_F and the red squares are for E_x/E_F). The inset figure is the atom number versus modulation time. Error bars represent one standard deviation.

For the simulation along a single axis, a constant value is used for the position of an atom in the other axis. The initial values necessary are trap depth U_0 , initial atom number N , degeneracy parameter T/T_F , mean trap frequency $\bar{\omega}$, modulation amplitude δ , modulation frequency ω_m , and modulation time t_m .

With the potential from the crossed-beam trap, the calculation is run as follows:

1. Discretize the trap space with an initial atom number N according to the Thomas-Fermi density distribution $n(x, t = 0)$ with phase $0 \leq \phi \leq 2\pi$ equally distributed among all atoms.
2. With initial conditions $0 \leq x(0) \leq \sigma_x$ and $x'(0) = 0$, solve Eq. 4.8 for $x(\phi, t_m)$ and $x'(\phi, t_m)$ for all individual atoms.
3. Calculate total energy $E = 1/2mx'(\phi, t_m)^2 + U(x(\phi, t_m))$ of each atom, where $U(x)$ is the crossed beam trap potential. After simulation t_m , atoms with energies $E \geq U_0$ are considered knocked out of the trap, and the final atom number is found. The final energy per particle is the average of all atoms left.
4. A new density profile $n(x, t_m)$ is calculated by summing the discretized trap space with the atoms left in the trap, then $\langle x^2 \rangle = N^{-1/3} \int x^2 n(x, t_m) dx$ is found.

5. ITINERANT FERROMAGNETISM IN A TWO-DIMENSIONAL FERMI GAS

In ferromagnetic transition elements such as iron, nickel, and cobalt, along with many of their alloys, itinerant electrons in the valence shells are free to move and rearrange themselves and create the magnetic order. This is a different mechanism from localized electrons models of ferromagnetism such as the Weiss and Heisenberg models. In the itinerant ferromagnetism dynamics, the Stoner model predicts itinerant ferromagnetism via a repulsive interaction parameter for high density of states at the Fermi energy. However, theoretical determination of the repulsive interaction parameter is very difficult in the transition elements because of their complex electronic structure. The Stoner model can be applied more directly to a system of trapped ultracold fermions in a bias magnetic field, where a zero-range repulsion between fermions is applicable [100].

Itinerant ferromagnetism has been searched for in a three-dimensional strongly interacting Fermi gas, but no direct evidenced has been found [29]. The ferromagnetic domains were believed to have formed due to the signatures predicted by the Stoner model. It was found later [30] that the repulsive polarons decayed into dimers before the ferromagnetic domains could form. Here I propose an experiment with a two-dimensional strongly interacting system as more favorable for the observation of itinerant ferromagnetism [101].

5.1 Stoner Model of Itinerant Ferromagnetism

The Stoner model describes the instability of a system of spin- $\frac{1}{2}$ particles toward ferromagnetism by the competition between kinetic and interaction energies. In the atomic gas considered here, no spin flipping occurs, so for the spin-balanced gas, the

total spin polarization is zero and the ferromagnetic phase is caused by the movement of spins within the gas.

The competition between interaction and kinetic energy in the Stoner model can be shown by a small increase (decrease) in the Fermi energy ϵ_F of spin up (spin down) atoms by $\delta\epsilon$ leading to an increase in local spin polarization. The number of spin up particles with energy $\delta\epsilon$ is $\int_0^{E_F+\delta\epsilon} \tilde{D}(\epsilon)d\epsilon \simeq \delta\epsilon \cdot \tilde{D}(\epsilon_F)$ and the increase in total kinetic energy of the gas is

$$\Delta E_K = (\delta\epsilon)^2 \cdot \tilde{D}(\epsilon_F) \quad (5.1)$$

where $\tilde{D}(\epsilon)$ is the density of states per spin at energy ϵ . The interaction energy of the system is $E_{int} = g \cdot N_\downarrow N_\uparrow / V$ where N_σ is the number of spin σ particles, g is the interaction exchange parameter $\frac{4\pi\hbar^2 a}{m}$ where a is the s-wave scattering length, V is the volume of the gas and m is the mass of the particles [70]. The initial interaction energy is given by $g(N_0/2)^2/V$ with $N_0 = N_\downarrow + N_\uparrow$ because for the balanced gas, $N_\downarrow = N_\uparrow = \frac{N_0}{2}$. The number of particles of spin σ is given by $N_\sigma = \int_0^{\epsilon_F\sigma} \tilde{D}(\epsilon)d\epsilon$ and so the change in interaction energy due to the change in ϵ_F is

$$\Delta E_{int} = \frac{g}{V} \left[\left(\frac{N_0}{2} + (\delta\epsilon)\tilde{D}(\epsilon_F) \right) \left(\frac{N_0}{2} - (\delta\epsilon)\tilde{D}(\epsilon_F) \right) - \left(\frac{N_0}{2} \right)^2 \right] \quad (5.2)$$

$$= -\frac{g}{V} \cdot (\delta\epsilon)^2 \cdot \tilde{D}^2(\epsilon_F), \quad (5.3)$$

and the total change in energy is

$$\Delta E_T = \tilde{D}(\epsilon_F) \cdot (\delta\epsilon)^2 \left(1 - \frac{g}{V} \cdot \tilde{D}(\epsilon_F) \right). \quad (5.4)$$

This indicates that for $\frac{g}{V} \cdot \tilde{D}(\epsilon_F) > 1$, the total energy decreases and the ferromagnetic order becomes more favorable. This is the Stoner criterion.

5.2 Mean-Field Treatment of Itinerant Ferromagnetism in an Atomic Fermi Gas

5.2.1 Three-Dimensional Gas

For a three-dimensional gas, the short-range interaction potential used in the mean-field treatment is $\frac{4\pi\hbar^2 a}{m}\delta(\mathbf{r})$, leading to interaction energy $E_{int} = \frac{4\pi\hbar^2 a}{m}Vn_\uparrow n_\downarrow$, where n_σ is the number density of spin- σ particles. For a trapped Fermi gas, the trap geometry should also be addressed in the potential, but for large enough clouds, the local-density approximation (LDA) is valid and the gas can be treated as uniform. For a uniform Fermi gas, the total energy is

$$E_T = E_{K\downarrow} + E_{K\uparrow} + \frac{4\pi\hbar^2 a}{m}Vn_\downarrow n_\uparrow, \quad (5.5)$$

where $E_{K\sigma}$ is the kinetic energy for spin σ particles. The kinetic energy at zero temperature for spin- σ is $\int_0^{E_{F\sigma}} \epsilon D(\epsilon) d\epsilon$ so

$$E_{K\downarrow} + E_{K\uparrow} = \frac{V}{2\pi^2} \left(\frac{2m}{\hbar^2} \right)^{3/2} (E_{F\downarrow}^{3/2} + E_{F\uparrow}^{3/2}), \quad (5.6)$$

where $E_{F\sigma} = \frac{\hbar^2 k_{F\sigma}^2}{2m}$ is the Fermi energy and $k_{F\sigma} = (6\pi^2 n_\sigma)^{1/3}$ is the Fermi wave-vector for spin σ . Defining the polarization of the gas as $\eta \equiv \frac{n_\uparrow - n_\downarrow}{n_\uparrow + n_\downarrow}$ and $n \equiv \frac{n_\uparrow + n_\downarrow}{2}$ as the average number density per spin, the total energy E_T is

$$E_T = 2VnE_F \left\{ \frac{3}{10} [(1 + \eta)^{5/3} + (1 - \eta)^{5/3}] + \frac{2}{3\pi} k_F a (1 + \eta)(1 - \eta) \right\}. \quad (5.7)$$

From Eq. 5.7, the total energy decreases with spontaneous polarization increase and this satisfies the Stoner criterion. The ferromagnetic phase transition occurs at the critical point where

$$\frac{\partial^2 E_T(\eta = 0)}{\partial \eta^2} = 0, \quad (5.8)$$

which occurs at $k_F a = \frac{\pi}{2}$. In Fig. 5.1(a), the total energy is seen to reach its minimum at $\eta = 0$ for $k_F a < \pi/2$. For $k_F a > \pi/2$, the minimum in total energy occurs for

increasing η until reaching full polarization at $\eta = 1$. Applying the requirements of $\frac{\partial E_T}{\partial \eta} = 0$ and $\frac{\partial^2 E_T}{\partial \eta^2} > 0$ for a local minimum in total energy, the polarization is

$$\eta(k_F a) = \begin{cases} 0 & k_F a < \frac{\pi}{2} \\ \frac{3\pi}{8k_F a}(1 + \eta)^{2/3} - (1 - \eta)^{2/3} & \frac{\pi}{2} \leq k_F a \leq \frac{3\pi}{4\sqrt[3]{2}} \\ 1 & k_F a > \frac{3\pi}{4\sqrt[3]{2}} \end{cases} \quad (5.9)$$

and the second-order phase transition can be observed through polarization as seen on the top of Fig. 5.1(a). The phase transition also leads to an increase in kinetic energy as shown in Eq. 5.1. In the fully polarized gas the repulsive interaction vanishes and the kinetic energy increases by $2^{2/3}$. At the phase transition the volume reaches a maximum due to the increase in kinetic energy and decrease in interaction energy, pictured in Fig. 5.1(b). The pressure of the gas is $P = -\frac{\partial E_T}{\partial V} = \frac{2}{3}E_K/V + E_{int}/V$, and considering a constant local pressure due to an approximately constant local trap potential, the volume must increase and reach a maximum at $k_F a = \pi/2$.

5.2.2 Two-Dimensional Gas

In two dimensions, the interaction exchange parameter from the mean-field model is $\frac{2\pi\hbar^2 a_{3D}}{ml} \sqrt{\frac{2}{\pi}} A$, where A is the area of the gas, and $l_z = \sqrt{\frac{\hbar}{m\omega_L}}$ is the oscillator length of the two-dimensional harmonic trap with trap frequency ω_L [101]. Following the methods of Sec. 5.2.1,

$$E_{int} = \frac{a}{l} \sqrt{\frac{2}{\pi}} n A E_F (1 + \eta)(1 - \eta). \quad (5.10)$$

The density of states in two dimensions is $\frac{m}{\pi\hbar^2}$ and the Fermi wave-vector is $k_F = \sqrt{4\pi n}$, so the total kinetic energy of the gas is

$$E_{K\downarrow} + E_{K\uparrow} = \frac{A}{2} n E_F [(1 + \eta)^2 + (1 - \eta)^2], \quad (5.11)$$

and the total energy in two dimensions is

$$E_T = \frac{A}{2} n E_F \left[(1 + \eta)^2 + (1 - \eta)^2 + \sqrt{\frac{8}{\pi}} \frac{a}{l_z} (1 + \eta)(1 - \eta) \right]. \quad (5.12)$$

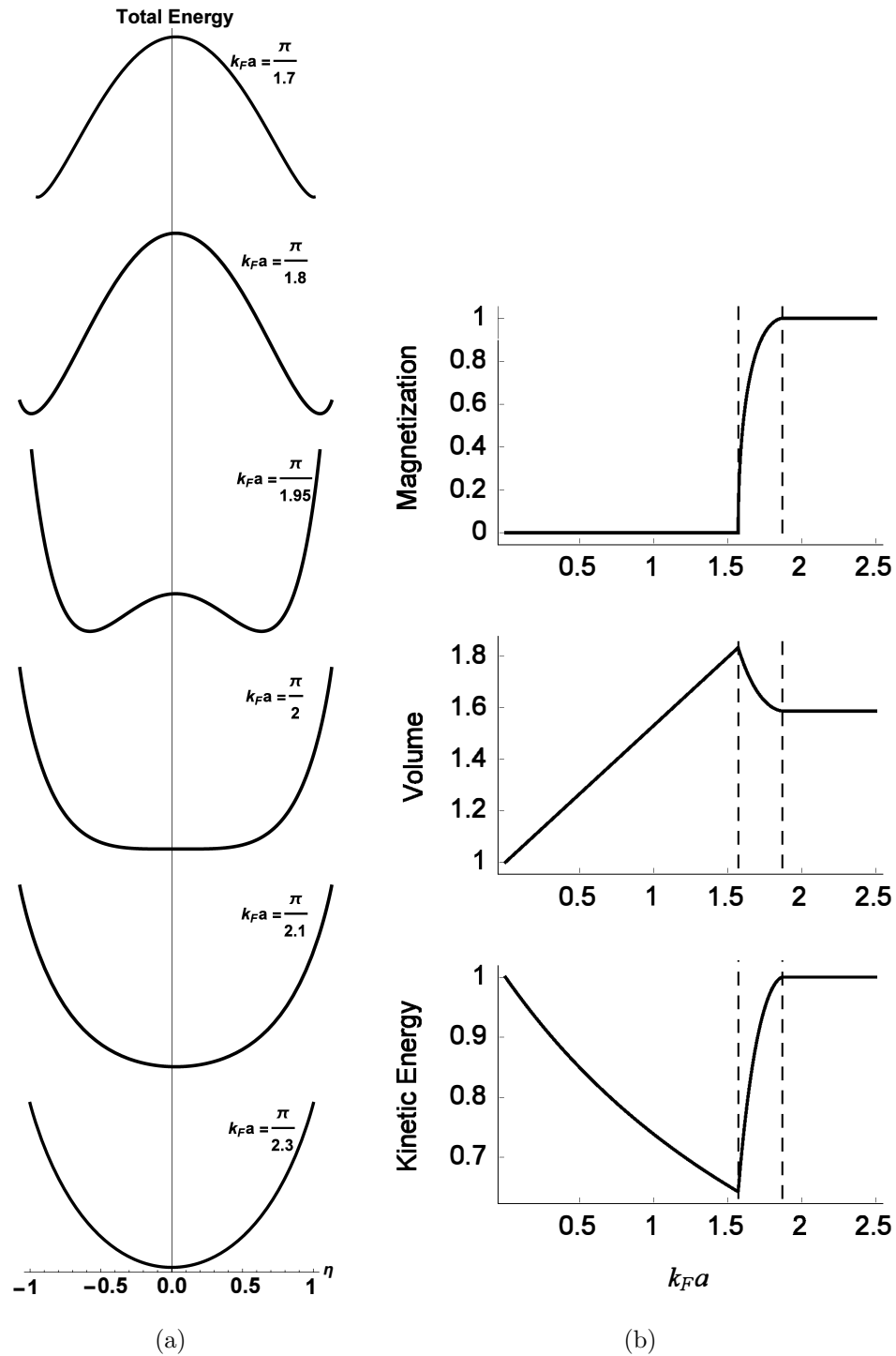


Figure 5.1. Stoner model properties for a three-dimensional system. (a) Total energy as a function of polarization. (b) Polarization, kinetic energy and volume. The kinetic energy is normalized to the total energy and the volume is normalized to the ideal gas volume. The dashed lines in (b) are for $k_F a = \pi/2$ and $k_F a = 3\pi/4\sqrt{2}$.

The ferromagnetic phase transition occurs at $\frac{a_{3D}}{l_z} = \sqrt{\frac{\pi}{2}}$. In two dimensions, it is observed that $\frac{\partial E_T}{\partial \eta}$ and $\frac{\partial^2 E_T}{\partial \eta^2}$ are not dependent on η so the onset of localized polarization occurs abruptly. The minimum of total energy only occurs at $\eta = 0$ for $\frac{a}{l_z} < \sqrt{\frac{\pi}{2}}$ and $\eta = 1$ for $\frac{a}{l_z} > \sqrt{\frac{\pi}{2}}$ as shown in Fig. 5.2(a). The first-order phase transition in polarization leads to a discontinuity in the kinetic energy of the gas at the critical point and a maximized volume for $\frac{a}{l_z} \geq \sqrt{\frac{\pi}{2}}$ as seen in Fig. 5.2(b).

5.2.3 Dimensional Dependence of Gas Properties

A comparison of the results from Sec. 5.2.1 and 5.2.2 reveals important differences between the two-dimensional and three-dimensional systems. These differences are used to signal the two-dimensional system as more favorable for the observance of itinerant ferromagnetism.

Sec. 5.2.1 shows that the three-dimensional gas depends upon η and $k_F a$ for its phase change, which is different for the two-dimensional gas that depends on η and a/l_z . This difference results from the dependence on k_F of the kinetic and interaction energies of the gas at different dimensions. From Eq. 5.7, the three-dimensional gas has $E_K \propto k_F^2$ and $E_{int} \propto k_F^3$, so the competition between the energies is dependent on the density of the gas. For the two-dimensional gas, in Eq. 5.12, the kinetic and interaction energies have the same k_F^2 dependence and so the parameter required for the phase change in two-dimensions is a/l_z .

The two-dimensional gas is seen to have a second-order phase shift signaled by the discontinuity in the local polarization at the critical point, as shown in Fig. 5.2(b). A discontinuity is also seen in the kinetic energy of the gas due to the η^2 dependence of the kinetic energy. In the three-dimensional system, the phase transition is of first-order and the local polarization increases continuously above the critical point as shown in Fig. 5.1(b). Due to the $\eta^{5/3}$ dependence of the kinetic energy, it increases continuously above the critical point and reaches a maximum at $\eta = 1$.

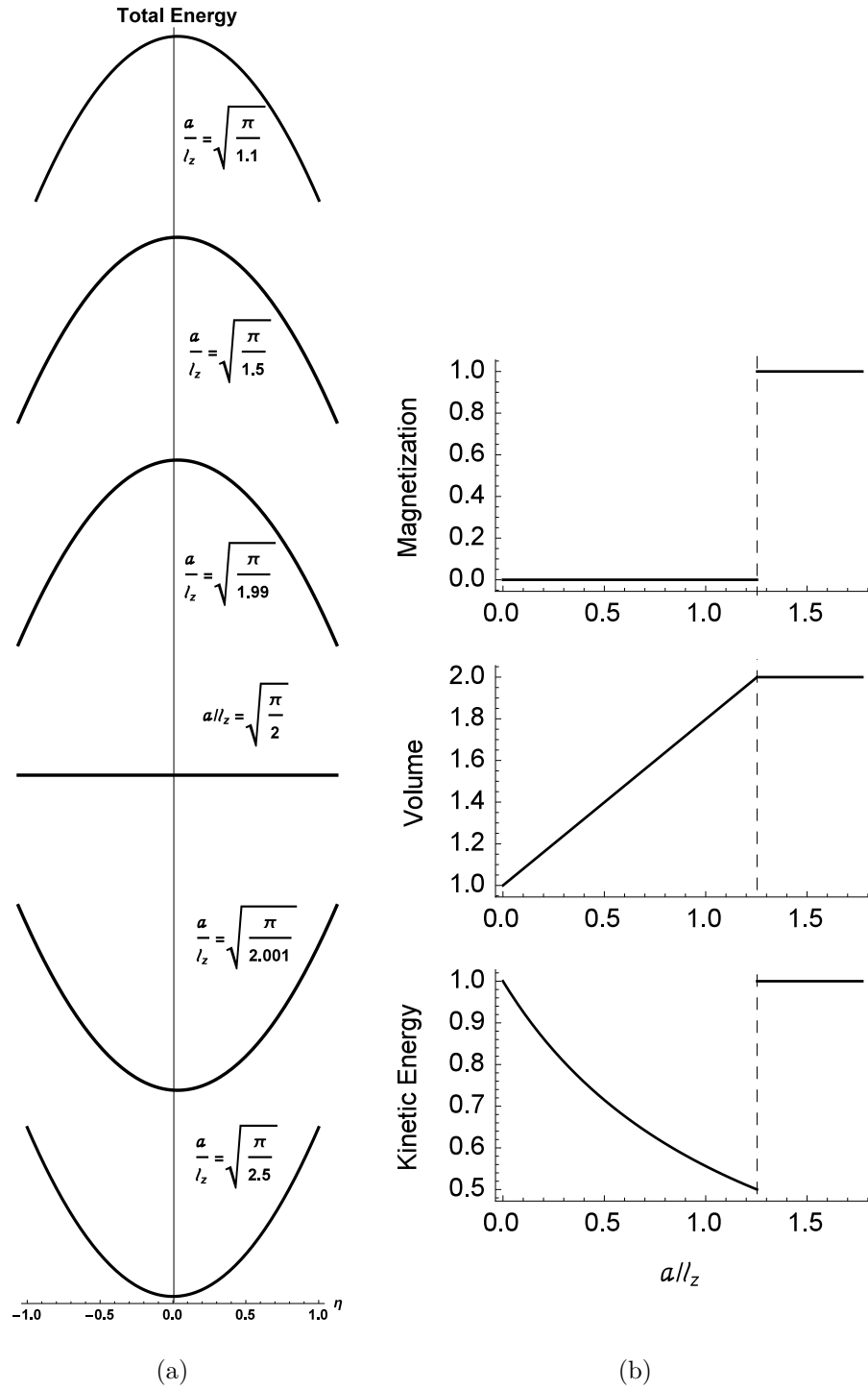


Figure 5.2. Stoner model properties for a two-dimensional system. (a) Total energy as a function of polarization. (b) Polarization, kinetic energy and volume. The kinetic energy is normalized to the total energy and the volume is normalized to the ideal gas volume. The dashed line in (b) indicates $a/l_z = \sqrt{\pi/2}$.

For $\eta = 1$, $E_{int} = 0$ independently of the dimension of the gas, but the kinetic energy has a different dependence at each dimension. In three dimensions the kinetic energy increases continuously above the critical point as the local density increases with increasing η and has a $2^{2/3}$ increase from its value at the critical point. In two dimensions, the kinetic energy has a discontinuity at the critical point, and above the critical point there is no dependence on the density of the gas. The value of the kinetic energy above the critical point increases to twice the value at the critical point.

The density dependence of the three-dimensional gas also leads to a maximum volume at the critical point. As E_{int} decreases faster than E_K increases above the critical point, the volume of the three-dimensional gas decreases above the critical point as η increases, as seen in Fig. 5.1(b). In the two-dimensional gas, the kinetic and interaction energies have the same dependence on density, so the change rate above the critical point is the same and the volume of the gas remains at a maximum above the critical point.

5.3 Experimental Search for Itinerant Ferromagnetism in a Three-Dimensional Atomic Fermi Gas

There have been two separate experiments conducted by the same group using a three-dimensional ${}^6\text{Li}$ gas and their results have led to different conclusions. Although neither experiment directly observed the formation of ferromagnetic domains, the experimental results first thought to signal the phase transition into itinerant ferromagnetism were later interpreted differently by the second experiment.

5.3.1 Review of First Experiment from MIT Group

In 2009, the first experiment searching for itinerant ferromagnetism in a three-dimensional Fermi gas was conducted by the Ketterle group at MIT [29], based on theoretical models such as those in Refs. [58, 59]. This experiment was believed to

observe itinerant ferromagnetism with ${}^6\text{Li}$ atoms by witnessing the kinetic energy minimum, volume maximum as predicted by the Stoner model with increasing repulsive interaction. A local polarization predicted by the Stoner model was claimed by a minimum in inelastic collisions.

Local polarization was determined by the suppression of inelastic collisions by way of the Pauli exclusion principle. Inelastic three-body collisions convert atoms into molecules and contribute to atom loss rate from the trap. The results showed a maximum loss rate at $k_F a \simeq 2.5$ at the lowest temperature in the experiment, with the critical point increasing with increasing temperature. In the Stoner model, the critical point is not temperature dependent, so the local polarization prediction must be explained otherwise.

A kinetic energy minimum was also found to be temperature dependent, unlike the Stoner model. The minimum value was found at $k_F a \simeq 2.2$ and $T/T_F = 0.12$. The increase in kinetic energy was only about 0.2, smaller than the predicted value of 0.59 when the gas is fully polarized. This result could not be explained but was believed to have been caused by experimental procedures.

The volume of the gas reached a maximum at $k_F a \simeq 2.2$ for $T/T_F = 0.12$, but the gas contained up to 25% dimers. The presence of dimers increases the volume of the gas and the interaction between dimers and atoms disturbs the formation of ferromagnetic domains. The ferromagnetic domains were not observed in this experiment, but given the $3 \mu\text{m}$ resolution of their imaging system, a domain size of approximately $5 \mu\text{m}^3$ containing about 50 atoms is predicted by the experiment. The lifetime of the proposed ferromagnetic phase was no longer than 20 ms, which was explained by inelastic collisions. The results of this experiment did not validate the Stoner model, but were not enough to show the existence of a ferromagnetic phase in a three-dimensional Fermi gas.

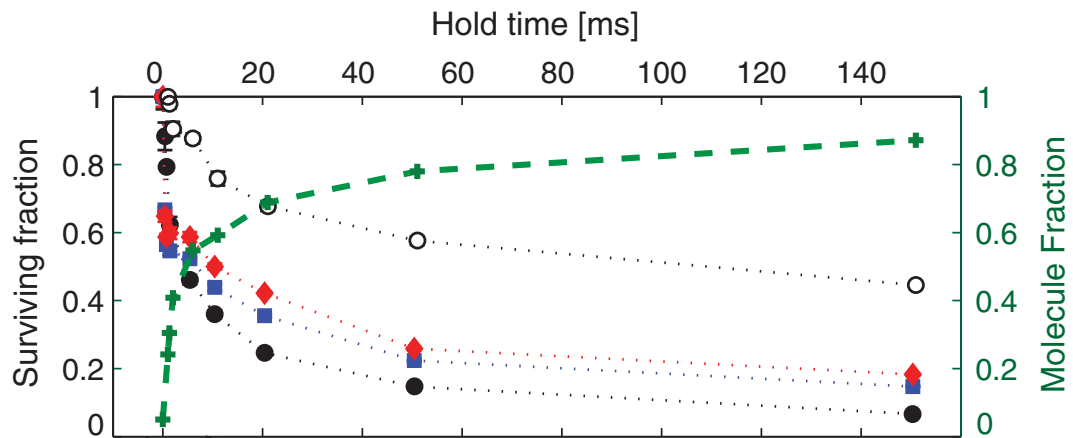


Figure 5.3. Characterization of molecule formation at short and long hold times, and at different values of the interaction strength. The closed symbols—circles (black) at 790 G with $k_{Fa} = 1.14$, squares (blue) at 810 G with $k_{Fa} = 2.27$, and diamonds (red) at 818 G with $k_{Fa} = 3.5$, represent the normalized number of free atoms, while the open symbols represent the total number of atoms, including those bound in Feshbach molecules (open circles at 790 G with $k_{Fa} = 1.14$). The crosses (green) show the molecule fraction. Image taken from Ref. [30]

5.3.2 Review of Second MIT Group Experiment

The conclusion of the first experiment was disputed by Ref. [30], which showed by using speckle imaging that what was observed in the previous experiment was the formation of dimers and not ferromagnetic domains. The measured spin fluctuations and instability of the repulsive gas led to the conclusion that itinerant ferromagnetism cannot occur in a three-dimensional atomic Fermi gas. The main result showing the pair formation is shown in Fig. 5.3.

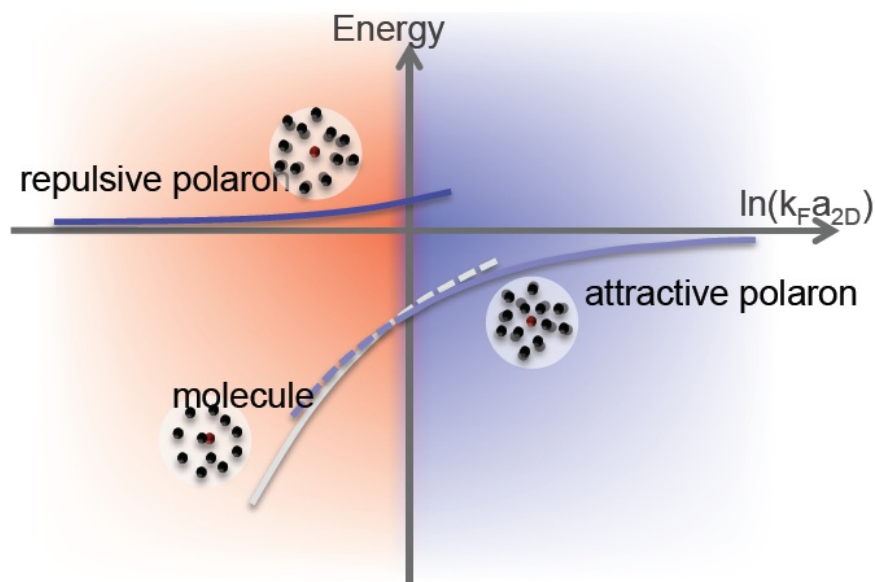


Figure 5.4. Phase diagram for strongly interacting Fermi gas in two dimensions. Image taken from Ref. [102].

The speckle imaging technique is used to measure spin fluctuations in a two-spin system and the spin susceptibility is then determined from the spin fluctuations [103]. The experiment had an imaging resolution of about $2.5 \mu\text{m}$ and did not observe a dramatic increase in the spin fluctuation of the gas as the repulsive interaction was increased, signaling that no ferromagnetic domains were formed. The spin fluctuation here is not caused by spin flipping, but by the movement of spins trying to form ferromagnetic domains.

The formation of domains large enough to be imaged by the $2.5 \mu\text{m}$ resolution imaging system is predicted to occur at $\simeq 300 \mu\text{s}$ with domains containing in the order of tens of atoms after a few ms [104]. Using speckle imaging with a minimum hold time of $350 \mu\text{s}$, no considerable spin fluctuation occurred at various hold times, signaling that no domains were formed.

This experiment concluded that a three-dimensional atomic Fermi gas with strong short-range interactions remains in a paramagnetic phase due to the rapid decay into dimers. The Stoner model does not include the competition between dimer formation and ferromagnetic domains, therefore the experiments were not suitable for the study of itinerant ferromagnetism in a three-dimensional atomic Fermi gas following the Stoner model.

The lifetime of the repulsively interacting gas has proved to be the determining factor for the possibility of itinerant ferromagnetism to occur in an atomic Fermi gas. In 2012, experiments with atomic Fermi gases discovered repulsive polarons in two [102] and three [105] dimensions, and the repulsive polaron's lifetime dependence on dimensionality has predicted a longer lifetime for a two-dimensional gas, which may be more suitable for the study of itinerant ferromagnetism. In two dimensions, the atom loss rate due to spin fluctuations is also predicted to be smaller than in three dimensions [101], providing a longer repulsively interacting gas lifetime.

5.4 Repulsive Polaron in an Atomic Fermi Gas

The many-body interaction of spin impurities in a Fermi sea with attractive or repulsive interactions gives rise to the formation of polarons [106]. Repulsive polarons were first observed in a three-dimensional ultracold Fermi gas by RF-spectroscopy [105] and in two dimensions using momentum-resolved photo-emission spectroscopy [102] (phase diagram on Fig. 5.4).

With no itinerant ferromagnetism observed in three dimensions, there are predictions of spatial confinement leading to a ferromagnetic phase change in two dimensions caused by longer stability of repulsive polarons.

The approach of treating a minority particle in a Fermi sea with the variational method used here was first proposed by Chevy [107]. The proposed Hamiltonian for spin- $\frac{1}{2}$ fermions at zero-temperature with short-range interactions in a dilute gas with interparticle distance $1/k_F$ is

$$H = \sum_{\mathbf{k},\sigma} \epsilon_{\mathbf{k}} \hat{a}_{\mathbf{k},\sigma}^\dagger \hat{a}_{\mathbf{k},\sigma} + \frac{g}{V} \sum_{\mathbf{k},\mathbf{k}',\mathbf{q}} \hat{a}_{\mathbf{k}+\mathbf{q},\uparrow}^\dagger \hat{a}_{\mathbf{k}'-\mathbf{q},\downarrow}^\dagger \hat{a}_{\mathbf{k}',\downarrow} \hat{a}_{\mathbf{k},\uparrow}, \quad (5.13)$$

where k, k' , and q are momenta, $\epsilon_k = \hbar^2 k^2 / 2m$ is the kinetic energy of a particle with momentum k , $\hat{a}_{k,\sigma}$ is the annihilation operator for particle with momentum k and spin σ , and g is the interaction parameter. In the mean-field theory, $\frac{1}{g} = \frac{m}{4\pi\hbar^2 a} - \frac{1}{V} \sum_k \frac{1}{2\epsilon_k}$, where s -wave scattering from the pseudo-potential $\frac{4\pi\hbar^2 a}{m} \delta(r) \frac{\partial}{\partial r} (r\psi(r))$ [71] is used. The trial wavefunction for the polaron with zero momentum is

$$|\Psi\rangle = \phi_0 |0\rangle_\downarrow |FS\rangle_\uparrow + \sum_{\substack{k>k_F \\ q<k_F}} \phi_{\mathbf{k},\mathbf{q}} \hat{a}_{\mathbf{k},\uparrow}^\dagger \hat{a}_{\mathbf{q},\uparrow} |\mathbf{q}-\mathbf{k}\rangle_\downarrow |FS\rangle_\uparrow. \quad (5.14)$$

The first term of the wavefunction accounts for a non-interacting impurity $|0\rangle_\downarrow$ with zero momentum in a Fermi sea of net zero momentum $|FS\rangle_\uparrow$. The second term describes a single particle-hole excitation between the impurity atom and the Fermi sea. In the second term, an impurity knocks a particle out of the Fermi sea with momentum k , creating a hole with momentum $-\mathbf{q}$. The impurity gains momentum $\mathbf{q}-\mathbf{k}$, thus conserving the total momentum of the system. To find the ground state energy, the quantity $\langle\Psi|\hat{H}|\Psi\rangle - E_p \langle\Psi|\Psi\rangle$ must be minimized by varying ϕ_0 and $\phi_{\mathbf{k},\mathbf{q}}$ under the constraint of wavefunction normalization

$$\langle\Psi|\Psi\rangle = |\phi_0|^2 + \sum_{\substack{k>k_F \\ q<k_F}} |\phi_{\mathbf{k},\mathbf{q}}|^2 = 1.$$

The polaron energy and quasiparticle weight are respectively given by

$$E_p = \frac{1}{V} \sum_{q < k_f} f(E_p, \mathbf{q}) \quad (5.15)$$

$$Z_{\pm} \equiv |\phi_0|^2 = \left(1 - \frac{\partial}{\partial E} \frac{1}{V} \sum_{q < k_F} f(E_{\pm}, \mathbf{q}) \right)_{E_{\pm} = E_p}^{-1}, \quad (5.16)$$

with $f(E, \mathbf{q})$ the s -wave scattering amplitude as

$$f^{-1}(E, \mathbf{q}) = \frac{1}{g} + \frac{1}{V} \sum_{k > k_F} \frac{1}{\epsilon_{\mathbf{k}} - \epsilon_{\mathbf{q}} + \epsilon_{\mathbf{q}-\mathbf{k}} - E}. \quad (5.17)$$

The quasi-particle weight Z is a measure of how much of the non-interacting particle is contained in the wavefunction. This quantity is required for the calculation of the repulsive polaron lifetime and experimentally useful for determining the Rabi frequency used to prepare the repulsive polarons [105].

5.4.1 Spectrum and Lifetime of Polaron in Three Dimensions

The three-dimensional polaron energy is found from the implicit equation [108]

$$\frac{E_p}{E_F} = \Sigma \left(\frac{E_p}{E_F} \right) = -2 \int_0^1 \frac{y^2 dy}{1 - \frac{\pi}{2k_F a} - I \left(\frac{E_p}{E_F}, \frac{q}{k_F} \right)} \quad (5.18)$$

$$I(\epsilon, y) = \int_1^{\infty} \left[\frac{x}{2y} \text{Ln} \left(\frac{2x^2 + 2xy - \epsilon}{2x^2 - 2xy - \epsilon} \right) - 1 \right] dx,$$

with $x = q/k_F$. The energy spectrum is shown in Fig. 5.5(a) with excellent agreement with experiment and the quasi-particle weight spectrum is seen in Fig. 5.5(b) and agrees well with experimental results [105].

The repulsive polaron decays into dimers in the BEC limit (large $k_F a$) and into attractive polaron in the unitarity limit ($-1 \leq k_F a \leq 1$). The polaron-polaron decay rate is given by

$$\Gamma_{pp} = -Z_+ \text{Im} [\Sigma^-(E_+)], \quad (5.19)$$

with

$$\Sigma^-(E_+) = -2 \int_0^1 \frac{y^2 dy}{1 - \frac{\pi}{2k_F a} - Z_- \cdot I^* \left(\frac{\Delta E}{E_F}, \frac{q}{k_F} \right)}, \quad (5.20)$$

where $\Delta E = E_+ - E_-$ and $I^* \left(\frac{\Delta E}{E_F}, \frac{q}{k_F} \right)$ is derived from

$$f^{-1*}(E, \mathbf{q}) = \frac{1}{g_b} + \frac{1}{V} \sum_{k > k_F} \frac{1}{\epsilon_{\mathbf{k}} - \epsilon_{\mathbf{q}} + \epsilon_{\mathbf{q}-\mathbf{k}}^* - E} \quad (5.21)$$

and $\epsilon_{q-k}^* = \hbar^2(\mathbf{q} - \mathbf{k})^2/2m_-^*$ with m_-^* as the effective mass of the attractive polaron [109].

Fig. 5.5(c) shows the decay rate of the repulsive polaron into the attractive polaron on the BEC side of the energy spectrum. The result from the variational method above is comparable with Ref. [110]. Repulsive polaron decay via three-body recombination has been determined theoretically [111] and experimentally [112], but is not considered here due to the Stoner criterion occurring in the $k_F a$ region where polaron-polaron decay is dominant.

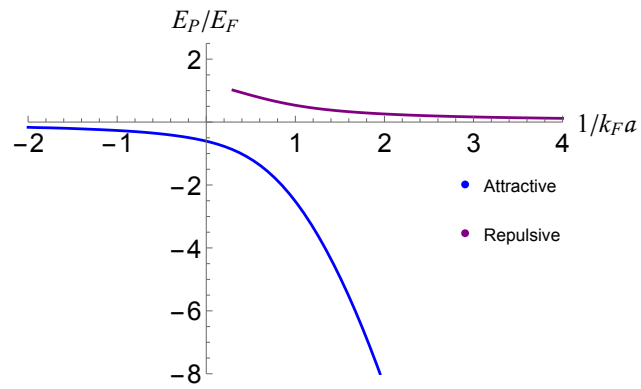
5.4.2 Spectrum and Lifetime of Polaron in Two Dimensions

Using the variational method, the polaron energy in terms of the Fermi energy is given as the self-energy [113]

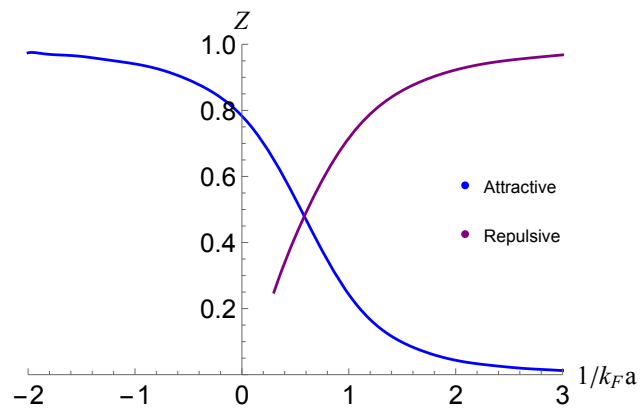
$$\epsilon = \Sigma(\epsilon) = -2 \int_0^1 \frac{du}{-\ln\left(\frac{E_b}{E_F}\right) + \ln \left[\sqrt{\left(1 - \frac{\epsilon}{2}\right)^2 - u} + \left(1 - \frac{\epsilon}{2}\right) - \frac{u}{2} \right]}, \quad (5.22)$$

where $E_b = \hbar^2/ma_{2D}$ is the dimer binding energy and $\epsilon = E_p/E_F$. Fig. 5.6(a) shows the energies of the repulsive and attractive polarons in terms of the Fermi energy compared with the perturbation method of Ref. [114], and Fig. 5.6(b) shows the quasi-particle weight for the two-dimensional polaron necessary for lifetime calculations. The calculated energy spectrum and quasi-particle weight are in excellent agreement with the results from [115].

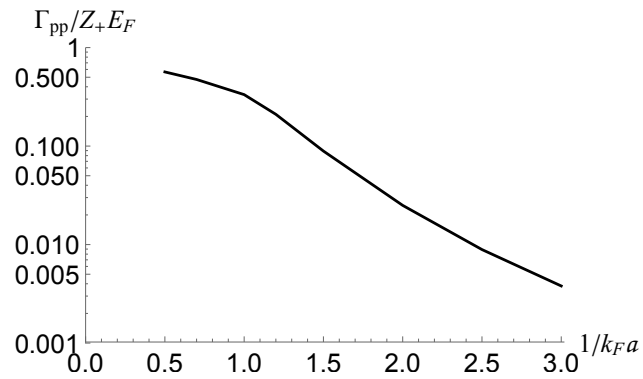
The decay rate of the repulsive polaron into the attractive polaron is shown in Fig. 5.6(c) and the results from the variational method above are comparable with the results from Ref. [116].



(a)

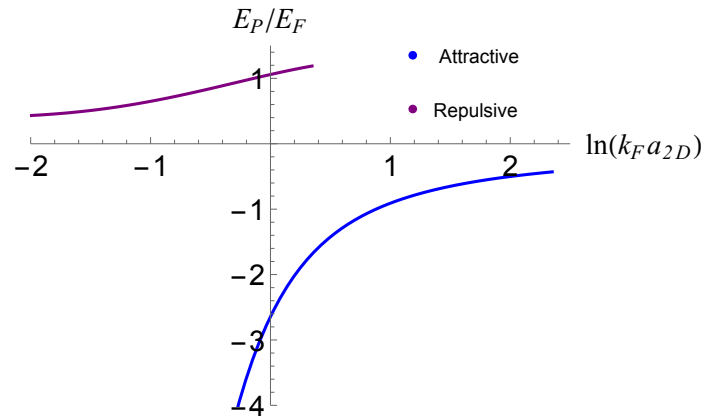


(b)

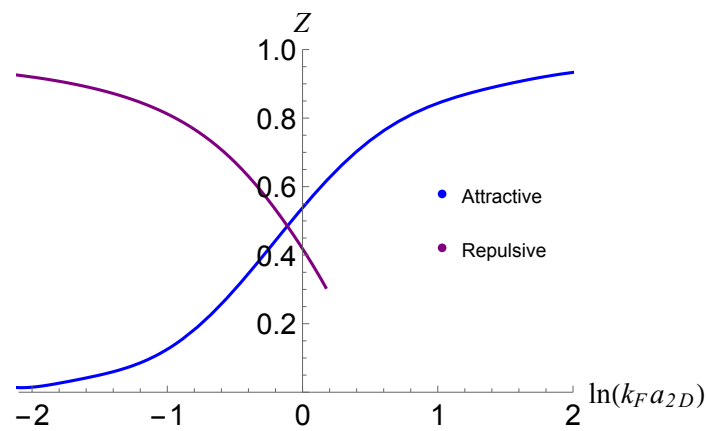


(c)

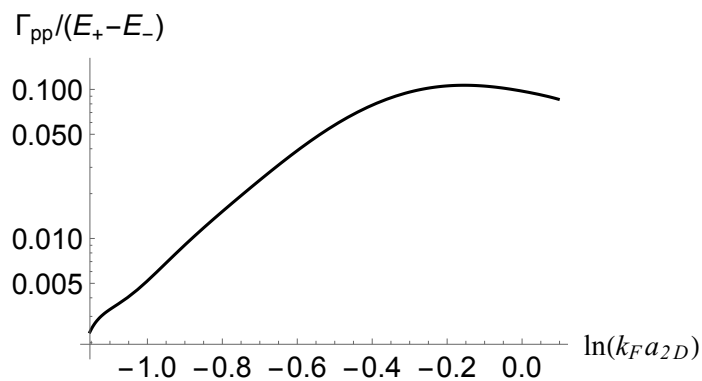
Figure 5.5. Three-dimensional polaron characteristics. (a) Energy spectrum. (b) Quasiparticle weight. (c) Lifetime of polaron against attractive polaron decay. The plots are based on theory from Refs. [108, 110].



(a)



(b)



(c)

Figure 5.6. Two-dimensional polaron characteristics. (a) Energy spectrum . (b) Quasiparticle weight. (c) Lifetime of polaron against attractive polaron decay. The interaction parameter is $\ln(k_F a_{2D}) = -\ln(E_b/E_F)/2$. The plots are based on theory from Refs. [113, 116].

5.4.3 Search of Ferromagnetism in a Two-Dimensional Fermi Gas

A proposed experiment will use a crossed-beam optical dipole trap with Gaussian beams from a single-mode laser at $\lambda = 1064$ nm wavelength and \hat{z} -polarized to create an optical one-dimensional lattice with potential [89]

$$U(x, y, z) \simeq -4U_0 \cos^2(ky \sin\theta) [1 - 2x^2\omega_x^2 - 2y^2\omega_y^2 - 2z^2\omega_z^2], \quad (5.23)$$

where the trapping frequencies due to the Gaussian beams are given by Eq. 3.11 with angle $2\theta = 35^\circ$ between the z -polarized Gaussian beams of waist $w_0 = 100$ μm , single beam Rayleigh range z_R and single beam trap depth U_0 to create the one-dimensional optical lattice in the y -direction with lattice constant $d = \lambda/2\sin\theta$. In this potential, the atoms are confined to the anti-nodes of the standing wave created by the crossed beams. The created ‘‘pancakes’’ occupy a space in the lattice where atoms are confined to two dimensions in the x - z plane. For the optical lattice, the harmonic approximation leads to trap frequency $\omega_L = \frac{4\sin\theta}{h}\sqrt{U_0 E_R}$ with recoil energy $E_R = \hbar^2(2\pi)^2/2m\lambda^2$ of an atom in the trap. Neglecting the three-dimensional Gaussian trapping potential (the term in brackets in Eq. 5.23), the lattice potential is given by

$$U_{lat} = -4U_0 \cos^2(ky \sin\theta) = -sE_R \cos^2(ky \sin\theta), \quad (5.24)$$

where $s = (\hbar\omega_L/2E_R \sin\theta)^2 = 4U_0/E_R$. The optical lattice creates a band structure for the allowed energies of the atoms in terms of the quasimomentum q . The Bloch bands are shown in Fig. 5.7 for various trap depths, with the band gap energies increasing with increasing trap depth. Knowing the band gap energy is essential for loading a three-dimensional gas trapped by Gaussian beams into a one-dimensional lattice and creating a two-dimensional gas. In order to keep the gas in two dimensions, a few conditions listed below must be met.

The first condition is that the atoms have energy $E_{F2D}, k_B T < \hbar\omega_L$ to guarantee the energy of the trapped atoms in the two relevant energy scales remains in the first excited band or in the harmonic approximation, to keep all atoms in the ground state in the lattice direction. Experimentally, these conditions are satisfied by isentropic

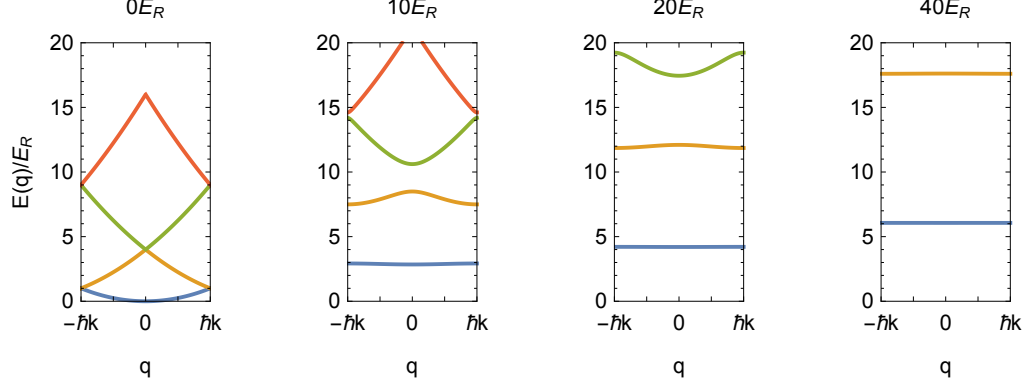


Figure 5.7. First Brillouin zone energy bands for a one-dimensional optical lattice created with laser of wave vector $k = 2\pi/\lambda$. The increasing trap depth creates smaller energy band depths with larger energy gaps.

loading of the optical lattice from a three-dimensional degenerate Fermi gas [117,118]. The Fermi energy for the whole trap is $E_{F,2D} = (16\pi N/15\sin\theta)^{2/5} \frac{(\hbar\bar{\omega})^{6/5}}{E_R^{1/5}}$, with atom number N and $\bar{\omega}$ being the mean trapping frequency. The $E_{F,2D} < \hbar\omega_L$ condition also sets a limit on the maximum number of atoms allowed in the trap, which leads to $E_{F,2D} = \sqrt{N}\hbar\omega_\perp$ for a single pancake where $\omega_\perp = \sqrt{\omega_x\omega_z}$, and leads to the condition $N < (\frac{\omega_L}{2\omega_\perp})^2$. These conditions are required to keep all atoms below the first excited state of the trap. The trapping potential and relevant energies are illustrated in Fig. 5.8.

The second condition is that the tunneling time for atoms in the first band to tunnel into an adjacent pancake must be larger than the experimental time to guarantee a two-dimensional system. The tunneling time is estimated by $t \sim \hbar/J$, where $J = (E_{\hbar k}(s) - E_0(s))/4$ [119] is the probability of an atom in the first band tunneling to an adjacent pancake, and the dependence on s is shown in Fig. 5.9. The experimental trapping laser beam requirements to satisfy all criteria for the two-dimensional gas are shown in Fig. 5.10.

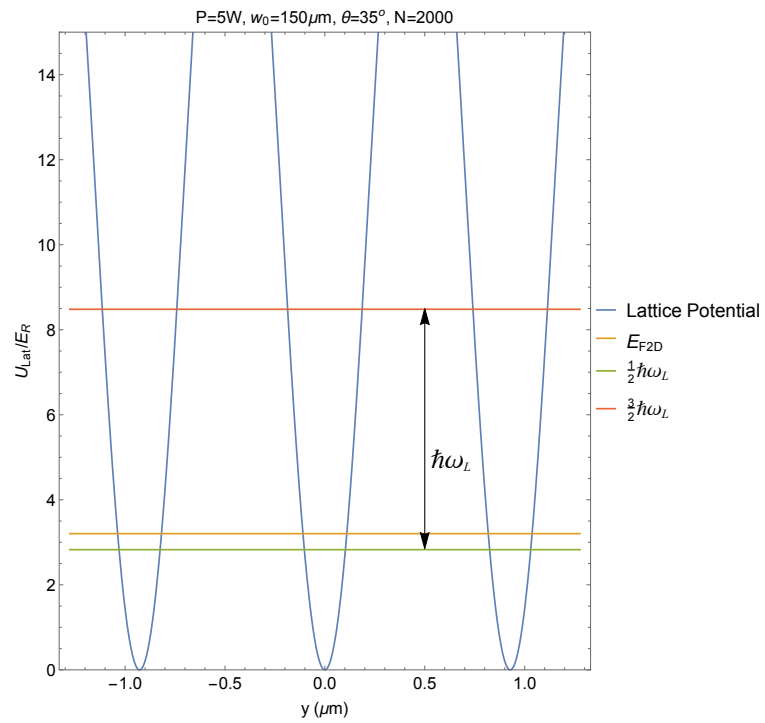


Figure 5.8. Lattice potential illustrating the relevant energies for confined two-dimensional motion.

5.4.4 Preparation of Repulsive Polaron

Once a two-dimensional system is established, the interaction strength between atoms of opposing pseudo-spin is controlled by tuning the Feshbach resonance via an applied bias magnetic field [16]. As shown in Sec. 5.4.2, the two-dimensional polaron energy is a function of the dimer binding energy E_b , which by [119]

$$\frac{l_z}{a_{3D}} = \int_0^\infty \frac{du}{\sqrt{4\pi u^3}} \left(1 - \frac{e^{-uE_b/\hbar\omega_L}}{\sqrt{(1 - e^{-2u})/2u}} \right), \quad (5.25)$$

is required to find the relationship between experimentally tunable parameters l which is the oscillator length of the two-dimensional trap and the three-dimensional scattering length a_{3D} . In two-dimensions, $\ln(k_F a_{2D})$ is the interaction parameter determined from the scattering amplitude which leads to binding energy $E_b = \hbar^2/m a_{2D}^2$ [120]. From $E_b/E_{F2D} = 2/(k_F a_{2D})^2$, the interaction parameter can be written in terms of experimental parameters as $\ln(k_F a_{2D}) = \ln\left(N^{1/4} \sqrt{\frac{\lambda}{\pi w_0 \sqrt{\sin\theta}} \left(\frac{\hbar\omega_L}{E_b}\right)}\right)$. As shown in Sec. 5.4.2, the region of interest for the repulsive two-dimensional polaron is $-1.65 \leq \ln(k_F a_{2D}) \leq -0.35$, with the longer lifetime occurring at the larger negative value.

The preparation of the repulsive polaron follows the methods of Ref. [102] with the relevant ${}^6\text{Li}$ parameters. Starting with a $|1\rangle$ - $|2\rangle$ gas at 633 G, an RF pulse of frequency 83.3 MHz is applied for the $|2\rangle \rightarrow |3\rangle$ transition, creating the repulsive $|1\rangle$ - $|3\rangle$ polaron. The field is then raised above 633 G to map the ferromagnetic instability at values of $a_{3D}/l_z > \sqrt{\pi/2}$. With ferromagnetic instability occurring at $a_{3D}/l_z = \sqrt{\pi/2}$, as shown in Fig. 5.11 the ferromagnetic phase would occur at $B = 633$ G with $\ln(k_F a_{2D}) = -0.8$.

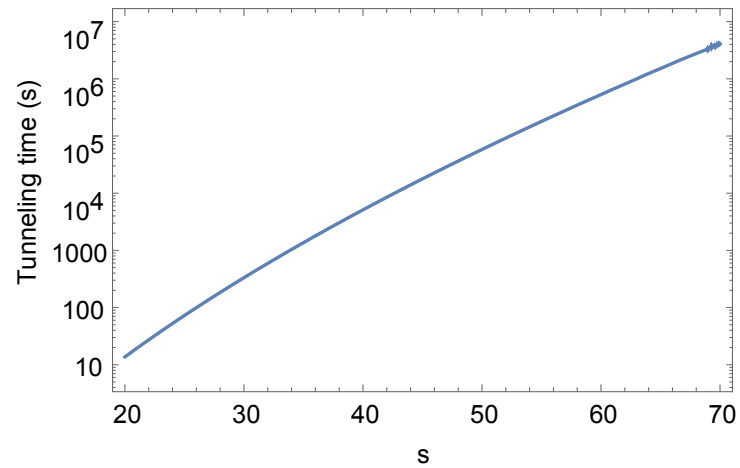


Figure 5.9. Tunneling time to adjacent pancake with $2\theta = 35^\circ$, and $w_0 = 100 \mu\text{m}$.

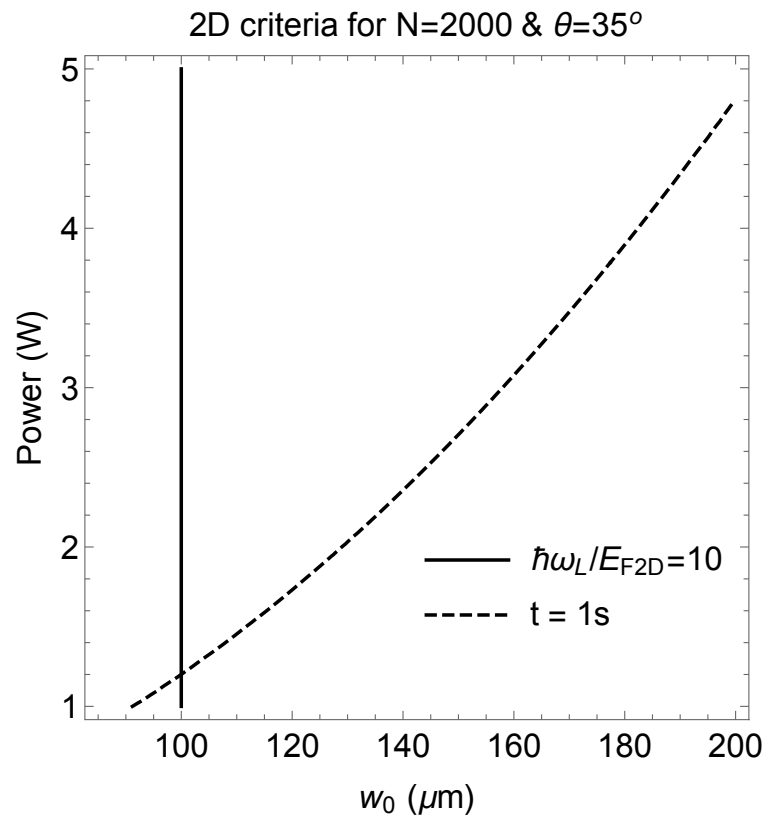


Figure 5.10. The region to the left of solid line does not satisfy the Fermi energy criterion; between the solid and dashed lines both conditions are satisfied; and region to the right of the dashed line does not satisfy the tunneling criterion.

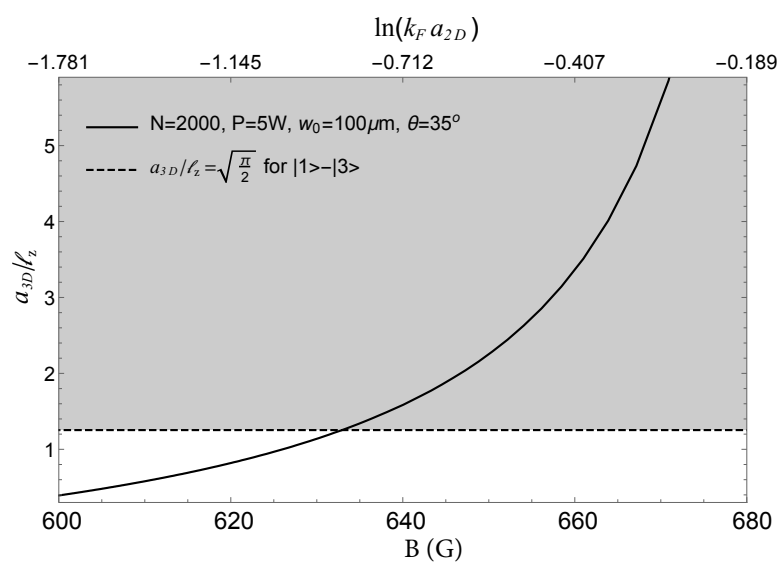


Figure 5.11. Ferromagnetic instability threshold in the gray region.

6. ABSOLUTE ABSORPTION OF A LITHIUM VAPOR CELL

6.1 Theory

An atomic vapor cell of isotopically pure ${}^6\text{Li}$ vapor has been applied to study the absolute absorption of a single frequency light near lithium D_2 lines. To simulate the system, a model system is proposed as follows: first, the energy levels of ${}^6\text{Li}$ D_2 lines are approximated to an effective three-level Λ system; second, a quantum master equation of atomic density matrix is used to describe the dynamics of the Λ system; then a set of rate equations of the atomic populations are extracted from the master equation; finally, the coupled equations are solved numerically in a self-consistent manner for optical beam evolution in space. The simulation result provides a benchmark for the experimental result presented in Sec. 6.4.

6.1.1 Effective Three-Level Model

The absorption of a monochromatic π -polarized laser light near the D_2 transition frequency is induced by the transition between multiple hyperfine states of the ground and excited manifolds. In principle, the absorption contribution from each hyperfine transition should be treated individually. However, in our experiment, lithium is heated to a temperature around 340°C , where the Doppler broadening is about 3 GHz, much larger than hyperfine splitting of energy levels in both ground states and the excited state (228.2 MHz for the ground levels and 4.4 MHz for the excited ones). In such conditions, the composite level model is valid comparing to that of full levels [42, 121], so the population ratio calculated by the full level model is close to the composite one as shown in the previous work of the D_1 transition of ${}^6\text{Li}$ [42].

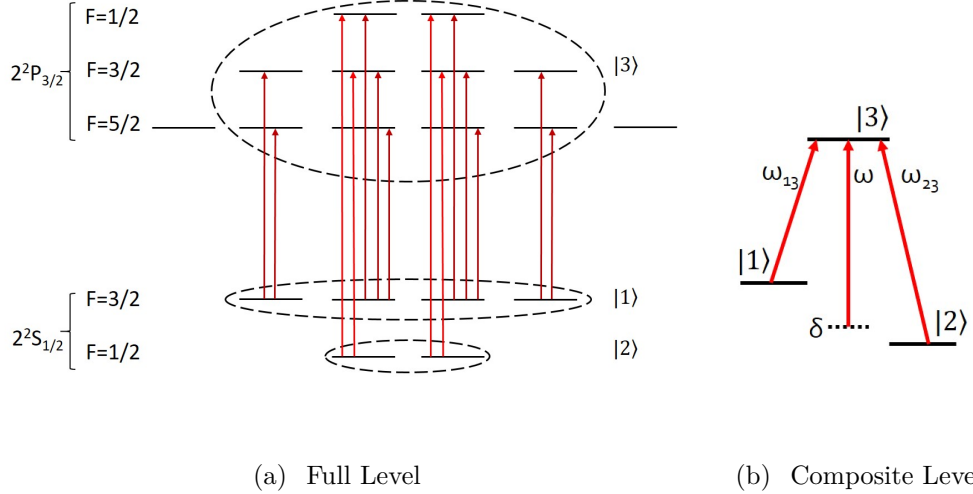


Figure 6.1. ${}^6\text{Li} - D_2$ Diagram. A π -polarized, monochromatic light stimulates both $|1\rangle \rightarrow |3\rangle$ and $|2\rangle \rightarrow |3\rangle$ transitions. The full level model in (a) is simplified to the composite level model in (b). δ is the laser detuning from the transition between average of ground states to excited state. Energy levels are not drawn to scale.

As described in Fig. 6.1, our composite three level model for π -polarized transitions forms a Λ quantum system, where the excited states $|3\rangle$ includes 10 out of 12 hyperfine levels in the excited state $2^2P_{3/2}$. The first ground state $|1\rangle$ contains all four levels of $2^2S_{1/2} |F = 3/2\rangle$, and the second ground state $|2\rangle$ has both 2 levels of $2^2S_{1/2} |F = 1/2\rangle$. Note that all Zeeman levels, as well as all $2^2P_{3/2}$ levels, are treated as degenerate, since our experiment is implemented in weak magnetic field where the Zeeman splitting is much less than the hyperfine splitting between $|1\rangle$ and $|2\rangle$.

To describe the atomic absorption using the composite level model, we need to find the effective Rabi frequencies of the composite level transitions as well as the branching ratio of radiative decays. For the Rabi frequency $\Omega_{ab} = \mu_{ab}E/\hbar$, where μ_{ab} is the electric-dipole transition matrix element for state a and b , and E is the electrical field strength of the laser field. μ^2 is additive, so $\mu_{13}^2 = \frac{8}{3}\mu_0^2$ by adding 10 π -transitions together, and $\mu_{23}^2 = \frac{4}{3}\mu_0^2$ with four π -transitions, where μ_0 is half of D_2 line transition dipole moment, using data from Ref. [66]. The relation between Rabi frequency and light intensity is $I/I_{sat} = 2\Omega^2/\Gamma^2$, where Γ is the rate of total spontaneous decays, Ω is

the Rabi frequency for the cycling transition corresponding to μ_0 , and the saturation intensity I_{sat} is $2.54\text{mW}/\text{cm}^2$ for D_2 line transition. To determine the branching ratio β of γ_{13} , the rate of $|3\rangle \rightarrow |1\rangle$ decay and the total decay rate Γ , all (π , σ^+ and σ^-) decays must be included, giving $\beta = 0.6$ by using sum rules on hyperfine manifold. Also, $\gamma_{13} + \gamma_{23} = \Gamma$, where γ_{23} is the rate of $|3\rangle \rightarrow |2\rangle$ decay.

6.1.2 Optical Master Equation and Rate Equation

When laser light couples the excited and ground states, the master equation in Lindblad form for a Λ system is given by [34, 54]

$$\begin{aligned} \frac{d\rho}{dt} = & -\frac{i}{\hbar}[H_{\text{atom}} + H_{\text{int}}(t), \rho] + \gamma_{13}(\hat{b}\rho\hat{b}^\dagger - \frac{1}{2}(\hat{b}^\dagger\hat{b}\rho \\ & + \rho\hat{b}^\dagger\hat{b})) + \gamma_{23}(\hat{c}\rho\hat{c}^\dagger - \frac{1}{2}(\hat{c}^\dagger\hat{c}\rho + \rho\hat{c}^\dagger\hat{c})), \end{aligned} \quad (6.1)$$

where ρ is the density matrix of the atomic system. $H_{\text{atom}} = \sum_{i=1}^3 \hbar\omega_i |i\rangle \langle i|$, the atomic Hamiltonian. $H_{\text{int}}(t) = \hbar\Omega_{13}\cos\omega t(\hat{b} + \hat{b}^\dagger) + \hbar\Omega_{23}\cos\omega t(\hat{c} + \hat{c}^\dagger)$ is the interaction Hamiltonian. $\hat{b} = |1\rangle \langle 3|$ and $\hat{c} = |2\rangle \langle 3|$ are lowering operators and ω is the angular frequency of the light field.

With the rotating wave approximation in the interaction picture of the laser, Eq. 6.1 is simplified as

$$\begin{aligned} H = & \hbar(\Delta_{13} |1\rangle \langle 1| + \Delta_{23} |2\rangle \langle 2| \\ & + \frac{\Omega_{13}}{2}(\hat{b} + \hat{b}^\dagger) + \frac{\Omega_{23}}{2}(\hat{c} + \hat{c}^\dagger)), \end{aligned} \quad (6.2)$$

where $\Delta_{13} = \delta + \Delta$ and $\Delta_{23} = \delta - \Delta$ are frequency detunings between laser and atomic transitions with Δ as half the frequency splitting between states $|1\rangle$ and $|2\rangle$.

In a hot atomic vapor, an incoherent process induces a rapid relaxation of non-diagonal terms so that they remain equilibrium all the time with the diagonal terms. Thus the adiabatic elimination approximation is applied to set the time derivatives

of all non-diagonal terms to zero. With this approximation, the rate equation of the atom population is given by:

$$\frac{d\mathbf{P}}{dt} = M\mathbf{P}, \quad (6.3)$$

where $\mathbf{P} = \{\rho_{11}, \rho_{22}, \rho_{33}\}$, and M is the coefficient matrix depending on the light intensity. \mathbf{P} is a function of position in three-dimensions, and M is a function of position and laser detuning δ .

6.1.3 Velocity-Changing Collisions

Previous models of absolute absorption in atomic vapors usually ignore the effects of buffer gases. In the presence of buffer gas, the velocity changing collision (VCC) must be included in the atomic model, where VCC plays an important role to rethermalize the atomic velocity distribution between multiple levels. For example, atoms with axial velocity between $v_{res} - \delta v$ and $v_{res} + \delta v$ are optically pumped by monochromatic light, creating a velocity distribution “dip” around the resonant velocity v_{res} . However, VCC can partially reverse the procedure, by kicking out pumped atoms from the resonant region and recruit unpumped ones into the region. In this three-level system, the monochromatic light couples both transitions, but not with the same velocity group of atoms due to hyperfine splitting of ground state lithium. This would lead to accumulation of unpumpable atoms and the vapor would be optically near-transparent, as the only absorption contribution would be “reset” atoms colliding with cell wall. Thanks to the VCC collision, the optical pumping process can continue in the optical illuminated region of cell as VCC provides unpumped atoms, as pictured in Fig. 6.2.

Three kinds of collision are present in our experiment: Li-Li, Li-Ar, and Li-wall. Since the lithium vapor has a number density of 10^{16} m^{-3} at $340 \text{ }^\circ\text{C}$, and argon vapor of 10^{20} m^{-3} at the same temperature, we ignore Li-Li collision and focus on Li-Ar collision, which changes the velocity of lithium atom but rarely changes its spin state [41]. The lithium-cell wall collision will reset both spin state and velocity of lithium

atoms to thermal equilibrium, which serves as a boundary condition for the atomic state evolution equation. In order to add VCC to Eq. 6.3, a system without optical transition and decay at all is considered. All relaxation to equilibrium is solely caused by VCC. The addition of this relaxation term in Eq. 6.3 will yield a VCC effect in atomic evolution such that $\frac{d\mathbf{P}}{dt} = -\gamma_{vc}(\mathbf{P} - \mathbf{P}_0)$, where γ_{vc} is VCC rate, and \mathbf{P}_0 is the equilibrium number density $\{0.5, 0.5, 0\}$. The solution of such a system is an exponential relaxation towards equilibrium, with the inverse of VCC rate as time constant.

The VCC rate is estimated as following: suppose each collision between Li-Ar resets lithium velocity to thermal distribution, and total collision rate is proportional to Li-Ar cross-section, argon number density, and relative velocity between Li and Ar atoms.

$$\gamma_{vc} = \sigma_{\text{Li-Ar}} n_{\text{Ar}} \sqrt{\frac{8kT}{\pi\mu}} \quad (6.4)$$

Where n_{Ar} is the number density of argon, μ is reduced mass, and $\sigma_{\text{Li-Ar}}$ is the collision cross-section of lithium and argon. Note that the collision rate is for each lithium atom.

6.2 Transverse Gas Dynamics and Numerical Solution of Atom-Light Coupled Equations

To describe the absolute absorption of ${}^6\text{Li}$ by coupling the atomic state evolution, the atomic motion and the spatial evolution of the light field together, the gas dynamic model proposed in Ref. [54] is adopted. First the atomic state evolution is transformed from the atomic frame to the laboratory frame, so Eq. 6.3 becomes $d/dt \rightarrow \partial/\partial t + \vec{v} \cdot \nabla$. Then two approximations in the laboratory frame are made: first, set $\partial/\partial t = 0$ for steady state solutions; second, ignore the axial variation of the atomic states by using $\vec{v} \cdot \nabla = v_\tau \partial/\partial \tau + v_z \partial/\partial z \approx v_\tau \partial/\partial \tau$ (here a rectilinear coordinate system is used in the velocity space where \hat{z} is along the axial direction of the beam and $\hat{\tau}$ is along the transverse direction of atomic motion. The atomic velocity component perpendicular

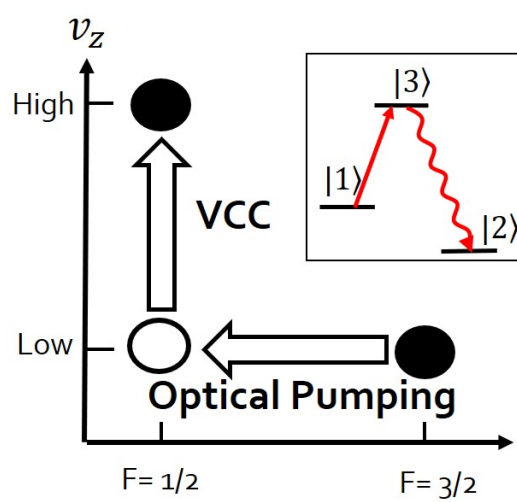


Figure 6.2. Description of the velocity-changing collisions effect on the light absorption. For the inset, the resonant transition is $2^2S_{1/2} |F = 3/2\rangle \leftrightarrow 2^2P_{3/2}$

to both \hat{z} and $\hat{\tau}$ is zero). The reason is that the typical beam diameter, 5 mm, is much shorter than the absorption length in the vapor cell of about 10 cm. Since the absorption length determines the axial variation, and the beam diameter determines the transverse one, the axial variation of the atomic state is much smaller compared to the transverse one. Now Eq. 6.3 becomes

$$v_\tau \frac{\partial \mathbf{P}}{\partial \tau} = M \mathbf{P}, \quad (6.5)$$

where \mathbf{P} is a function of position in three-dimensions and velocity (v_τ and v_z). By changing the frame, atomic states and atomic velocities are now connected.

The spatial evolution of light field is determined by the atomic population using the M matrix,

$$\delta N = [(M_{13} - 2\beta\Gamma + M_{23} + \Gamma)\bar{P}_3 - (M_{31}\bar{P}_1 + M_{32}\bar{P}_2)]\rho_0\delta V\delta t \quad (6.6)$$

where δN is the change of photon number N over a small volume of δV in time δt , ρ_0 is lithium number spatial density, and \bar{P}_i is the i -state population in that small volume, averaged by the 3D Maxwell-Boltzmann (M-B) distribution of the atom velocity in thermal equilibrium. Because the laser beam and atomic vapor are both cylindrically symmetric, the rectilinear velocities obey M-B distribution in cylindrical coordinates, such that

$$\bar{P} = \int_0^{2\pi} \frac{d\theta}{2\pi} \int_0^\infty dv_\tau F_\tau(v_\tau) \int_{-\infty}^\infty dv_z F_z(v_z) P(\vec{v}) \quad (6.7)$$

Here $F_\tau(v_\tau) = 2v_\tau e^{-(v_\tau/v_0)^2}/v_0^2$ and $F_z(v_z) = e^{-(v_z/v_0)^2}/\sqrt{\pi}v_0$ are distributions of the transverse and longitudinal velocities respectively, and v_0 is the most probable speed in M-B distribution.

From Eq.6.6, light intensity is given by $I = N\hbar\omega/(\delta A\delta t)$, where δA is the cross section perpendicular to the \hat{z} . Using the relation between Rabi frequency and light intensity, the spatial Rabi frequency distribution is coupled to the atomic density matrix by

$$\frac{\partial \Omega^2(\vec{x})}{\partial z} = \kappa\Gamma[(M_{13} - 2\beta\Gamma + M_{23} + \Gamma)\bar{P}_3 - (M_{31}\bar{P}_1 + M_{32}\bar{P}_2)], \quad (6.8)$$

where $\kappa = \hbar\omega\rho_0\Gamma/(2I_{sat})$.

Eq.6.7 can be simplified by taking the $F_z(v_z)$ out of the integral because the Doppler width $\Delta_{dop} = \omega v_0/c$ is much larger than the natural linewidth Γ . By substituting $v_z = \delta c/\omega$ in the Eq. 6.7 and assuming that only for $v_z \gg v_0$, $F_z(v_z)$ is a constant $1/\sqrt{\pi}v_0$, and zero for other v_z . i.e. it is assumed the laser frequency is in the central region of Doppler broadened absorption peak. The light intensity evolution equation becomes

$$\begin{aligned} \Omega^2(r, z) = \Omega^2(r, 0) \text{Exp}\{ & -K \int_0^z dz_0 \int_0^{2\pi} \frac{d\theta}{2\pi} \int_0^\infty F_\tau(v_\tau) \\ & dv_\tau \int_{-\infty}^\infty \frac{d\delta}{\Omega^2(r, z)} [(M_{13} - 2\beta\Gamma + M_{23} + \Gamma)P_3(r, z_0, v_\tau, \delta) - \\ & M_{31}P_1(r, z_0, v_\tau, \delta) - M_{32}P_2(r, z_0, v_\tau, \delta)]\}, \end{aligned} \quad (6.9)$$

where

$$K = (\hbar\omega\rho_0\Gamma^2\lambda)/(4\pi^{3/2}I_{sat}v_0) \quad (6.10)$$

is the inverse absorption length characterizing the optical density of atomic vapor. Eq. 6.5 and Eq. 6.9 give us a complete description of atom-light interaction including the effects from spatial atomic motion. These nonlinear equations are coupled in 6-dimensional phase space with no analytic solutions available, so we implement a self-consistent numerical approach to solve them.

In order to facilitate numerical solving process, we nondimensionalize radial, axial and time units. Because the radial and axial evolution are completely decoupled, we are allowed to use different scales for radial and axial lengths. The table of conversion is given in Table 6.1. After this transformation, the form of Eq. 6.5 does not change, and Eq. 6.9 changes by absorbing the K coefficient into z .

From now on, all physical quantities in the numerical solving process are assumed nondimensional.

The iteration sequence is as follows (The numerical code used is listed in Appendix D and each step is labeled with a line number):

Table 6.1.
Conversion from dimensional variables to nondimensional variables.

Variable	Nondimensional Variable	Description
r	r/r_0	Radial Length
z	Kz	Axial Length
t	$t\Gamma$	Time
v_τ	$v_\tau/(r_0\Gamma)$	Transverse Atomic Velocity
Ω	Ω/Γ	Rabi Frequency
Δ	δ/Γ	Half of Hyperfine Splitting of $2S_{1/2}$
δ	δ/Γ	Detuning From Δ
v_0	$v_0/(r_0\Gamma)$	Most Probable Velocity

1. Use a test distribution for light intensity (e.g. $\Omega_0^2(r, z) = \Omega^2(r, 0)\text{Exp}(-z/z_0)$, where z_0 is an educated guess based on input intensity).
2. Solve for $\mathbf{P}(v_\tau, \delta, \vec{x})$ using the $\Omega^2(r, z)$ in step 1 with Eq. 6.5.
3. Calculate a new set of $\Omega_1^2(r, z)$ with Eq. 6.9, using $\Omega^2(r, z)$ in step 1 and $\mathbf{P}(v_\tau, \delta, \vec{x})$ in step 2.
4. Use the new set of $\Omega_1^2(r, z)$ to replace the one in step 1.
5. Go back to step 2.

By recursive iteration we reach a convergent solution with 1% variation in transmission ratio in 2 iterations.

The transmission ratio T from light intensity distributions $\Omega^2(r, z)$ is obtained from the above simulation with: $T(z) = \int_0^{r_1} r\Omega^2(r, z)dr / \int_0^{r_1} r\Omega^2(r, 0)dr$, where r_1 is the iris radius that limits the beam size and z is the effective vapor length.

6.3 Experimental Setup

The lithium vapor cell is a customized stainless steel tee vacuum fitting of 20 inches with a 2.75 inch del-seal fused silica viewport (Thorlabs VPCH42-B) at each end. The branch is connected to an angle valve (Ideal Vacuum P103787). The clear aperture of the input viewport is larger than 1.3 inch which suitable for the input light beam up to one inch diameter. About 3 g of ^6Li (enriched to $> 97.5\%$) is cut into 1 cm^3 pieces and placed in the center of the tee. A single core heating element tape from Omega is folded into two layers to reduce the magnetic field generated and uniformly wrapped 10 cm long around the center of the tee. In order to reduce the effect of the earth magnetic field, we set the current of the heating tape to the range of 1.14-1.21 A, and use the residue magnetic field of the heating tape to cancel out the earth magnetic field. The measured residual magnetic field is less than 100 mG by a Hall probe. We pack the heating area with 3 cm thick fiberglass and two layers

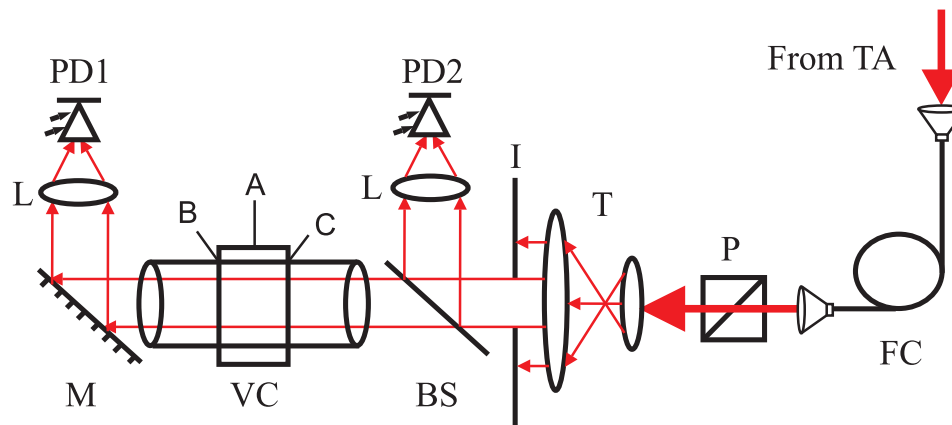


Figure 6.3. Experimental setup for absorption measurement. TA: taper-amplified diode laser; FC: fiber couplers and optical fiber in between; P: linear polarizer; T: telescope; I: adjustable iris; BS: beam splitter; VC: vapor cell; L: lens; PD1 and PD2: signal and reference photodiodes. The laser light is sent through a fiber coupling scheme to improve the Gaussian beam profile quality. Then the beam is enlarged and split between PD1 and PD2 paths. In the vapor cell, A, B and C are places we put thermocouples on, and the temperatures are 340 °C, 320 °C and 320 °C respectively. AB and AC are both 5 cm long.

of aluminum foil to maintain the central temperature at 340 °C, which is measured by 3 thermocouples at the center and the ends of the heating area. The accuracy of the thermocouple is ± 2 °C. We pre-baked the tubing to 150 °C for 12 hours to remove residual impurities after we load the ^6Li samples. After the cell cooled down, 20 mTorr argon ($> 99\%$ purity) was filled into the cell as the buffer gas.

Our absorption measurement is shown in Fig. 6.3. In this setup, an adjustable iris is used to control the laser beam profile, and PD1 and PD2 are used for the balanced measurement to cancel out the laser noise.

6.4 Results

6.4.1 Experimental Method and Comparison with Simulation

In our measurements, the input beam to the vapor cell is a Gaussian beam of waist size of 2.5 mm ($1/e$ intensity). To study the absorption dependence on the beam intensity, the beam central intensity is tuned from $10I_{sat}$ to $0.1I_{sat}$ with the maximum power at $10I_{sat}$ is 20 mW. In our gas dynamic model, the absorption also depends on the beam size and profile. To study this effect, we filter the Gaussian beam with the iris, and obtain different beam profiles as shown in Fig. 6.4.

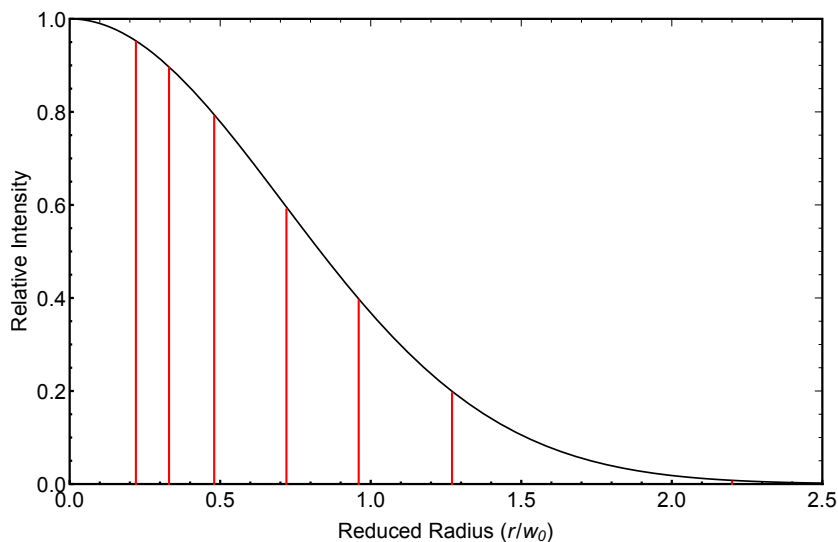


Figure 6.4. Gaussian beam shape with different beam profiles. The black line is the full input beam intensity distribution in the radial direction. The radius unit is the e^{-1} radius (2.5 mm) of the Gaussian beam and the intensity unit is normalized to the central intensity at $r = 0$. The radii of profiles corresponding to the transmitted power of 100%, 80%, 60%, 40%, 20%, 10%, and 5% of the full beam power are indicated by the red lines. The iris filters out optical power outside the red lines to obtain the desired profiles.

For an input beam with certain central intensity and beam profile, we scan laser frequency in 10 GHz range around D_2 transition of ${}^6\text{Li}$, and record the full Doppler absorption spectrum. With a lithium cell of temperature around 340 °C, the Doppler

broadened width is about 3 GHz. The transmission is given by $V_s/(\beta V_r)$, where V_s is the the photodiode PD1 signal of the transmission beam, V_r is the photodiode PD2 signal of the reference beam, and β is a signal ratio between the signal path and the reference one when the laser frequency is far-off-resonance with the atomic transitions, accounting for the beam splitting ratio, power loss on the viewports of the call, and the gain difference between of two photodetectors.

The measured transmission is a Doppler broadening profile, and the frequency dependence of V_s/V_r can be treated as an inverted Voigt profile with a baseline of $V_s/V_r = \beta$ [122]. Because of the D_1 transition is 10.6 GHz below the D_2 , the base line has a small slope. The fitting formula is given by

$$V_s(f)/V_r(f) = \beta[(1 + kf) - AV(f - f_0; w_G, w_L)] \quad (6.11)$$

$$V(f; w_G, w_L) = \frac{w_L \sqrt{\ln 2}}{\pi w_G} \int_{-\infty}^{\infty} df' \frac{\text{Exp}(-f'^2)}{\ln 2 \frac{w_L^2}{w_G^2} + (\frac{2\sqrt{\ln 2}}{w_G} f - f')^2} \quad (6.12)$$

where k is the slope of baseline, which is less than 10^{-3} per GHz in all cases. A is amplitude of Voigt function $V(f; w_G, w_L)$, and $V(f - f_0; w_G, w_L)$ is Voigt function, which is centered in f_0 with the Gaussian width w_G and the Lorentzian width w_L . Using that fitting procedure, we can extract the peak transmission and Doppler width w_G by fixing Lorentzian width w_L as 5.87 MHz. The peak transmission ratio then is given by

$$T = 1 - A \frac{\text{Exp}(\ln 2 \frac{w_L^2}{w_G^2})}{\text{Erfc}(\frac{w_L \sqrt{\ln 2}}{w_G})} \quad (6.13)$$

Fig. 6.5 shows a typical example of the fitting. The relative fitting residual is less than 2% in all the fitting range.

6.4.2 Peak Transmission as Function of Beam Intensity and Size

The comparison between simulation and experimental results verifies the validity of our model. The decrease of transmission accompanied by decrease in beam size is qualitatively in agreement with the effusive dynamics of atomic vapor: smaller beam

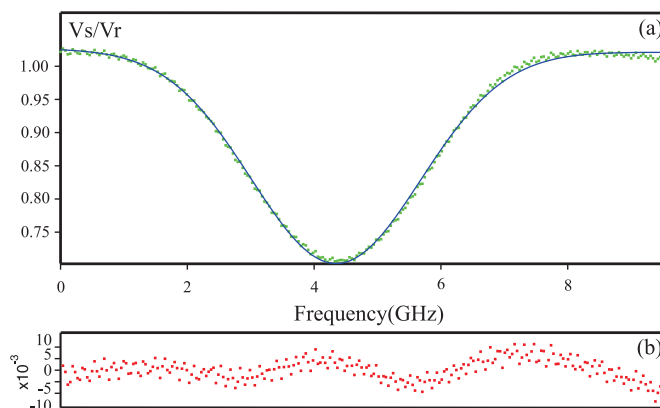


Figure 6.5. Experimental results for 340 °C, $I=10I_{sat}$, 40% power transmitted through iris. (a) Green dots: measurement data, blue curve: fitting by Eq. 6.12, and (b) red dots: residual of fitting.

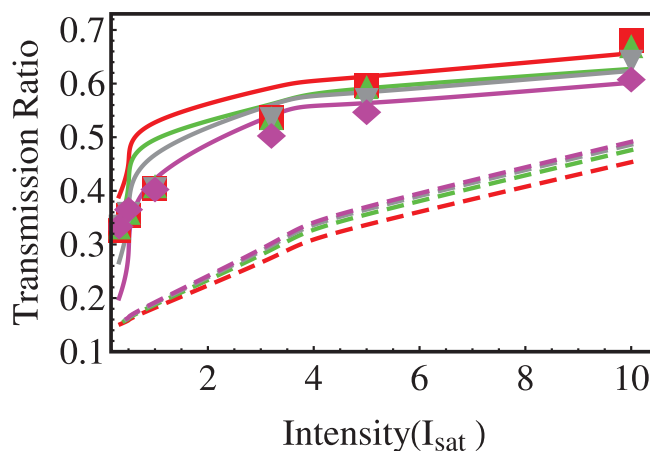


Figure 6.6. Transmission ratio vs. central beam intensity for different beam sizes. Beam size is expressed as the percentage of full beam power transmitted through iris. Markers are experimental results, where red squares are 40% power transmitted, green up-triangles are 20%, gray down-triangles are 10%, and magenta diamonds are 5%. The four solid curves in the upper part of the figure are simulations based on our model, and the four dashed curves in the lower part are calculated based on two-level model in Sec. VIII of Ref. [54].

size brings higher proportion of fresh, thermal atoms into the illuminated region, thus increasing absorption. The other effect of transmission decreasing when intensity decreases is the effect of absorption saturation. The quantitative agreement between

simulation and experiment shows that our estimate of effective vapor length is also accurate.

Here the results of 2-level model with no transverse dynamics from Ref. [54] is also included. In the 2-level model, the transmission ratio is solely dependent on the light intensity, which means the smaller beam would yield higher transmission due to the increase of average intensity. Such trends are not observed in our experiments, prompting that the transverse dynamics are not negligible.

The root mean square deviation of the simulation results from the experiment with all the power cuts, show that for low transmitted power, the results are not as good as for higher transmitted power as seen in Fig. 6.7. The simulation predicts the velocity changing collision rate to be about an order of magnitude higher than the D_2 decay rate. Comparisons of the simulation and experimental curves are shown in Figs. 6.8-6.11. Here again we can see the results don't match as well for the weak beam. RMS deviation shows the best results around γ_{vc} of around 1 and 10 based the full transmission curve with all I/I_{sat} values. Observed in the simulation results is that for larger transmitted power, the simulation curve comes closer to the experimental result. Also observed is a saturation effect which for large γ_{vc} values, where it dominates the other effects in the gas dynamics population equation.

For the power dependence of the individual intensity curves shown in Figs. 6.12-6.15. The simulation without buffer gas collisions underestimates the transmission for the weak probe and overestimates for the strong probe. As with the intensity data, the simulation disagrees most with the low power data.

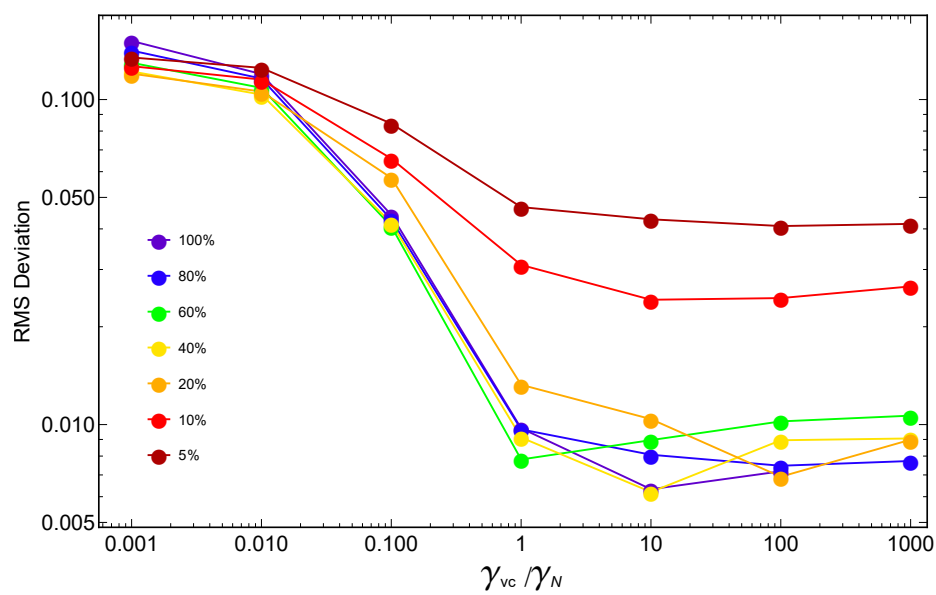
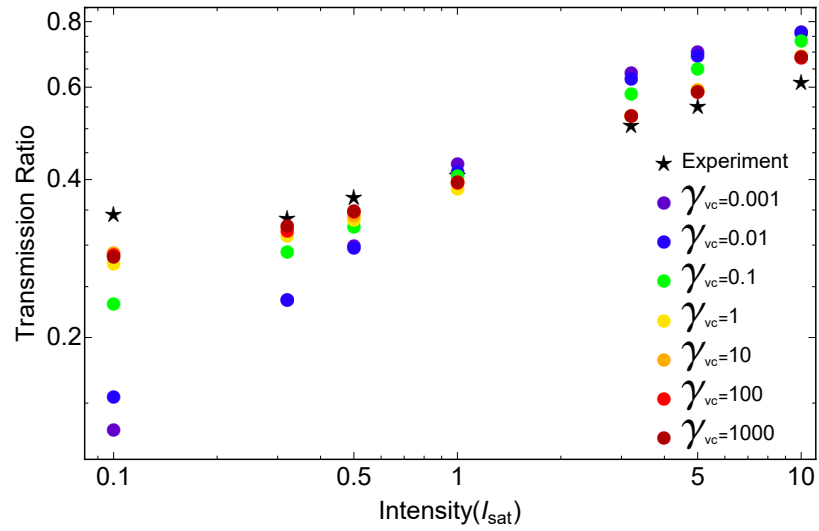
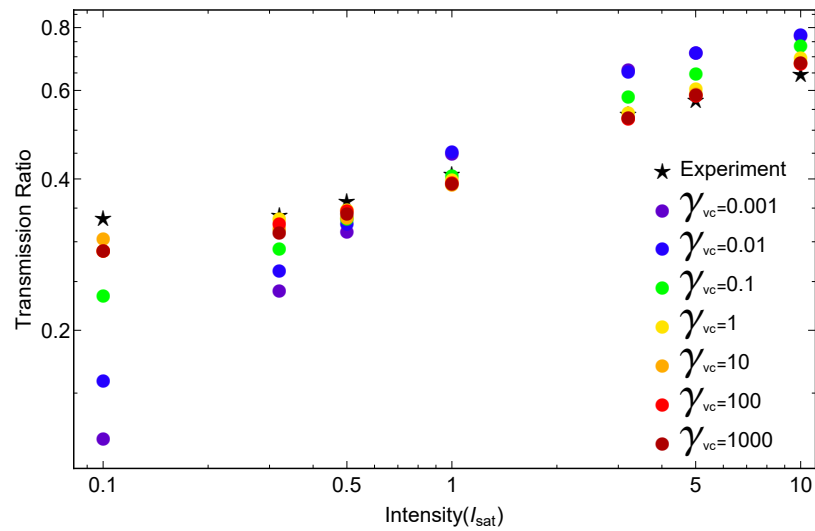


Figure 6.7. RMS deviation for simulated velocity-changing collision decay rate where γ_N is the decay rate of the D_2 transition. Each curve is calculated for all seven I/I_{sat} values for each power percentage.

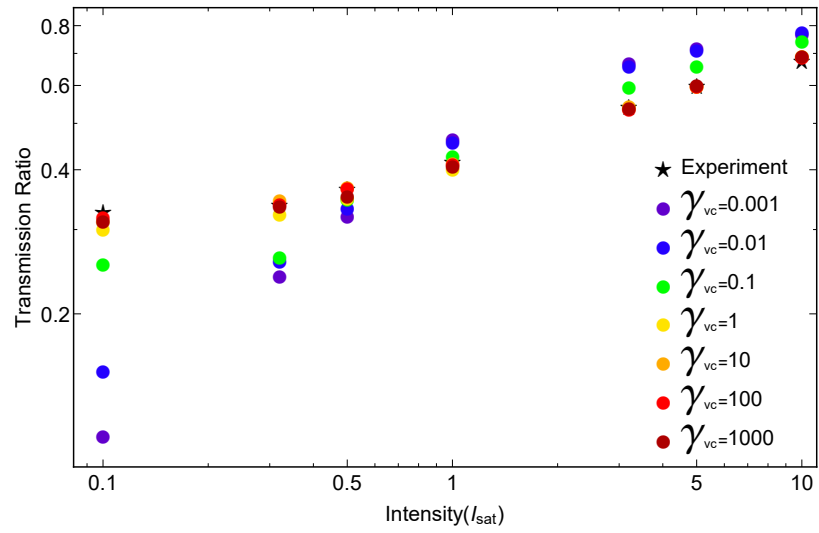


(a)

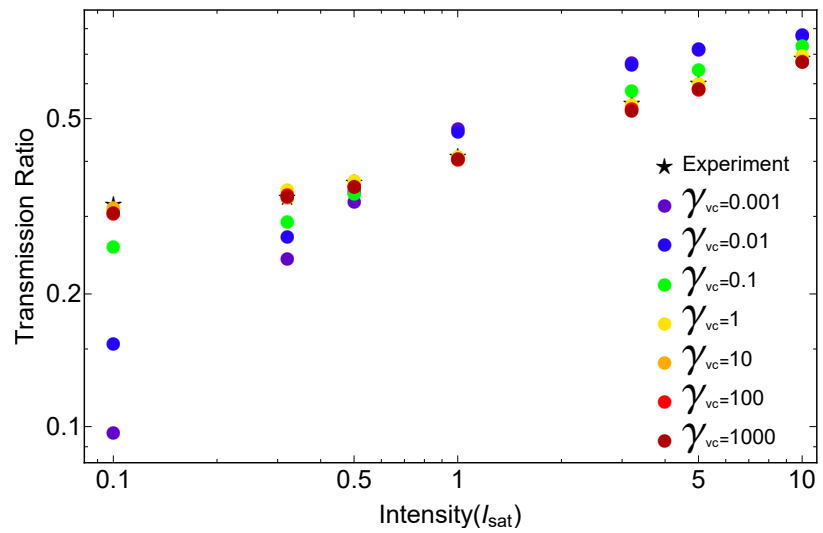


(b)

Figure 6.8. Simulation and experimental results at fixed beam power for (a) 5% transmitted power and (b) 10% transmitted power.

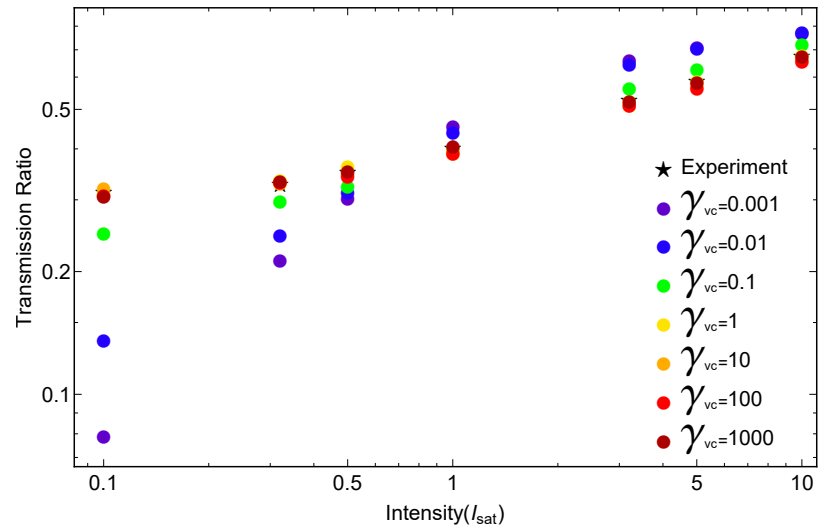


(a)

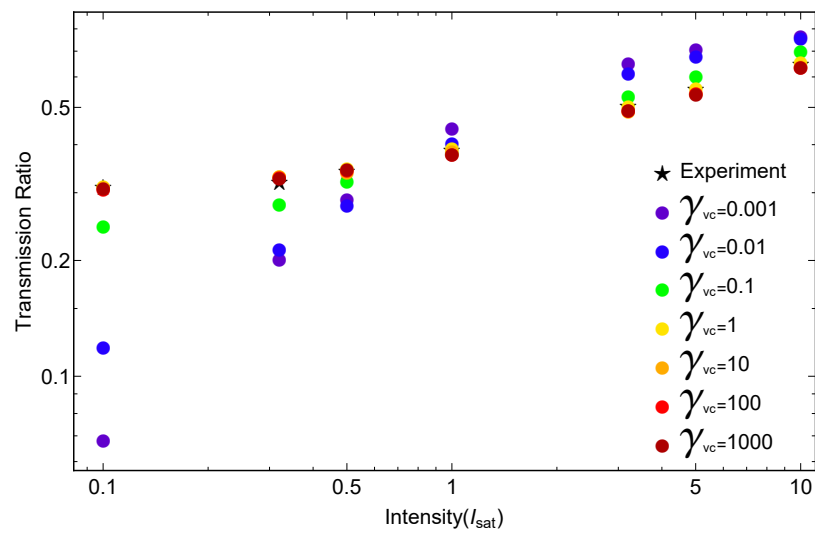


(b)

Figure 6.9. Simulation and experimental results at fixed beam power for (a) 20% transmitted power and (b) 40% transmitted power.



(a)



(b)

Figure 6.10. Simulation and experimental results at fixed beam power for (a) 60% transmitted power and (b) 80% transmitted power

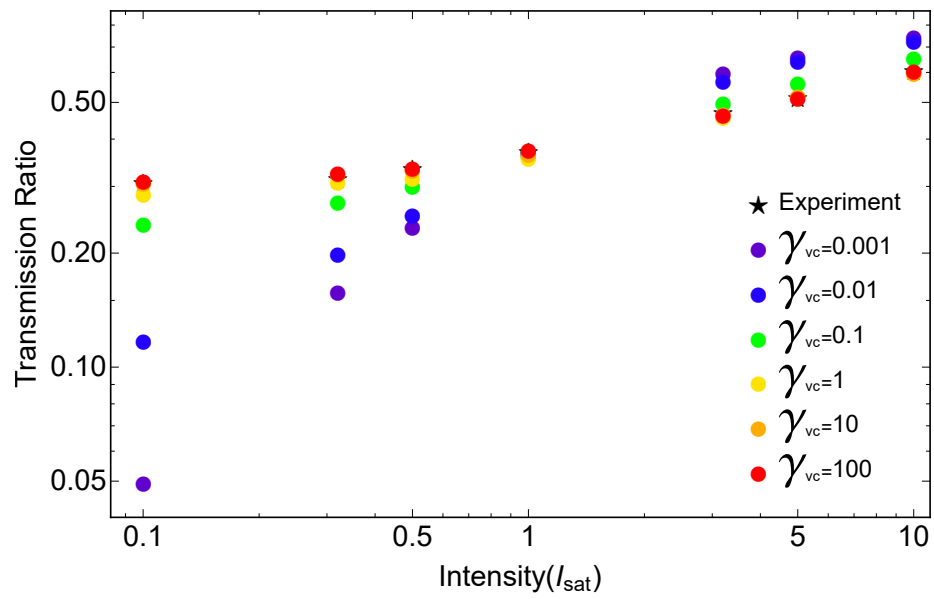
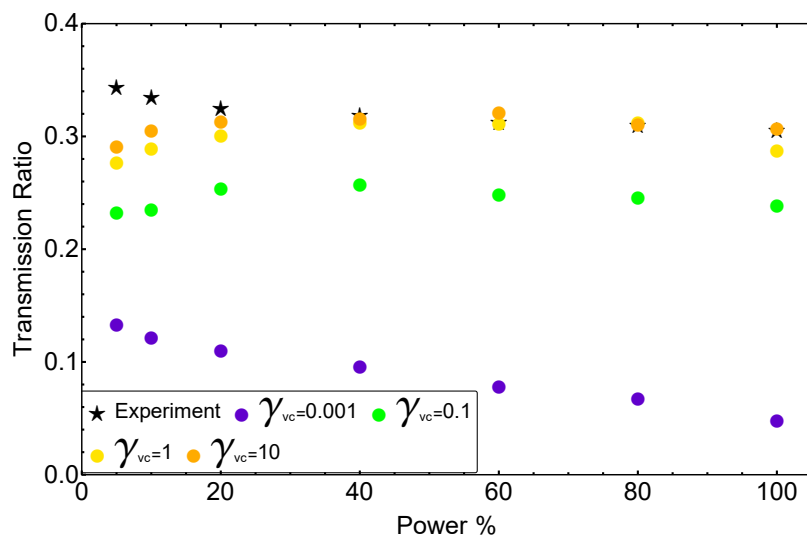
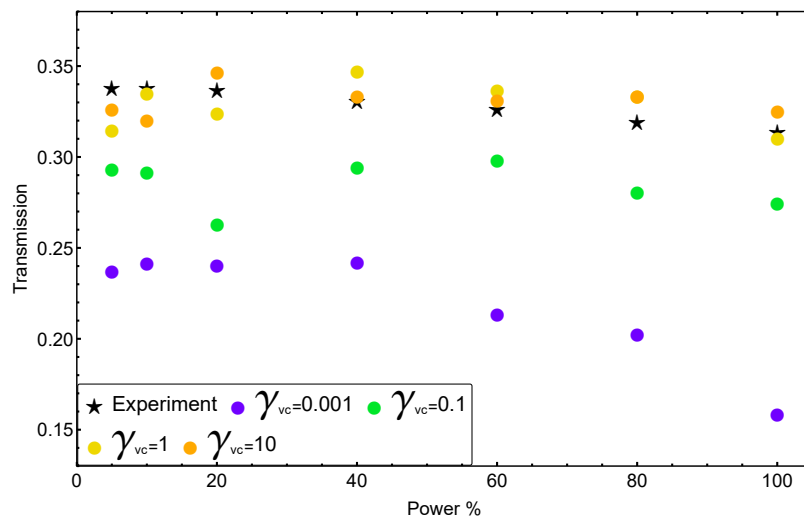


Figure 6.11. Simulation and experimental results at 100% transmitted power.

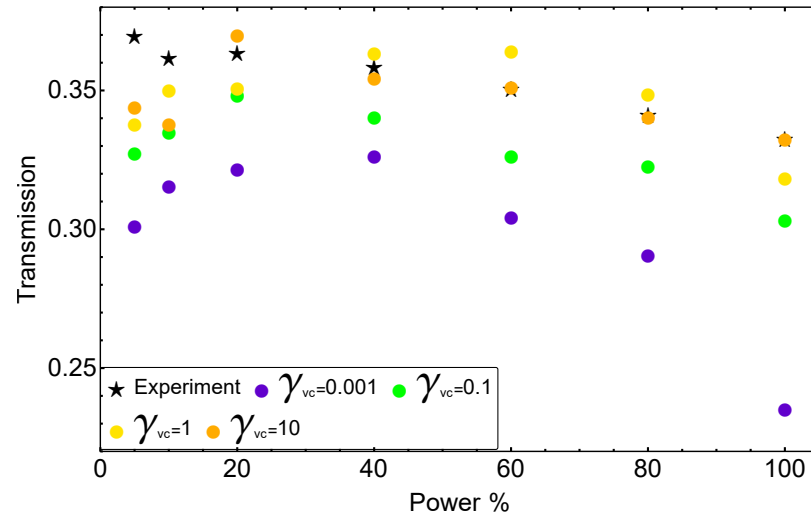


(a)

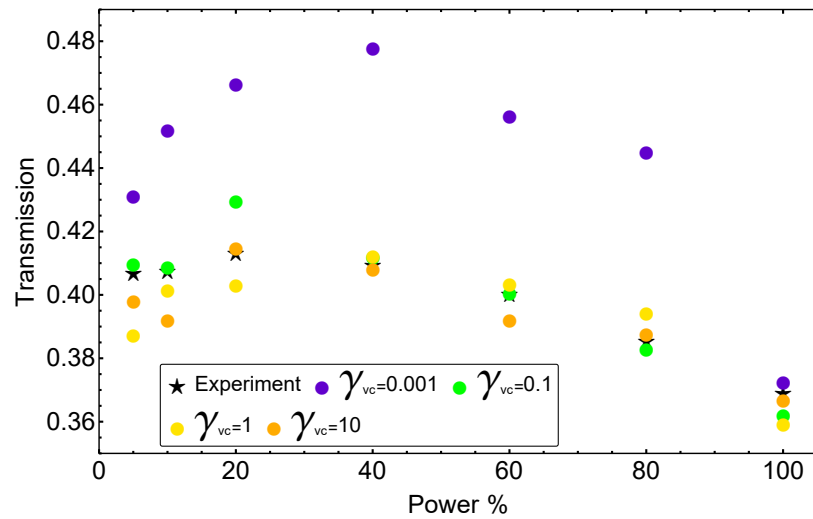


(b)

Figure 6.12. Simulation and experimental results at fixed beam power for (a) $0.1I/I_{sat}$ transmitted power and (b) $0.32I/I_{sat}$ transmitted power.

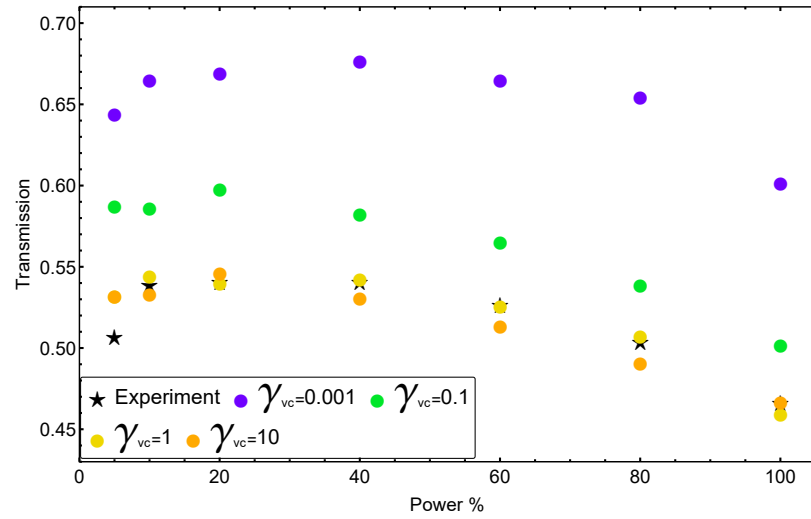


(a)

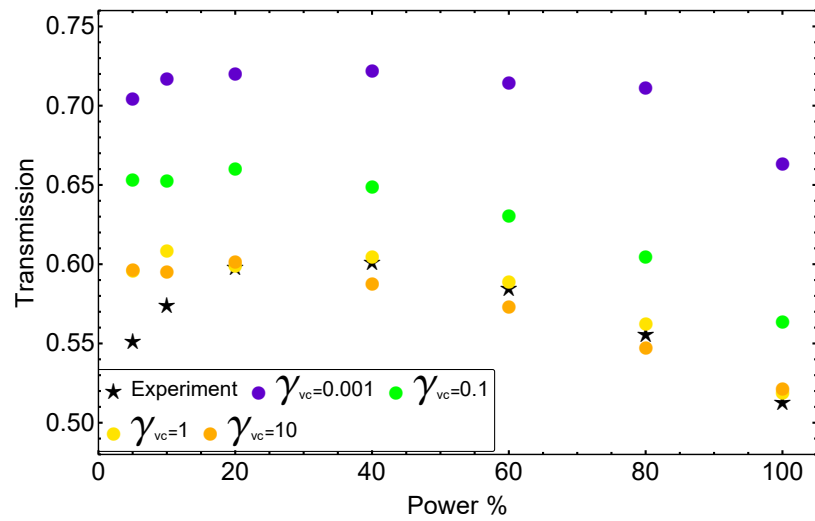


(b)

Figure 6.13. Simulation and experimental results at fixed beam power for (a) $0.5I/I_{sat}$ transmitted power and (b) $1I/I_{sat}$ transmitted power.



(a)



(b)

Figure 6.14. Simulation and experimental results for (a) $3.2I/I_{sat}$ and (b) $5I/I_{sat}$.

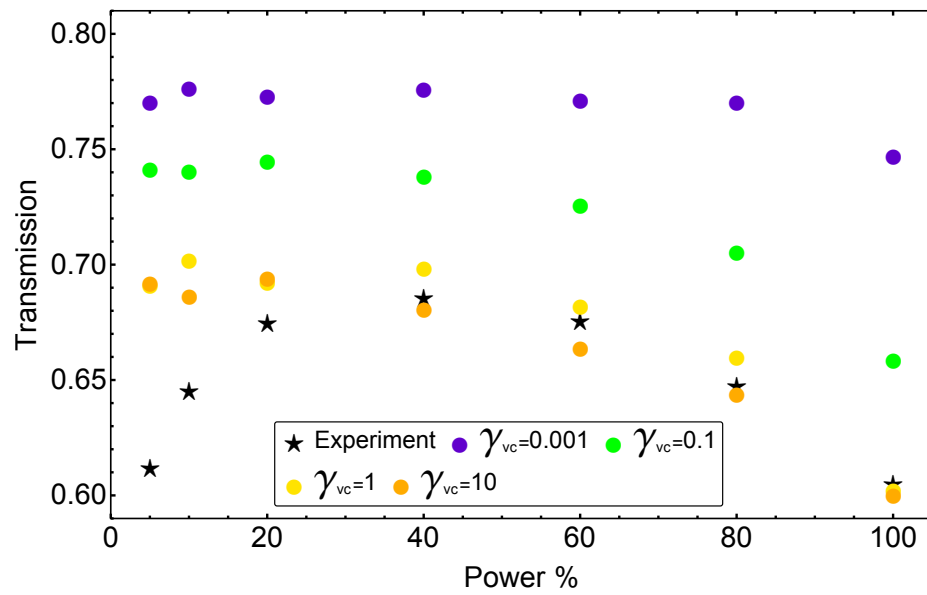


Figure 6.15. Simulation and experimental results at $10I/I_{sat}$.

7. SUMMARY AND OUTLOOK

My work in this project began with learning CAD and UHV techniques to design and build the vacuum side of the apparatus starting with an empty lab. Along with my labmates working on various projects with optics, electronics and computer control, in two years we realized our first degenerate Fermi gas in 2014. In those two years much of the time was spent troubleshooting systems and redesigning things until they worked. All of this work has paid off with the experiments that were conducted with the completed apparatus. Our vacuum system has not had any problems throughout our research at IUPUI, or during moving to SYSU, when the ion pumps were turned off and only the NEG was pumping. We were able to achieve a degenerate Fermi gas with a minimum $T/T_F \approx 0.2$ with 1.5×10^5 atoms/spin.

During the time between 2014 and 2018, I worked on multiple projects in our group: parametric cooling of a degenerate Fermi gas, three-body recombination near a narrow Feshbach resonance, parity-time symmetry breaking transitions in a cold atom system, itinerant ferromagnetism and absolute absorption of a ^6Li vapor. Listed below are projects where I made major contributions.

The parametric cooling of a degenerate Fermi gas was the first experiment with published results in our lab. This was exciting to know that our apparatus is able to produce new results. Showing that a degenerate Fermi gas can be cooled by parametric excitation in an ODT, has lead us to believe that our method would be more efficient using a more anharmonic trap like a box-trap [123]. The modeling of results using classical methods gives a good fit, even though we used Fermi statistics to determine atomic cloud properties.

The proposed experiment for observation of itinerant ferromagnetism in a two-dimensional Fermi gas based on the Stoner model and applied to a repulsive Fermi gas, where the formation of repulsive polarons leads to separation of spins into polarized

domains is yet to be performed. Speculation exists on whether the polaron decay into dimers limits the observation time of the domains, an effect that is not considered in the Stoner model. This project has taken more time to realize than first planned due to funding problems, but future students in our laboratory will continue this research and conduct the experiments at Sun-Yat Sen University.

Observation of optical absorption by ${}^6\text{Li}$ in Ar buffer gas based on the probe beam intensity and radius including the role of velocity-changing collisions in the transmission spectrum was successful. The application of an effective three-level model for simulating the experimental results yielded favorable results as the simulation was able to determine a velocity-changing collision rate that fit well with experimental results.

After moving the lab to Sun-Yat Sen University and beginning the assembly work, improvements on the apparatus for future experiments include:

Magnets upgrade with less power consumption due to new coil configuration and cooling system allowing the coils to be placed inside the recessed windows. The coils (pictured in Fig. 7.1) are mounted on a water-cooled copper plate and have electrically insulating, thermally conductive epoxy between the windings for heat dissipation. The current in the coils will be generated with high current batteries, with MOSFETs (design and implementation shown in Fig. 7.2) used for current control. This setup will allow for a bias field of 1008 G to be produced with 100 A in each coil. With these improvements, we expect to reach a magnetic field stability of 1 mG, which is necessary for studies in the ${}^6\text{Li}$ narrow-Feshbach resonance with 0.1 G width.

Other upgrades to the apparatus are also being made to conduct research in itinerant ferromagnetism. We have added a single-mode 1064 nm laser to create the optical lattice required for formation of the two-dimensional gas. The new magnets will also aid in this research as expected faster magnetic field sweeping time will allow faster changes in interaction strength. Finally, we will also implement a high-resolution imaging system that includes a diffraction limited objective to give us a calculate imaging resolution of $0.82 \mu\text{m}$.

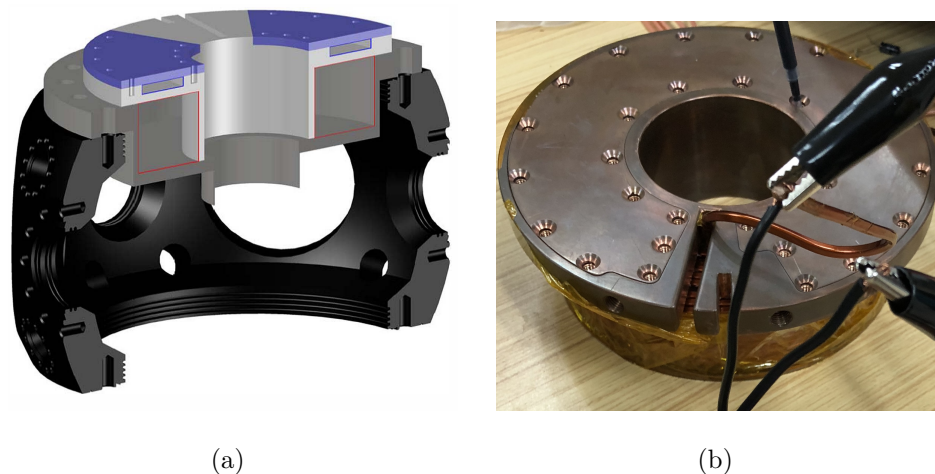
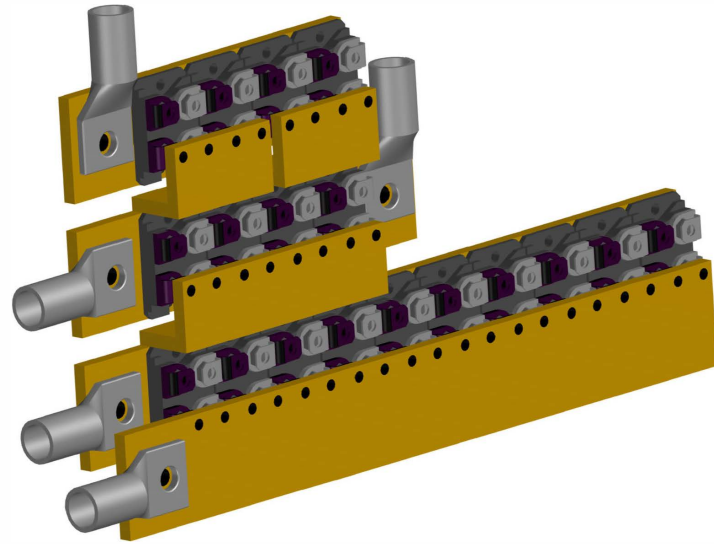


Figure 7.1. Magnet design and implementation. (a) Design for magnets to fit inside recessed window for closer proximity to trapped atoms with the red rectangles indicate the region of square wire windings. (b) Implementation of design on a water-cooled copper mount.

Addition of 323 nm laser for a narrow-line “blue” MOT with lower the Doppler limit of a “red” MOT by about seven times to improve cooling efficiency during experimental runs, therefore shortening evaporative cooling time. Our setup will be different from previous works in that our laser has 300 mW output, giving us enough power to operate a purely “blue” MOT, without the need of the 671 nm laser.



(a)



(b)

Figure 7.2. MOSFET mount design and implementation. (a) Mounting on copper plates for current distribution and cooling. (b) Implementation of design on a water-cooled aluminum plate.

REFERENCES

REFERENCES

- [1] National Research Council. *Atomic, Molecular, and Optical Physics*. The National Academies Press, Washington, DC, 1986.
- [2] David Kramer. Darpa looks beyond gps for positioning, navigating, and timing. *Physics Today*, 67(10):23–26, 2014.
- [3] V. Guillemin. *The Story of Quantum Mechanics*. Scribner, 1968.
- [4] T. H. MAIMAN. Stimulated optical radiation in ruby. *Nature*, 187:493 EP –, Aug 1960.
- [5] William D. Phillips and Harold Metcalf. Laser deceleration of an atomic beam. *Phys. Rev. Lett.*, 48:596–599, Mar 1982.
- [6] E. L. Raab, M. Prentiss, Alex Cable, Steven Chu, and D. E. Pritchard. Trapping of neutral sodium atoms with radiation pressure. *Phys. Rev. Lett.*, 59:2631–2634, Dec 1987.
- [7] M. H. Anderson, J. R. Ensher, M. R. Matthews, C. E. Wieman, and E. A. Cornell. Observation of bose-einstein condensation in a dilute atomic vapor. *Science*, 269(5221):198–201, 1995.
- [8] K. B. Davis, M. O. Mewes, M. R. Andrews, N. J. van Druten, D. S. Durfee, D. M. Kurn, and W. Ketterle. Bose-einstein condensation in a gas of sodium atoms. *Phys. Rev. Lett.*, 75:3969–3973, Nov 1995.
- [9] C. C. Bradley, C. A. Sackett, J. J. Tollett, and R. G. Hulet. Evidence of bose-einstein condensation in an atomic gas with attractive interactions. *Phys. Rev. Lett.*, 75:1687–1690, Aug 1995.
- [10] B. DeMarco and D. S. Jin. Onset of fermi degeneracy in a trapped atomic gas. *Science*, 285(5434):1703–1706, 1999.
- [11] P. A. Murthy, I. Boettcher, L. Bayha, M. Holzmann, D. Kedar, M. Neidig, M. G. Ries, A. N. Wenz, G. Zürn, and S. Jochim. Observation of the berezinskii-kosterlitz-thouless phase transition in an ultracold fermi gas. *Phys. Rev. Lett.*, 115:010401, Jun 2015.
- [12] J. E. Thomas, S. Ezekiel, C. C. Leiby, R. H. Picard, and C. R. Willis. Ultrahigh-resolution spectroscopy and frequency standards in the microwave and far-infrared regions using optical lasers. *Opt. Lett.*, 6(6):298–300, Jun 1981.
- [13] Arnold L. Bloom. Principles of operation of the rubidium vapormagnetometer. *Appl. Opt.*, 1(1):61–68, Jan 1962.

- [14] J. Kitching, S. Knappe, and L. Hollberg. Miniature vapor-cell atomic-frequency references. *Applied Physics Letters*, 81(3):553–555, 2002.
- [15] T. Bourdel, L. Khaykovich, J. Cubizolles, J. Zhang, F. Chevy, M. Teichmann, L. Tarruell, S. J. J. M. F. Kokkelmans, and C. Salomon. Experimental study of the bec-bcs crossover region in lithium 6. *Phys. Rev. Lett.*, 93:050401, Jul 2004.
- [16] Cheng Chin, Rudolf Grimm, Paul Julienne, and Eite Tiesinga. Feshbach resonances in ultracold gases. *Rev. Mod. Phys.*, 82:1225–1286, Apr 2010.
- [17] C. Cao, E. Elliott, J. Joseph, H. Wu, J. Petricka, T. Schäfer, and J. E. Thomas. Universal quantum viscosity in a unitary fermi gas. *Science*, 331(6013):58–61, 2011.
- [18] Pengjun Wang, Zeng-Qiang Yu, Zhengkun Fu, Jiao Miao, Lianghai Huang, Shijie Chai, Hui Zhai, and Jing Zhang. Spin-orbit coupled degenerate fermi gases. *Phys. Rev. Lett.*, 109:095301, Aug 2012.
- [19] Kirill Martiyanov, Vasiliy Makhhalov, and Andrey Turlapov. Observation of a two-dimensional fermi gas of atoms. *Phys. Rev. Lett.*, 105:030404, Jul 2010.
- [20] T. Rom, Th Best, D. van Oosten, U. Schneider, S. Fölling, B. Paredes, and I. Bloch. Free fermion antibunching in a degenerate atomic fermi gas released from an optical lattice. *Nature*, 444:733 EP –, Dec 2006.
- [21] Sara Rosi, Alessia Burchianti, Stefano Conclave, Devang S. Naik, Giacomo Roati, Chiara Fort, and Francesco Minardi. L-enhanced grey molasses on the d2 transition of rubidium-87 atoms. *Scientific Reports*, 8(1):1301, 2018.
- [22] David E. Pritchard. Cooling neutral atoms in a magnetic trap for precision spectroscopy. *Phys. Rev. Lett.*, 51:1336–1339, Oct 1983.
- [23] J. D. Miller, R. A. Cline, and D. J. Heinzen. Far-off-resonance optical trapping of atoms. *Phys. Rev. A*, 47:R4567–R4570, Jun 1993.
- [24] M. Kumakura, Y. Shirahata, Y. Takasu, Y. Takahashi, and T. Yabuzaki. Shaking-induced cooling of cold atoms in a magnetic trap. *Phys. Rev. A*, 68:021401, Aug 2003.
- [25] N. Poli, R. J. Brecha, G. Roati, and G. Modugno. Cooling atoms in an optical trap by selective parametric excitation. *Phys. Rev. A*, 65:021401, Jan 2002.
- [26] Shuyu Zhou, Zhen Xu, Shanyu Zhou, Liang Liu, and Yuzhu Wang. Parametric excitation of ^{87}Rb atoms in a quadrupole-ioffe-configuration trap. *Phys. Rev. A*, 75:053414, May 2007.
- [27] M G Blamire and J W A Robinson. The interface between superconductivity and magnetism: understanding and device prospects. *Journal of Physics: Condensed Matter*, 26(45):453201, 2014.
- [28] David Pekker, Mehrtash Babadi, Rajdeep Sensarma, Nikolaj Zinner, Lode Pollet, Martin W. Zwierlein, and Eugene Demler. Competition between pairing and ferromagnetic instabilities in ultracold fermi gases near feshbach resonances. *Phys. Rev. Lett.*, 106:050402, Feb 2011.

- [29] Gyu-Boong Jo, Ye-Ryoung Lee, Jae-Hoon Choi, Caleb A. Christensen, Tony H. Kim, Joseph H. Thywissen, David E. Pritchard, and Wolfgang Ketterle. Itinerant ferromagnetism in a fermi gas of ultracold atoms. *Science*, 325(5947):1521–1524, 2009.
- [30] Christian Sanner, Edward J. Su, Wujie Huang, Aviv Keshet, Jonathon Gillen, and Wolfgang Ketterle. Correlations and pair formation in a repulsively interacting fermi gas. *Physical Review Letters*, 108(24):240404, 2012.
- [31] Colin V. Parker, Li-Chung Ha, and Cheng Chin. Direct observation of effective ferromagnetic domains of cold atoms in a shaken optical lattice. *Nature Physics*, 9:769 EP –, Oct 2013.
- [32] G. Valtolina, F. Scazza, A. Amico, A. Burchianti, A. Recati, T. Enss, M. Inguscio, M. Zaccanti, and G. Roati. Exploring the ferromagnetic behaviour of a repulsive fermi gas through spin dynamics. *Nature Physics*, 13:704 EP –, Apr 2017. Article.
- [33] B. Welz, M. Sperling, and M. Resano. *Atomic Absorption Spectrometry*. Wiley, 2008.
- [34] Paul Siddons. Light propagation through atomic vapours. *Journal of Physics B: Atomic, Molecular and Optical Physics*, 47(9):093001, 2014.
- [35] T P Heavner, S R Jefferts, E A Donley, J H Shirley, and T E Parker. Nist-f1: recent improvements and accuracy evaluations. *Metrologia*, 42(5):411, 2005.
- [36] D. Budker, W. Gawlik, D. F. Kimball, S. M. Rochester, V. V. Yashchuk, and A. Weis. Resonant nonlinear magneto-optical effects in atoms. *Rev. Mod. Phys.*, 74:1153–1201, Nov 2002.
- [37] Thad G. Walker and William Happer. Spin-exchange optical pumping of noble-gas nuclei. *Rev. Mod. Phys.*, 69:629–642, Apr 1997.
- [38] M. V. Balabas, T. Karaulanov, M. P. Ledbetter, and D. Budker. Polarized alkali-metal vapor with minute-long transverse spin-relaxation time. *Phys. Rev. Lett.*, 105:070801, Aug 2010.
- [39] J.L. Hall, Long-Sheng Ma, M. Taubman, B. Tiemann, Feng-Lei Hong, O. Pfister, and J. Ye. Stabilization and frequency measurement of the i2-stabilized nd:yag laser. *Instrumentation and Measurement, IEEE Transactions on*, 48(2):583–586, Apr 1999.
- [40] J. Li, J. Liu, L. Melo, L. Luo, T. Lai, and Z. Wang. Sub-megahertz frequency stabilization of a diode laser by digital laser current modulation. *Appl. Opt.*, 54(13):3913–3917, May 2015.
- [41] Steven W. Morgan and William Happer. Optically pumped atoms with velocity- and spin-changing collisions at low gas pressures. *Phys. Rev. A*, 81:042703, Apr 2010.
- [42] W. W. Quivers. Production of highly polarized vapors using laser optical pumping with velocity-changing collisions. *Phys. Rev. A*, 34:3822–3838, Nov 1986.

- [43] Gar-Wing Truong, Eric F. May, Thomas M. Stace, and André N. Luiten. Quantitative atomic spectroscopy for primary thermometry. *Phys. Rev. A*, 83:033805, Mar 2011.
- [44] G. Casa, A. Castrillo, G. Galzerano, R. Wehr, A. Merlone, D. Di Serafino, P. Laporta, and L. Gianfrani. Primary gas thermometry by means of laser-absorption spectroscopy: Determination of the boltzmann constant. *Phys. Rev. Lett.*, 100:200801, May 2008.
- [45] C. Daussy, M. Guinet, A. Amy-Klein, K. Djerroud, Y. Hermier, S. Briaudeau, Ch. J. Bordé, and C. Chardonnet. Direct determination of the boltzmann constant by an optical method. *Phys. Rev. Lett.*, 98:250801, Jun 2007.
- [46] L-M Duan, MD Lukin, J Ignacio Cirac, and Peter Zoller. Long-distance quantum communication with atomic ensembles and linear optics. *Nature*, 414(6862):413–418, 2001.
- [47] C.J. Foot. *Atomic Physics*. Oxford Master Series in Physics. OUP Oxford, 2004.
- [48] I. E. Olivares, A. E. Duarte, T. Lokajczyk, A. Dinklage, and F. J. Duarte. Doppler-free spectroscopy and collisional studies with tunable diode lasers of lithium isotopes in a heat-pipe oven. *Journal of the Optical Society of America B*, 15(7):1932, 1998.
- [49] E. Vliegen, S. Kadlecsek, L.W. Anderson, T.G. Walker, C.J. Erickson, and William Happer. Faraday rotation density measurements of optically thick alkali metal vapors. *Nuclear Instruments and Methods in Physics Research Section A: Accelerators, Spectrometers, Detectors and Associated Equipment*, 460(2–3):444 – 450, 2001.
- [50] B. H. McGuyer, R. Marsland, B. A. Olsen, and W. Happer. Cusp kernels for velocity-changing collisions. *Phys. Rev. Lett.*, 108:183202, May 2012.
- [51] T. Bhamre, R. Marsland, I. K. Kominis, B. H. McGuyer, and W. Happer. Collision kernels from velocity-selective optical pumping with magnetic depolarization. *Phys. Rev. A*, 87:043412, Apr 2013.
- [52] Albert Schliesser, Markus Brehm, Fritz Keilmann, and Daniel van der Weide. Frequency-comb infrared spectrometer for rapid, remote chemical sensing. *Opt. Express*, 13(22):9029–9038, Oct 2005.
- [53] Aleksandra Foltynowicz, Ticijana Ban, Piotr Masłowski, Florian Adler, and Jun Ye. Quantum-noise-limited optical frequency comb spectroscopy. *Phys. Rev. Lett.*, 107:233002, Nov 2011.
- [54] T. M. Stace and A. N. Luiten. Theory of spectroscopy in an optically pumped effusive vapor. *Phys. Rev. A*, 81:033848, Mar 2010.
- [55] Thomas M. Stace, Gar-Wing Truong, James Anstie, Eric F. May, and André N. Luiten. Power-dependent line-shape corrections for quantitative spectroscopy. *Phys. Rev. A*, 86:012506, Jul 2012.

- [56] Biswaroop Mukherjee, Zhenjie Yan, Parth B. Patel, Zoran Hadzibabic, Tarik Yefsah, Julian Struck, and Martin W. Zwierlein. Homogeneous atomic fermi gases. *Phys. Rev. Lett.*, 118:123401, Mar 2017.
- [57] Klaus Hueck, Niclas Luick, Lennart Sobirey, Jonas Siegl, Thomas Lompe, and Henning Moritz. Two-dimensional homogeneous fermi gases. *Phys. Rev. Lett.*, 120:060402, Feb 2018.
- [58] Ilya Berdnikov, P. Coleman, and Steven H. Simon. Itinerant ferromagnetism in an atom trap. *Phys. Rev. B*, 79:224403, Jun 2009.
- [59] R. A. Duine and A. H. MacDonald. Itinerant ferromagnetism in an ultracold atom fermi gas. *Phys. Rev. Lett.*, 95:230403, Nov 2005.
- [60] L. J. LeBlanc, J. H. Thywissen, A. A. Burkov, and A. Paramekanti. Repulsive fermi gas in a harmonic trap: Ferromagnetism and spin textures. *Phys. Rev. A*, 80:013607, Jul 2009.
- [61] Paul Siddons, Charles S. Adams, Chang Ge, and Ifan G. Hughes. Absolute absorption on rubidium d lines: comparison between theory and experiment. *Journal of Physics B: Atomic, Molecular and Optical Physics*, 41(15):155004, 2008.
- [62] J Sagle, R K Namiotka, and J Huennekens. Measurement and modelling of intensity dependent absorption and transit relaxation on the cesium d_1 line. *Journal of Physics B: Atomic, Molecular and Optical Physics*, 29(12):2629, 1996.
- [63] Lee Weller, Kathrin S Kleinbach, Mark A Zentile, Svenja Knappe, Charles S Adams, and Ifan G Hughes. Absolute absorption and dispersion of a rubidium vapour in the hyperfine paschen-back regime. *Journal of Physics B: Atomic, Molecular and Optical Physics*, 45(21):215005, 2012.
- [64] D.J. Griffiths. *Introduction to Quantum Mechanics*. Pearson international edition. Pearson Prentice Hall, 2005.
- [65] Dipankar Das and Vasant Natarajan. High-precision measurement of hyperfine structure in the d lines of alkali atoms. *Journal of Physics B: Atomic, Molecular and Optical Physics*, 41(3):035001, 2008.
- [66] M. E. Gehm. *Preparation of an optically-trapped degenerate Fermi gas of 6Li : Finding the route to degeneracy*. PhD thesis, Duke University, 2003.
- [67] Albert Messiah. *Quantum Mechanics (2 Volumes in 1)*. Dover Publications, 2017.
- [68] J. Kinast. *Thermodynamics and Superfluidity of a Strongly Interacting Fermi Gas*. PhD thesis, Duke University, 2008.
- [69] *Cold Atoms and Molecules*. Wiley-VCH, 2009.
- [70] K. Huang. *Statistical mechanics*. Wiley, 1987.
- [71] Wolfgang Ketterle and Martin W. Zwierlein. Making, probing and understanding ultracold fermi gases. *Nuovo Cimento Rivista Serie*, 31:247–422, 2008.

- [72] W. Ketterle, D. S. Durfee, and D. M. Stamper-kurn. Making, probing and understanding bose-einstein condensates. In *PROCEEDINGS OF THE INTERNATIONAL SCHOOL OF PHYSICS "ENRICO FERMI", COURSE CXL, EDITED BY M. INGUSCIO, S. STRINGARI AND C.E. WIEMAN (IOS)*, page 67. Press, 1999.
- [73] *The BCS-BEC Crossover and the Unitary Fermi Gas (Lecture Notes in Physics)*. Springer, 2011.
- [74] M. Bartenstein, A. Altmeyer, S. Riedl, R. Geursen, S. Jochim, C. Chin, J. Hecker Denschlag, R. Grimm, A. Simoni, E. Tiesinga, C. J. Williams, and P. S. Julienne. Precise determination of ${}^6\text{Li}$ cold collision parameters by radio-frequency spectroscopy on weakly bound molecules. *Phys. Rev. Lett.*, 94:103201, Mar 2005.
- [75] T. A. Savard. *Raman Induced Resonance Imaging of Trapped Atoms*. PhD thesis, Duke University, 1998.
- [76] John V. Prodan, William D. Phillips, and Harold Metcalf. Laser production of a very slow monoenergetic atomic beam. *Phys. Rev. Lett.*, 49:1149–1153, Oct 1982.
- [77] Jiaming Li, Ji Liu, Leonardo de Melo, Le Luo, Tianshu Lai, and Zixin Wang. Sub-megahertz frequency stabilization of a diode laser by digital laser current modulation. *Appl. Opt.*, 54(13):3913–3917, May 2015.
- [78] Arthur L. Schawlow. Spectroscopy in a new light. *Rev. Mod. Phys.*, 54:697–707, Jul 1982.
- [79] U. Schünemann, H. Engler, R. Grimm, M. Weidemüller, and M. Zielonkowski. Simple scheme for tunable frequency offset locking of two lasers. *Review of Scientific Instruments*, 70(1):242–243, 1999.
- [80] Harold J. Metcalf and Peter van der Straten. *Laser Cooling and Trapping*. Springer-Verlag, New York, 1999.
- [81] R. Grimm, M. Weidemüller, and Y. B. Ovchinnikov. Optical dipole traps for neutral atoms. *Advances in Atomic Molecular, and Optical Physics*, 42:95–170, 2000.
- [82] L. Luo. *Entropy and Superfluid Critical Parameters of a Strongly Interacting Fermi Gas*. PhD thesis, Duke University, 2008.
- [83] C. Bason. *Hydrodynamics of a Rotating Strongly Interacting Fermi gas*. PhD thesis, Duke University, 2008.
- [84] K. M. O'Hara, S. L. Hemmer, S. R. Granade, M. E. Gehm, J. E. Thomas, V. Venturi, E. Tiesinga, and C. J. Williams. Measurement of the zero crossing in a feshbach resonance of fermionic ${}^6\text{Li}$. *Phys. Rev. A*, 66:041401, Oct 2002.
- [85] E. L. Hazlett, Y. Zhang, R. W. Stites, and K. M. O'Hara. Realization of a resonant fermi gas with a large effective range. *Phys. Rev. Lett.*, 108:045304, Jan 2012.

- [86] K. M. O'Hara, M. E. Gehm, S. R. Granade, and J. E. Thomas. Scaling laws for evaporative cooling in time-dependent optical traps. *Phys. Rev. A*, 64:051403, Oct 2001.
- [87] S. R. Granade, M. E. Gehm, K. M. O'Hara, and J. E. Thomas. All-optical production of a degenerate fermi gas. *Phys. Rev. Lett.*, 88:120405, Mar 2002.
- [88] S.R. Granade. *All-optical Production of a Degenerate Gas of 6Li: Characterization of Degeneracy*. PhD thesis, Duke University, 2002.
- [89] S. Friebel, C. D'Andrea, J. Walz, M. Weitz, and T. W. Hänsch. CO₂-laser optical lattice with cold rubidium atoms. *Phys. Rev. A*, 57:R20–R23, Jan 1998.
- [90] D. J. Han, Marshall T. DePue, and David S. Weiss. Loading and compressing cs atoms in a very far-off-resonant light trap. *Phys. Rev. A*, 63:023405, Jan 2001.
- [91] Toshiya Kinoshita, Trevor Wenger, and David S. Weiss. All-optical bose-einstein condensation using a compressible crossed dipole trap. *Phys. Rev. A*, 71:011602, Jan 2005.
- [92] J.-F. Clément, J.-P. Brantut, M. Robert-de Saint-Vincent, R. A. Nyman, A. Aspect, T. Bourdel, and P. Bouyer. All-optical runaway evaporation to bose-einstein condensation. *Phys. Rev. A*, 79:061406, Jun 2009.
- [93] D Jacob, E Mimoun, L De Sarlo, M Weitz, J Dalibard, and F Gerbier. Production of sodium bose–einstein condensates in an optical dimple trap. *New Journal of Physics*, 13(6):065022, 2011.
- [94] Chen-Lung Hung, Xibo Zhang, Nathan Gemelke, and Cheng Chin. Accelerating evaporative cooling of atoms into bose-einstein condensation in optical traps. *Phys. Rev. A*, 78:011604, Jul 2008.
- [95] Alan L. Migdall, John V. Prodan, William D. Phillips, Thomas H. Bergeman, and Harold J. Metcalf. First observation of magnetically trapped neutral atoms. *Phys. Rev. Lett.*, 54:2596–2599, Jun 1985.
- [96] S. Bize, Y. Sortais, M. S. Santos, C. Mandache, A. Clairon, and C. Salomon. High-accuracy measurement of the 87 rb ground-state hyperfine splitting in an atomic fountain. *EPL (Europhysics Letters)*, 45(5):558, 1999.
- [97] Wolfgang Ketterle and N.J. Van Druten. Evaporative cooling of trapped atoms. volume 37 of *Advances In Atomic, Molecular, and Optical Physics*, pages 181 – 236. Academic Press, 1996.
- [98] L.D. Landau, E.M. Lifshits, J.B. Sykes, and J.S. Bell. *Mechanics*. Butterworth-Heinemann. Butterworth-Heinemann, 1976.
- [99] Le Luo and J. E. Thomas. Thermodynamic measurements inastrongly interacting fermigas. *Journal of Low Temperature Physics*, 154(1):1–29, Jan 2009.
- [100] Wilhelm Zwerger. Itinerant ferromagnetism with ultracold atoms. *Science*, 325(5947):1507–1509, 2009.

- [101] G. J. Conduit. Itinerant ferromagnetism in a two-dimensional atomic gas. *Physical Review A*, 82(4):043604, 2010.
- [102] Marco Koschorreck, Daniel Pertot, Enrico Vogt, Bernd Fröhlich, Michael Feld, and Michael Köhl. Attractive and repulsive fermi polarons in two dimensions. *Nature*, 485(7400):619–622, 2012.
- [103] Christian Sanner, Edward J. Su, Aviv Keshet, Wujie Huang, Jonathon Gillen, Ralf Gommers, and Wolfgang Ketterle. Speckle imaging of spin fluctuations in a strongly interacting fermi gas. *Physical Review Letters*, 106(1):010402, 2011.
- [104] David Pekker, Mehrtash Babadi, Rajdeep Sensarma, Nikolaj Zinner, Lode Pollet, Martin W. Zwierlein, and Eugene Demler. Competition between pairing and ferromagnetic instabilities in ultracold fermi gases near feshbach resonances. *Phys. Rev. Lett.*, 106:050402, Feb 2011.
- [105] C. Kohstall, M. Zaccanti, M. Jag, A. Trenkwalder, P. Massignan, G. M. Bruun, F. Schreck, and R. Grimm. Metastability and coherence of repulsive polarons in a strongly interacting fermi mixture. *Nature*, 485(7400):615–618, 2012.
- [106] Massignan Pietro, Zaccanti Matteo, and M. Bruun Georg. Polarons, dressed molecules and itinerant ferromagnetism in ultracold fermi gases. *Reports on Progress in Physics*, 77(3):034401, 2014.
- [107] F. Chevy. Universal phase diagram of a strongly interacting fermi gas with unbalanced spin populations. *Physical Review A*, 74(6):063628, 2006.
- [108] André Schirotzek, Cheng-Hsun Wu, Ariel Sommer, and Martin W. Zwierlein. Observation of fermi polarons in a tunable fermi liquid of ultracold atoms. *Physical Review Letters*, 102(23):230402, 2009.
- [109] Michael Klawunn and Alessio Recati. Fermi polaron in two dimensions: Importance of the two-body bound state. *Physical Review A*, 84(3):033607, 2011.
- [110] P. Massignan and G. M. Bruun. Repulsive polarons and itinerant ferromagnetism in strongly polarized fermi gases. *The European Physical Journal D*, 65(1):83–89, 2011.
- [111] D. S. Petrov. Three-body problem in fermi gases with short-range interparticle interaction. *Phys. Rev. A*, 67:010703, Jan 2003.
- [112] F. Scazza, G. Valtolina, P. Massignan, A. Recati, A. Amico, A. Burchianti, C. Fort, M. Inguscio, M. Zaccanti, and G. Roati. Repulsive fermi polarons in a resonant mixture of ultracold ${}^6\text{Li}$ atoms. *Phys. Rev. Lett.*, 118:083602, Feb 2017.
- [113] Yingyi Zhang. *Radio Frequency Spectroscopy Of a Quasi-Two-Dimensional Fermi Gas*. Ph.d., Duke, 2013.
- [114] T. M. Whitehead, L. M. Schonenberg, N. Kongsuwan, R. J. Needs, and G. J. Conduit. Pseudopotential for the two-dimensional contact interaction. *Physical Review A*, 93(4):042702, 2016.
- [115] Richard Schmidt, Tilman Enss, Ville Pietilä, and Eugene Demler. Fermi polarons in two dimensions. *Physical Review A*, 85(2):021602, 2012.

- [116] Ngampruetikorn Vudtiwat, Levinsen Jesper, and M. Parish Meera. Repulsive polarons in two-dimensional fermi gases. *EPL (Europhysics Letters)*, 98(3):30005, 2012.
- [117] P. B. Blakie, A. Bezett, and P. Buonsante. Degenerate fermi gas in a combined harmonic-lattice potential. *Phys. Rev. A*, 75:063609, Jun 2007.
- [118] Michael Feld. *Low temperature phases of interacting fermions in two dimensions*. Ph.d., Cambridge University, 2011.
- [119] Immanuel Bloch, Jean Dalibard, and Wilhelm Zwerger. Many-body physics with ultracold gases. *Rev. Mod. Phys.*, 80:885–964, Jul 2008.
- [120] D. S. Petrov and G. V. Shlyapnikov. Interatomic collisions in a tightly confined bose gas. *Phys. Rev. A*, 64:012706, Jun 2001.
- [121] G. Shimkaveg, W. W. Quivers, R. R. Dasari, and M. S. Feld. Direct measurement of velocity-changing collision cross sections by laser optical pumping. *Phys. Rev. A*, 48:1409–1418, Aug 1993.
- [122] Rodney Loudon. *The Quantum Theory of Light*. Oxford university press, 2000. Pg. 68–70.
- [123] Graham D. Bruce, Sarah L. Bromley, Giuseppe Smirne, Lara Torralbo-Campo, and Donatella Cassetari. Holographic power-law traps for the efficient production of bose-einstein condensates. *Phys. Rev. A*, 84:053410, Nov 2011.

APPENDICES

A. Physical Constants & ${}^6\text{Li}$ Properties

Table A.1.
 ${}^6\text{Li}$ properties

Symbol	Value	Definition
m	$9.9883414 \times 10^{-27}$ kg	Mass
λ	670.977338 nm	D_2 Wavelength
Γ	5.8724 MHz	D_2 Natural Linewidth
$\langle J = 1/2 \boldsymbol{\mu}^{(1)} J' = 3/2 \rangle$	3.977×10^{-18} C·m	D_2 Reduced Matrix Element
I_{sat}	2.54 mW/cm ²	D_2 Saturation Intensity
$E_R(1064\text{nm})$	$k_B \times 1.405$ μK	Recoil energy

Table A.2.
Physical constants

Symbol	Value	Definition
\hbar	$1.054571800 \times 10^{-34}$ J·s	Reduced Planck constant
c	299792458 m·s ⁻¹	Speed of light in vacuum
ϵ_0	$8.854187817 \times 10^{-12}$ F·m ⁻¹	Vacuum permittivity
μ_B	$9.274009994 \times 10^{-24}$ J·T ⁻¹	Bohr magneton
k_B	$1.38064852 \times 10^{-23}$ J·K ⁻¹	Boltzmann constant
a_0	$5.2917721067 \times 10^{-11}$ m	Bohr radius

B. Mathematica Code for Parametric Cooling

Below is the Mathematica code written by Ji Liu to obtain simulation results presented in Figs. 4.6 and 4.7. The code follows the steps listed in Sec. 4.5 to calculate all the theoretical results. The theoretical model uses a classical approach to simulate the dynamics of the atoms in the trap, then uses Fermi statistics to calculate numerical values for measured quantities.

```

c = 2.99792458 * 108; (*Speed of light, unit: m/s*)
ħ = 1.05457 * 10-34; (*Reduced Planck Const*)
e = 1.60217 * 10-19; (*Electron Charge*)
ε0 = 8.8542 * 10-12; (*permittivity*)
kB = 1.38065 * 10-23; (*Boltzmann Constant*)
h = 2 π ħ;
γ = 5.8724 * 106; (*nature linewidth of D2 line, unit: Hz*)
Γ = 2 π γ;
ν0 = 4.467997 * 1014; (*resonance frequency at D2 line, unit: Hz*)
ω0 = 2 π ν0;
λ0 = c / ν0;
λtrap = 1.064 * 10-6; (*Trap laser wavelength,
here assume YAG laser, 1.064 um wavelength*)
νtrap = c / λtrap; (*Trap laser frequency,unit: Hz*)
ωtrap = 2 π νtrap;
mLi6 = 9.98834 * 10-27; (*Mass of Li6 atoms, unit: kg*)
a0 = 5.29177 * 10-11; (* Bohr radius *)

```

(*Trap Setting*)

```

wout = 36 * 10^(-6);
Ptrap = 0.65;
z0 =  $\frac{\pi wout^2}{\lambda_{trap}}$ ;
I0 =  $\frac{2 Ptrap}{\pi wout^2}$ ;
CrossAngle = 6 Degree;
U0 =  $\frac{3 \pi c^2}{2 \omega_0^3} \times \left( \frac{\Gamma}{\omega_0 - \omega_{trap}} + \frac{\Gamma}{\omega_0 + \omega_{trap}} \right) \times I_0$ 

```

(*Arbitrary degree Cross Beam trap *)

```

IGaussianAb01[x_, y_, z_, θ_] := I0  $\left( \frac{wout}{wout * \text{Sqrt}[1 + (x * \text{Cos}[\theta] - y * \text{Sin}[\theta])^2 / z_0^2]} \right)^2$ 
Exp[- $\frac{2 (z^2 + (x * \text{Sin}[\theta] + y * \text{Cos}[\theta])^2)}{(wout * \text{Sqrt}[1 + (x * \text{Cos}[\theta] - y * \text{Sin}[\theta])^2 / z_0^2])^2}$ ];
UAb01[x_, y_, z_, θ_] := -U0 *  $\frac{IGaussianAb01[x, y, z, \theta]}{I_0}$ ;
IGaussianAb02[x_, y_, z_, θ_] :=
I0  $\left( \frac{wout}{wout * \text{Sqrt}[1 + (x * \text{Cos}[\theta] + y * \text{Sin}[\theta])^2 / z_0^2]} \right)^2$ 
Exp[- $\frac{2 (z^2 + (-x * \text{Sin}[\theta] + y * \text{Cos}[\theta])^2)}{(wout * \text{Sqrt}[1 + (x * \text{Cos}[\theta] + y * \text{Sin}[\theta])^2 / z_0^2])^2}$ ];
UAb02[x_, y_, z_, θ_] := -U0 *  $\frac{IGaussianAb02[x, y, z, \theta]}{I_0}$ ;
UcrossAb[x_, y_, z_] := UAb01[x, y, z, CrossAngle] + UAb02[x, y, z, CrossAngle] + 2 U0;

```

(*Trap Frequency AnHarmonic*)

```

ωxxAnHarmonic[x0] :=
Pi * Sqrt[2 / mLi6] * 1 / NIntegrate[Sqrt[1 / (UcrossAb[x0, θ, θ] - UcrossAb[x, θ, θ])],
{x, -x0 * 0.9999999, x0 * 0.9999999}]

```

```

ωyxAnHarmonic[x_] :=
  Pi * Sqrt[2/mli6] * 1/NIntegrate[Sqrt[1/(UcrossAb[x, y0, 0] - UcrossAb[x, y, 0])],
    {y, -y0 * 0.9999999, y0 * 0.9999999}]

xd = FindRoot[(2 U0 - UcrossAb[x, 0, 0]) / (2 U0) == 2/3, {x, 0.00015}]
yd = FindRoot[(2 U0 - UcrossAb[0, y, 0]) / (2 U0) == 2/3, {y, 0.00015}]
N[xd[[1]][[2]]/yd[[1]][[2]]]
ωyyAnHarmonic[y0_] :=
  Pi * Sqrt[2/mli6] * 1/NIntegrate[Sqrt[1/(UcrossAb[0, y0, 0] - UcrossAb[0, y, 0])],
    {y, -y0 * 0.9999999, y0 * 0.9999999}]

```

(*Oscillation Short Axis, High Frequency Side*)

```

GaussData = Table[{y, UcrossAb[0, y, 0]}, {y, -0.0001, 0.0001, 0.000001}];
ListPlot[GaussData, PlotRange -> All];
FindFit[GaussData, A * Exp[-2 * x^2 /waist^2],
  {{A, 5.33 * 10^-28}, {waist, 0.000036}}, x]
DUcross = D[UcrossAb[0, y, 0], y]
TrapFreqX = ωyyAnHarmonic[0.0000002] * 0.707
ωp = 2 * TrapFreqX
DeltaU = 0.5 * U0;
Time = 1 /ωp * 2 Pi * 10
TrapPotential[t_, Theta_?NumericQ] := (2 * U0 + DeltaU * Cos[(ωp) * t + Theta]) (/) 2 * U0
)

```

AmpTheta[Theta_?NumericQ] :=

$$\left(y[\text{Time}] /. \text{NDSolve} \left[\left\{ y''[t] + 1/mli6 * \text{TrapPotential}[t, \text{Theta}] * \right. \right. \right. \\ \left. \left. \left(\left(7.961593544882919 \cdot 10^{-25} e^{-\frac{1250000000 y[t]^2 \cos[6^\circ]^2}{81 (1+746.1783408606012 y[t]^2)}} y[t] \right) / \right. \right. \\ \left. \left. (1 + 746.1783408606012 y[t]^2)^2 - (5.334913323603345 \cdot 10^{-28} \right. \right. \\ \left. \left. e^{-\frac{1250000000 y[t]^2 \cos[6^\circ]^2}{81 (1+746.1783408606012 y[t]^2)}} \left(\frac{2.277856318970571 \cdot 10^{12} y[t]^3}{(1 + 746.1783408606012 y[t]^2)^2} - \right. \right. \\ \left. \left. \frac{25000000000 y[t] \cos[6^\circ]^2}{81 (1 + 746.1783408606012 y[t]^2)} \right) \right) / (1 + 746.1783408606012 y[t]^2) \right) = \\ \left. \left. \left. \theta, y[0] == 0.0000025, y'[0] == 0 \right\}, y, \{t, \theta, \text{Time}\} \right] \right) [[1]];$$

VelocityTheta[Theta_?NumericQ] := y'[Time] /.

$$\text{NDSolve} \left[\left\{ y''[t] + 1/mli6 * \text{TrapPotential}[t, \text{Theta}] * \right. \right. \\ \left. \left. \left(\left(7.961593544882919 \cdot 10^{-25} e^{-\frac{1250000000 y[t]^2 \cos[6^\circ]^2}{81 (1+746.1783408606012 y[t]^2)}} y[t] \right) / \right. \right. \\ \left. \left. (1 + 746.1783408606012 y[t]^2)^2 - (5.334913323603345 \cdot 10^{-28} \right. \right. \\ \left. \left. e^{-\frac{1250000000 y[t]^2 \cos[6^\circ]^2}{81 (1+746.1783408606012 y[t]^2)}} \left(\frac{2.277856318970571 \cdot 10^{12} y[t]^3}{(1 + 746.1783408606012 y[t]^2)^2} - \right. \right. \\ \left. \left. \frac{25000000000 y[t] \cos[6^\circ]^2}{81 (1 + 746.1783408606012 y[t]^2)} \right) \right) / (1 + 746.1783408606012 y[t]^2) \right) = \\ \left. \left. \left. \theta, y[0] == 0.0000025, y'[0] == 0 \right\}, y, \{t, \theta, \text{Time}\} \right] \right) [[1]];$$

Energy[Theta_] := (1/2 mli6 VelocityTheta[Theta]^2 + UcrossAb[AmpTheta[Theta], \theta, \theta]);

(*Finite Temperature Fermi Gas Oscillation Amplitude Property Calculation*)

```

(*chemical Potential Vs T*)
(*reduced parameter equation of chemical potential by using  $x = \frac{\epsilon}{e_f}, \mu = \frac{\mu}{e_f}, T' = \frac{T}{T_f}$ *)

f1[x_, mu_, T_] :=  $\frac{x^2}{\text{Exp}\left[\frac{x-\mu}{T}\right] + 1}$ ;

Integrate[f1[x, mu, T1], {x, 0, Infinity}];
g1[mu_, T_] := -2 T^3 PolyLog[3, -Exp[mu / T]];
j2[T_] := FindMinimum[(1 - 3 * g1[z, T])^2, {z, {0.01, 1}}]
mu[T_] := {z /. Part[j2[T], 2]}[[1, 1]]
mulist = Table[{T, mu[T]}, {T, 0.01, 1.0, 0.01}];

ToverTF = 0.7;
Trapwaist = wout;
Natom = 4 * 10^5; (*Total Atomic Number in the Trap*)
wx = 2 Pi 2051;
wy = 2 Pi 2403;
wz = 2 Pi 237.8;
w = (wx wy wz)^{1/3};
g[ε_] :=  $\frac{e^2}{2 (\hbar w)^3}$ ; (*density of state*)
f[ε_, T_] :=  $\frac{1}{\text{Exp}\left[\frac{(\epsilon - \mu)}{(k_B T)}\right] + 1}$ ; (*Occupation number*)
EF = (3 Natom)^{1/3} \hbar w;
TF =  $\frac{EF}{k_B}$ ;
(*FermiRadii= Sqrt[2*EF/mli6/wx^2] * Sqrt[1 + (wx*0.0005)^2] / (Natom/2)^{1/6};*)
EnergyDist[ε_, T_] :=  $\frac{1}{\text{Exp}\left[\frac{(\epsilon - \mu[T] * EF)}{(k_B T * TF)}\right] + 1}$ ;
Amplitude[x_, T_] := EnergyDist[1/2 * mli6 * wx^2 * x^2, T]

IntialAtomCoeffiency = Natom / NIntegrate[Amplitude[x, ToverTF], {x, 10^-8, Trapwaist}];
PositionCalStep = 0.5 * 10^-6;
ThetaCalStep = 0.2;
AtomIntialPositionThetaDist = Table[
  IntialAtomCoeffiency * Amplitude[x, ToverTF] * PositionCalStep * ThetaCalStep / (2 Pi),
  {x, 10^-8, Trapwaist, PositionCalStep}, {Theta, 10^-3, 2 Pi * 0.999, ThetaCalStep}];
Total[Total[AtomIntialPositionThetaDist]]

OscEnergyTable1 = ParallelTable[Energy[x, Theta],
  {x, 10^-8, Trapwaist, PositionCalStep}, {Theta, 10^-3, 2 Pi * 0.999, ThetaCalStep}];
OscEnergyTable = ParallelTable[If[OscEnergyTable1[[x]][[y]] ≥ U0,
  0, OscEnergyTable1[[x]][[y]]], {x, 1, 72}, {y, 1, 32}];
OscFinalResult = OscEnergyTable * AtomIntialPositionThetaDist;
OscFinalResultRef1 = OscEnergyTable1 * AtomIntialPositionThetaDist;

AtomLeftTable = Table[If[OscEnergyTable[[x]][[y]] > 0,
  AtomIntialPositionThetaDist[[x]][[y]], 0], {x, 1, 72}, {y, 1, 32}];
AtomLeft = Tal[Total[AtomLeftTable]]

EFFinal = (3 AtomLeft)^{1/3} \hbar w
Total[Total[OscFinalResult]]

```

C. Mathematica Code for Polaron Properties

The Mathematica code written below is use to calculate the polaron properties presented in Sec. 5.4. The functions are used to calculate single points following Refs. [108, 110, 113] and polynomial fits are used to generate the line plots.

First, the polaron self-energy E_p/E_F is calculated as a function of interaction parameter $k_F a$ in three-dimensions and $\ln(k_F a_{2D})$ in two-dimensions for the repulsive attractive cases. Then the quasiparticle weights are found using the self-energy function for the repulsive and attractive polarons. Finally, using the quasiparticle weights, the decay rates are calculated.

Attractive 2D Polaron

```

Polaron2Dselfenergy[x_, a_] := -2 *
  NIntegrate[ $\frac{1}{-a + \text{Log}[\sqrt{(1-x/2)^2 - u} + (1-x/2 - u/2)]}$ , {u, 0, 1}, MaxRecursion -> 30];
(*Σ(ε), a= Ln(Eb/EF), x=polaron energy*)
Energy2D[a_] :=
  Re[FindRoot[x == -2 * NIntegrate[ $\frac{1}{-a + \text{Log}[\sqrt{(1-x/2)^2 - u} + (1-x/2 - u/2)]}$ , {u, 0, 1},
    MaxRecursion -> 30], {x, -4.5}][[1]][[2]]];
(*Σ(ε) = ε, this function takes in a a= Ln(Eb/EF) value to find
  the polaron energy ε=Ep/EF*)

Quasiweight2D[a_, x_] := (1 - Re[Derivative[1, 0][Polaron2Dselfenergy][x, a]])-1;
(* Quasiparticle weight, a= Ln(Eb/EF), x=polaron energy*)

```

Repulsive 2D Polaron

```

Polaron2Dselfenergy[x_, a_] := -2 * NIntegrate[ $\frac{1}{-a + \text{Log}[\sqrt{(1-x/2)^2 - u} + (1-x/2 - u/2)]}$ ,
  {u, 0, 1}, Method -> "QuasiMonteCarlo", MaxRecursion -> 10000];
(*Σ(ε), a= Ln(Eb/EF), x=polaron energy*)

Energy2D[a_] :=
  Re[FindRoot[x == -2 * Re[NIntegrate[ $\frac{1}{-a + \text{Log}[\sqrt{(1-x/2)^2 - u} + (1-x/2 - u/2)]}$ ,
    {u, 0, 1}, Method -> "QuasiMonteCarlo", MaxRecursion -> 10000}], {x, 0, 6},
    MaxIterations -> 10000, AccuracyGoal -> 10][[1]][[2]]]; (*Σ(ε) = ε,
  this function takes in a= Ln(Eb/EF) value to find the polaron energy x=Ep/EF*)

In[14]= Quasiweight2D[a_, x_] := (1 - Re[Derivative[1, 0][Polaron2Dselfenergy][x, a]])-1
(* Quasiparticle weight, a= Ln(Eb/EF), x=polaron energy*)

```

2D polaron decay rate calculation requires effective mass and $Z_+ \text{Im}[\Sigma^-] / \Delta E$ for plotting results

```

In[15]= Effm2D[x_] :=  $\left(1 - \frac{1}{2} \left(\frac{-1}{\text{Log}\left[1 + \frac{1}{x}\right]}\right)^2 (1+x)^{-2}\right)^{-1}$ ;
(*Effective mass of 2D polaron with  $x = \frac{|E_b|}{2E_F}$ *)

```

```

sigmam[a_, lnebef_, z_, deltae_] :=
  Im[ $\frac{-2}{a}$  * NIntegrate[ $\frac{1}{-lnebef + \text{Log}[z * \sqrt{(1 - \text{deltae}/2)^2 - u} + (1 - \text{deltae}/2 - u/2)]}$ ,
    {u, 0, 1}, WorkingPrecision → 12, MaxRecursion → 50, PrecisionGoal → 6]];
(*Im[Σ-], a= $\frac{m^*}{m}$ , lnebef=Ln( $\frac{E_k}{E_f}$ ), z=Z-, deltae=E+-E- *)

```

3D Polaron

```

ln[12]= Secondaryintegral[y_?NumericQ, ε_?NumericQ] :=
  NIntegrate[ $\frac{x}{2 * y} \text{Log}[\frac{2 x^2 + 2 * x * y - \epsilon}{2 x^2 - 2 * x * y - \epsilon}] - 1$ , {x, 1, Infinity}];
(* ε=polaron energy*)
Energy3D[x_, ak_] := -2 * NIntegrate[ $\frac{y^2}{1 - \frac{\pi}{2} * ak - \text{Secondaryintegral}[y, x]}$ ,
  {y, 0, 1}, WorkingPrecision → 12, MaxRecursion → 100000];
(*Σ(ε)= ε, this function takes in ak= kfa value to find the polaron energy *)
EnergyRootFind3D[ak_, z1_] :=
  FindRoot[z == -2 * NIntegrate[ $\frac{y^2}{1 - \frac{\pi}{2} * ak - \text{Secondaryintegral}[y, z]}$ , {y, 0, 1}], {z, z1},
  WorkingPrecision → 15] [[1]] [[2]]; (*Σ(ε)= ε, this function takes in ak=
  kfa value to find the polaron energy z=Ep/Ef with initial guess z1*)
Quasiweight3D[a_, x_] := (1 - Re[Derivative[1, 0][Energy3D][x, a]])-1;
(* Quasiparticle weight, a= kfa, x=polaron energy*)

```

To find the decay rate of the repulsive polaron, must find effective mass first, $\Gamma_{pp} = -Z_+ \text{Im}\{\Sigma^-\}$

```

ln[8]= Effm[ep_, ak_] :=  $(1 - \frac{1}{2} (ep/2)^2 (1 + (ak^2))^{-2})^{-1}$ ;
(*Attractive polaron effective mass, ep= polaron energy, ak=kfa*)
Secondaryintegral2[y_?NumericQ, ε_?NumericQ, me_] :=
  NIntegrate[ $\frac{(x * me)}{2 * y} \text{Log}[\frac{2 (x * me)^2 + 2 * (x * me) * y - \epsilon}{2 (x * me)^2 - 2 * (x * me) * y - \epsilon}] - 1$ ,
  {x, 1, Infinity}, WorkingPrecision → 12, MaxRecursion → 100];
(* ε=polaron energy, me is the effective mass *)
Energy3Dimaginary[ak_, e_, z_, me_] :=
  Im[-2 * NIntegrate[ $\frac{y^2}{1 - \frac{\pi}{2} * ak - z * \text{Secondaryintegral2}[y, e, me]}$ ,
  {y, 0, 1}, WorkingPrecision → 12, MaxRecursion → 50, PrecisionGoal → 6]];
(*Im{Σ-}, ak=1/kfa, e=(E+-E-)/Ef, z=Z-*)

```

D. Mathematica Code for Absolute Absorption

The Mathematica code written below was written by Ji Liu to numerically solve the system of coupled equations using the procedure outlined in Sec. 6.2. This code was run on the Big red 2 supercomputer at Indiana University. In the simulation, trial γ_{vc} values are used in two iterations to calculate the spatial beam intensity profile. The code included here is the first iteration with a guess for $\Omega_0^2(r, z)$. For the second iteration, line 17 of the code that has the $\Omega_0^2(r, z)$, is replaced with the output file of the first iteration, which is line 54 of the code below.

This simulation is run for every experimental value of beam power percentage through the iris and I/I_{sat} value. The output file from the second iteration is used to calculate the transmission through the gas, then the calculated values are compared to experimental values for each γ_{vc} value.

```

#!/ /N/soft/rhel6/mathematica/11.1.1/bin/math -script

\[\Beta]=0.6;
\[\CapitalOmega]20=0.05;
\[\CapitalGamma]=36.90*10^6; (*Hz*)
temp=603 ;(*340C for cell center*)
kb=1.38*10^-23;
m=0.9988*10^-26;
\[\CapitalDelta]=228.2*10^6*Pi/\[\CapitalGamma]; (*Half of Hyperfine splitting of
ground state, in reduced units*)
vmean[temp_]:=Sqrt[2*kb*temp/m];
v0=vmean[temp] ;(*average velocity, unit in m/s*)
r0=0.0025; (*laser beam radius, unit in m*)
\[\Lambda]=670.977*10^-9;(*unit in m*)
v0star=v0/(r0*\[\CapitalGamma]);(*dimensionless velocity*)
\[\CapitalOmega]2Input[r_]:= \[\CapitalOmega]20*Exp[-r^2];
F\[\Tau][v\[\Tau]_?NumericQ,v0_?NumericQ]:=(2*v\[\Tau]*Exp[-(v\[\Tau]/v0)^2])/v0^2;
\[\CapitalOmega]2Test0[r_,z]:= \[\CapitalOmega]20*Exp[-z*0.75]*Exp[-r^2];
\[\Delta]Table={-3,-2,-1.5,-1.3,-1.1,-1.09,-1.07,-1.05,-1.03,-1.01,-1.005,-1,-0.995,-0.
99,-0.97,-0.95,-0.93,-0.91,-0.9,0.9,0.9,0.91,0.93,0.95,0.97,0.99,0.995,1,1.005,1.01,1.03
,1.05,1.07,1.09,1.1,1.3,1.5,2,3}*\[\CapitalDelta]; (*I integrate the whole regions of
hyperfine split in higher precision*)
VCC=1; (*VCC rate, dimensionless*)
XYTable=Range[-2.2,2.2,0.2];
(*First Iteration*)
RTable={0,0.2,0.4,0.6,0.8,1,1.2,1.4,1.6,1.8,2,2.2};

\[\CapitalOmega]2Test1[r_,z]:=Piecewise[{{\[\CapitalOmega]2Test0[r,z],r<2.2},{0,r>=2.2}
}];
(*Definition of All parameters in the M Matrix*)
\[\CapitalGamma]=1;

M11[\[\Delta]_,\[\CapitalOmega]2_]=Simplify[(-24 \[\CapitalGamma]^3
\[\CapitalDelta]^2-96 \[\CapitalGamma] \[\Delta]^2 \[\CapitalDelta]^2+192
\[\CapitalGamma] \[\Delta] \[\CapitalDelta]^3-96 \[\CapitalGamma] \[\CapitalDelta]^4)
\[\CapitalOmega]2+(-64 \[\CapitalGamma] \[\Delta] \[\CapitalDelta]^4+64 \[\CapitalGamma]
\[\CapitalDelta]^2) \[\CapitalOmega]2^2-16 \[\CapitalGamma] \[\CapitalOmega]2^3)/(9
\[\CapitalGamma]^4 \[\CapitalDelta]^2+72 \[\CapitalGamma]^2 \[\Delta]^2
\[\CapitalDelta]^2+144 \[\Delta]^4 \[\CapitalDelta]^2+72 \[\CapitalGamma]^2
\[\CapitalDelta]^4-288 \[\Delta]^2 \[\CapitalDelta]^4+144 \[\CapitalDelta]^6+(12
\[\CapitalGamma]^2 \[\Delta] \[\CapitalDelta]^4+48 \[\Delta]^3 \[\CapitalDelta]-36
\[\CapitalGamma]^2 \[\CapitalDelta]^2+144 \[\Delta]^2 \[\CapitalDelta]^2-48 \[\Delta]
\[\CapitalDelta]^3-144 \[\CapitalDelta]^4) \[\CapitalOmega]2+(9 \[\CapitalGamma]^2+4
\[\Delta]^2+24 \[\Delta] \[\CapitalDelta]^3+36 \[\CapitalDelta]^2) \[\CapitalOmega]2^2)
M12[\[\Delta]_,\[\CapitalOmega]2_]=Simplify[(-32 \[\CapitalGamma] \[\CapitalDelta]^2
\[\CapitalOmega]2^2+8 \[\CapitalGamma] \[\CapitalOmega]2^3)/(9 \[\CapitalGamma]^4
\[\CapitalDelta]^2+72 \[\CapitalGamma]^2 \[\Delta]^2 \[\CapitalDelta]^2+144 \[\Delta]^4
\[\CapitalDelta]^2+72 \[\CapitalGamma]^2 \[\CapitalDelta]^4-288 \[\Delta]^2
\[\CapitalDelta]^4+144 \[\CapitalDelta]^6+(12 \[\CapitalGamma]^2 \[\Delta]
\[\CapitalDelta]^4+48 \[\Delta]^3 \[\CapitalDelta]-36 \[\CapitalGamma]^2
\[\CapitalDelta]^2+144 \[\Delta]^2 \[\CapitalDelta]^2-48 \[\Delta] \[\CapitalDelta]^3-144
\[\CapitalDelta]^4) \[\CapitalOmega]2+(9 \[\CapitalGamma]^2+4 \[\Delta]^2+24 \[\Delta]
\[\CapitalDelta]^3+36 \[\CapitalDelta]^2) \[\CapitalOmega]2^2)
M13[\[\Delta]_,\[\CapitalOmega]2_]=Simplify[(9 \[\Beta] \[\CapitalGamma]^5
\[\CapitalDelta]^2+72 \[\Beta] \[\CapitalGamma]^3 \[\Delta]^2 \[\CapitalDelta]^2+144
\[\Beta] \[\CapitalGamma] \[\Delta]^4 \[\CapitalDelta]^2+72 \[\Beta] \[\CapitalGamma]^3
\[\CapitalDelta]^4-288 \[\Beta] \[\CapitalGamma] \[\Delta]^2 \[\CapitalDelta]^4+144
\[\Beta] \[\CapitalGamma] \[\CapitalDelta]^6+(12 \[\Beta] \[\CapitalGamma]^3 \[\Delta]
\[\CapitalDelta]^4+48 \[\Beta] \[\CapitalGamma] \[\Delta]^3 \[\CapitalDelta]^2+4
\[\CapitalGamma]^3 \[\CapitalDelta]^2-36 \[\Beta] \[\CapitalGamma]^3
\[\CapitalDelta]^2+96 \[\CapitalGamma] \[\Delta]^2 \[\CapitalDelta]^2+144 \[\Beta]
\[\CapitalGamma] \[\Delta]^2 \[\CapitalDelta]^2-192 \[\CapitalGamma] \[\Delta]
\[\CapitalDelta]^3-48 \[\Beta] \[\CapitalGamma] \[\Delta] \[\CapitalDelta]^3+96
\[\CapitalGamma] \[\CapitalDelta]^4-144 \[\Beta] \[\CapitalGamma] \[\CapitalDelta]^4)
\[\CapitalOmega]2+(9 \[\Beta] \[\CapitalGamma] \[\CapitalGamma]^3+4 \[\Beta] \[\CapitalGamma]
\[\Delta]^2+64 \[\CapitalGamma] \[\Delta] \[\CapitalDelta]^2+24 \[\Beta] \[\CapitalGamma]
\[\Delta] \[\CapitalDelta]-32 \[\CapitalGamma] \[\CapitalDelta]^2+36 \[\Beta]
\[\CapitalGamma] \[\CapitalDelta]^2) \[\CapitalOmega]2^2+8 \[\CapitalGamma]
\[\CapitalOmega]2^3)/(9 \[\CapitalGamma]^4 \[\CapitalDelta]^2+72 \[\CapitalGamma]^2
\[\Delta]^2 \[\CapitalDelta]^2+144 \[\Delta]^4 \[\CapitalDelta]^2+72 \[\CapitalGamma]^2
\[\CapitalDelta]^4-288 \[\Delta]^2 \[\CapitalDelta]^4+144 \[\CapitalDelta]^6+(12

```

```

\[CapitalGamma]^2 \[Delta] \[CapitalDelta]+48 \[Delta]^3 \[CapitalDelta]-36
\[CapitalGamma]^2 \[CapitalDelta]^2+144 \[Delta]^2 \[CapitalDelta]^2-48 \[Delta]
\[CapitalDelta]^3-144 \[CapitalDelta]^4) \[CapitalOmega]2+(9 \[CapitalGamma]^2+4
\[Delta]^2+24 \[Delta] \[CapitalDelta]+36 \[CapitalDelta]^2) \[CapitalOmega]2^2]]
M21\[Delta]_,\[CapitalOmega]2_]=Simplify[(-32 \[CapitalGamma] \[CapitalDelta]^2
\[CapitalOmega]2^2+8 \[CapitalGamma] \[CapitalOmega]2^3)/(9 \[CapitalGamma]^4
\[CapitalDelta]^2+72 \[CapitalGamma]^2 \[Delta]^2 \[CapitalDelta]^2+144 \[Delta]^4
\[CapitalDelta]^2+72 \[CapitalGamma]^2 \[CapitalDelta]^4-288 \[Delta]^2
\[CapitalDelta]^4+144 \[CapitalDelta]^6+(12 \[CapitalGamma]^2 \[Delta]
\[CapitalDelta]+48 \[Delta]^3 \[CapitalDelta]-36 \[CapitalGamma]^2
\[CapitalDelta]^2+144 \[Delta]^2 \[CapitalDelta]^2-48 \[Delta] \[CapitalDelta]^3-144
\[CapitalDelta]^4) \[CapitalOmega]2+(9 \[CapitalGamma]^2+4 \[Delta]^2+24 \[Delta]
\[CapitalDelta]+36 \[CapitalDelta]^2) \[CapitalOmega]2^2)]
M22\[Delta]_,\[CapitalOmega]2_]=Simplify[(-12 \[CapitalGamma]^3
\[CapitalDelta]^2-48 \[CapitalGamma] \[Delta]^2 \[CapitalDelta]^2-96 \[CapitalGamma]
\[Delta] \[CapitalDelta]^3-48 \[CapitalGamma] \[CapitalDelta]^4)
\[CapitalOmega]2+(16 \[CapitalGamma] \[Delta] \[CapitalDelta]+16 \[CapitalGamma]
\[CapitalDelta]^2) \[CapitalOmega]2^2-4 \[CapitalGamma] \[CapitalOmega]2^3)/(9
\[CapitalGamma]^4 \[CapitalDelta]^2+72 \[CapitalGamma]^2 \[Delta]^2
\[CapitalDelta]^2+144 \[Delta]^4 \[CapitalDelta]^2+72 \[CapitalGamma]^2
\[CapitalDelta]^4-288 \[Delta]^2 \[CapitalDelta]^4+144 \[CapitalDelta]^6+(12
\[CapitalGamma]^2 \[Delta] \[CapitalDelta]+48 \[Delta]^3 \[CapitalDelta]-36
\[CapitalGamma]^2 \[CapitalDelta]^2+144 \[Delta]^2 \[CapitalDelta]^2-48 \[Delta]
\[CapitalDelta]^3-144 \[CapitalDelta]^4) \[CapitalOmega]2+(9 \[CapitalGamma]^2+4
\[Delta]^2+24 \[Delta] \[CapitalDelta]+36 \[CapitalDelta]^2) \[CapitalOmega]2^2)]
M23\[Delta]_,\[CapitalOmega]2_]=Simplify[(9 \[CapitalGamma]^5 \[CapitalDelta]^2-9
\[Beta] \[CapitalGamma]^5 \[CapitalDelta]^2+72 \[CapitalGamma]^3 \[Delta]^2
\[CapitalDelta]^2-72 \[Beta] \[CapitalGamma]^3 \[Delta]^2 \[CapitalDelta]^2+144
\[CapitalGamma] \[Delta]^4 \[CapitalDelta]^2-144 \[Beta] \[CapitalGamma] \[Delta]^4
\[CapitalDelta]^2+72 \[CapitalGamma]^3 \[CapitalDelta]^4-72 \[Beta]
\[CapitalGamma]^3 \[CapitalDelta]^4-288 \[CapitalGamma] \[Delta]^2
\[CapitalDelta]^4+288 \[Beta] \[CapitalGamma] \[Delta]^2 \[CapitalDelta]^4+144
\[CapitalGamma] \[CapitalDelta]^6-144 \[Beta] \[CapitalGamma] \[CapitalDelta]^6+(12
\[CapitalGamma]^3 \[Delta] \[CapitalDelta]-12 \[Beta] \[CapitalGamma]^3 \[Delta]
\[CapitalDelta]+48 \[CapitalGamma] \[Delta]^3 \[CapitalDelta]-48 \[Beta]
\[CapitalGamma] \[Delta]^3 \[CapitalDelta]-24 \[CapitalGamma]^3 \[CapitalDelta]^2+36
\[Beta] \[CapitalGamma]^3 \[CapitalDelta]^2+192 \[CapitalGamma] \[Delta]^2
\[CapitalDelta]^2-144 \[Beta] \[CapitalGamma] \[Delta]^2 \[CapitalDelta]^2+48
\[CapitalGamma] \[Delta] \[CapitalDelta]^3+48 \[Beta] \[CapitalGamma] \[Delta]
\[CapitalDelta]^3-96 \[CapitalGamma] \[CapitalDelta]^4+144 \[Beta] \[CapitalGamma]
\[CapitalDelta]^4) \[CapitalOmega]2+(9 \[CapitalGamma]^3-9 \[Beta]
\[CapitalGamma]^3+4 \[CapitalGamma] \[Delta]^2-4 \[Beta] \[CapitalGamma]
\[Delta]^2+8 \[CapitalGamma] \[Delta] \[CapitalDelta]-24 \[Beta] \[CapitalGamma]
\[Delta] \[CapitalDelta]+52 \[CapitalGamma] \[CapitalDelta]^2-36 \[Beta]
\[CapitalGamma] \[CapitalDelta]^2) \[CapitalOmega]2^2-4 \[CapitalGamma]
\[CapitalOmega]2^3)/(9 \[CapitalGamma]^4 \[CapitalDelta]^2+72 \[CapitalGamma]^2
\[Delta]^2 \[CapitalDelta]^2+144 \[Delta]^4 \[CapitalDelta]^2+72 \[CapitalGamma]^2
\[CapitalDelta]^4-288 \[Delta]^2 \[CapitalDelta]^4+144 \[CapitalDelta]^6+(12
\[CapitalGamma]^2 \[Delta] \[CapitalDelta]+48 \[Delta]^3 \[CapitalDelta]-36
\[CapitalGamma]^2 \[CapitalDelta]^2+144 \[Delta]^2 \[CapitalDelta]^2-48 \[Delta]
\[CapitalDelta]^3-144 \[CapitalDelta]^4) \[CapitalOmega]2+(9 \[CapitalGamma]^2+4
\[Delta]^2+24 \[Delta] \[CapitalDelta]+36 \[CapitalDelta]^2) \[CapitalOmega]2^2)]
(*M11.etc divided by Omega2, the sponatenous parts excluded. They will be used for
absorption calculation*)
M11Div\[Delta]_,\[CapitalOmega]2_]=Simplify[(-24 \[CapitalGamma]^3
\[CapitalDelta]^2-96 \[CapitalGamma] \[Delta]^2 \[CapitalDelta]^2+192
\[CapitalGamma] \[Delta] \[CapitalDelta]^3-96 \[CapitalGamma]
\[CapitalDelta]^4)+(-64 \[CapitalGamma] \[Delta] \[CapitalDelta]+64 \[CapitalGamma]
\[CapitalDelta]^2) \[CapitalOmega]2-16 \[CapitalGamma] \[CapitalOmega]2^2)/(9
\[CapitalGamma]^4 \[CapitalDelta]^2+72 \[CapitalGamma]^2 \[Delta]^2
\[CapitalDelta]^2+144 \[Delta]^4 \[CapitalDelta]^2+72 \[CapitalGamma]^2
\[CapitalDelta]^4-288 \[Delta]^2 \[CapitalDelta]^4+144 \[CapitalDelta]^6+(12
\[CapitalGamma]^2 \[Delta] \[CapitalDelta]+48 \[Delta]^3 \[CapitalDelta]-36
\[CapitalGamma]^2 \[CapitalDelta]^2+144 \[Delta]^2 \[CapitalDelta]^2-48 \[Delta]
\[CapitalDelta]^3-144 \[CapitalDelta]^4) \[CapitalOmega]2+(9 \[CapitalGamma]^2+4
\[Delta]^2+24 \[Delta] \[CapitalDelta]+36 \[CapitalDelta]^2) \[CapitalOmega]2^2)]
M12Div\[Delta]_,\[CapitalOmega]2_]=Simplify[(-32 \[CapitalGamma] \[CapitalDelta]^2
\[CapitalOmega]2+8 \[CapitalGamma] \[CapitalOmega]2^2)/(9 \[CapitalGamma]^4
\[CapitalDelta]^2+72 \[CapitalGamma]^2 \[Delta]^2 \[CapitalDelta]^2+144 \[Delta]^4
\[CapitalDelta]^2+72 \[CapitalGamma]^2 \[CapitalDelta]^4-288 \[Delta]^2
\[CapitalDelta]^4+144 \[CapitalDelta]^6+(12 \[CapitalGamma]^2 \[Delta]

```

```

\[CapitalDelta]^48 \[Delta]^3 \[CapitalDelta]^36 \[CapitalGamma]^2
\[CapitalDelta]^2+144 \[Delta]^2 \[CapitalDelta]^2-48 \[Delta] \[CapitalDelta]^3-144
\[CapitalDelta]^4 \[CapitalOmega]^2+(9 \[CapitalGamma]^2+4 \[Delta]^2+24 \[Delta]
\[CapitalDelta]^36 \[CapitalDelta]^2) \[CapitalOmega]^2)
M13Div\[Delta]_,\[CapitalOmega]^2]=Simplify\[CapitalGamma]^8 (3
(\[CapitalGamma]^2+4 (\[Delta]-\[CapitalDelta])^2) \[CapitalDelta]^2-4
\[CapitalDelta] (-2 \[Delta]+\[CapitalDelta])
\[CapitalOmega]^2+\[CapitalOmega]^2)/(9 \[CapitalGamma]^4 \[CapitalDelta]^2+72
\[CapitalGamma]^2 \[Delta]^2 \[CapitalDelta]^2+144 \[Delta]^4 \[CapitalDelta]^2+72
\[CapitalGamma]^2 \[CapitalDelta]^4-288 \[Delta]^2 \[CapitalDelta]^4+144
\[CapitalDelta]^6+(12 \[CapitalGamma]^2 \[Delta] \[CapitalDelta]^48 \[Delta]^3
\[CapitalDelta]^36 \[CapitalGamma]^2 \[CapitalDelta]^2+144 \[Delta]^2
\[CapitalDelta]^2-48 \[Delta] \[CapitalDelta]^3-144 \[CapitalDelta]^4)
\[CapitalOmega]^2+(9 \[CapitalGamma]^2+4 \[Delta]^2+24 \[Delta] \[CapitalDelta]^36
\[CapitalDelta]^2) \[CapitalOmega]^2)
M21Div\[Delta]_,\[CapitalOmega]^2]=Simplify[(-32 \[CapitalGamma] \[CapitalDelta]^2
\[CapitalOmega]^2+8 \[CapitalGamma] \[CapitalOmega]^2)/(9 \[CapitalGamma]^4
\[CapitalDelta]^2+72 \[CapitalGamma]^2 \[Delta]^2 \[CapitalDelta]^2+144 \[Delta]^4
\[CapitalDelta]^2+72 \[CapitalGamma]^2 \[CapitalDelta]^4-288 \[Delta]^2
\[CapitalDelta]^4+144 \[CapitalDelta]^6+(12 \[CapitalGamma]^2 \[Delta]
\[CapitalDelta]^48 \[Delta]^3 \[CapitalDelta]^36 \[CapitalGamma]^2
\[CapitalDelta]^2+144 \[Delta]^2 \[CapitalDelta]^2-48 \[Delta] \[CapitalDelta]^3-144
\[CapitalDelta]^4) \[CapitalOmega]^2+(9 \[CapitalGamma]^2+4 \[Delta]^2+24 \[Delta]
\[CapitalDelta]^36 \[CapitalDelta]^2) \[CapitalOmega]^2)
M22Div\[Delta]_,\[CapitalOmega]^2]=Simplify[(-12 \[CapitalGamma]^3
\[CapitalDelta]^2-48 \[CapitalGamma] \[Delta]^2 \[CapitalDelta]^2-96 \[CapitalGamma]
\[Delta] \[CapitalDelta]^3-48 \[CapitalGamma] \[CapitalDelta]^4) +(16
\[CapitalGamma] \[Delta] \[CapitalDelta]^16 \[CapitalGamma] \[CapitalDelta]^2)
\[CapitalOmega]^2-4 \[CapitalGamma] \[CapitalOmega]^2)/(9 \[CapitalGamma]^4
\[CapitalDelta]^2+72 \[CapitalGamma]^2 \[Delta]^2 \[CapitalDelta]^2+144 \[Delta]^4
\[CapitalDelta]^2+72 \[CapitalGamma]^2 \[CapitalDelta]^4-288 \[Delta]^2
\[CapitalDelta]^4+144 \[CapitalDelta]^6+(12 \[CapitalGamma]^2 \[Delta]
\[CapitalDelta]^48 \[Delta]^3 \[CapitalDelta]^36 \[CapitalGamma]^2
\[CapitalDelta]^2+144 \[Delta]^2 \[CapitalDelta]^2-48 \[Delta] \[CapitalDelta]^3-144
\[CapitalDelta]^4) \[CapitalOmega]^2+(9 \[CapitalGamma]^2+4 \[Delta]^2+24 \[Delta]
\[CapitalDelta]^36 \[CapitalDelta]^2) \[CapitalOmega]^2)
M23Div\[Delta]_,\[CapitalOmega]^2]=Simplify[(4 \[CapitalGamma] (3 \[CapitalGamma]^2
\[CapitalDelta]^2+12 \[Delta]^2 \[CapitalDelta]^2+24 \[Delta] \[CapitalDelta]^3+12
\[CapitalDelta]^4-4 \[Delta] \[CapitalDelta] \[CapitalOmega]^2+4 \[CapitalDelta]^2
\[CapitalOmega]^2-\[CapitalOmega]^2)/(9 \[CapitalGamma]^4 \[CapitalDelta]^2+72
\[CapitalGamma]^2 \[Delta]^2 \[CapitalDelta]^2+144 \[Delta]^4 \[CapitalDelta]^2+72
\[CapitalGamma]^2 \[CapitalDelta]^4-288 \[Delta]^2 \[CapitalDelta]^4+144
\[CapitalDelta]^6+(12 \[CapitalGamma]^2 \[Delta] \[CapitalDelta]^48 \[Delta]^3
\[CapitalDelta]^36 \[CapitalGamma]^2 \[CapitalDelta]^2+144 \[Delta]^2
\[CapitalDelta]^2-48 \[Delta] \[CapitalDelta]^3-144 \[CapitalDelta]^4)
\[CapitalOmega]^2+(9 \[CapitalGamma]^2+4 \[Delta]^2+24 \[Delta] \[CapitalDelta]^36
\[CapitalDelta]^2) \[CapitalOmega]^2)
PDFE1[y_?NumericQ,z_?NumericQ,\[Delta]_?NumericQ,
v\[Tau]_?NumericQ]:=NDSolve[{v\[Tau]*P1'[x]==(M11\[Delta]_,\[CapitalOmega]^2Test1[Sqrt[
x^2+y^2],z])*P1[x]+M12\[Delta]_,\[CapitalOmega]^2Test1[Sqrt[x^2+y^2],z])*P2[x]+M13\[De
lta]_,\[CapitalOmega]^2Test1[Sqrt[x^2+y^2],z])*(1-P1[x]-P2[x])-VCC*(P1[x]-P2[x]),v\[Tau]
]*P2'[x]==(M21\[Delta]_,\[CapitalOmega]^2Test1[Sqrt[x^2+y^2],z])*P1[x]+M22\[Delta]_,\[C
apitalOmega]^2Test1[Sqrt[x^2+y^2],z])*P2[x]+M23\[Delta]_,\[CapitalOmega]^2Test1[Sqrt[x^2
+y^2],z])*(1-P1[x]-P2[x])-VCC*(P2[x]-P1[x]),P1[-2.2]==0.5,P2[-2.2]==0.5},{P1,P2},{x,-
2.2,2.2},AccuracyGoal->10,PrecisionGoal->10];
(*This is the P1, the percentage of atoms in ground state*)

PTables=ParallelTable[{P1[xx],P2[xx]}/.PDFE1[y,z,\[Delta],v\[Tau]],{y,XYTable},{z,0,2.
2,0.1},{\[Delta],\[Delta]Table},{v\[Tau],0.1*v0star,3*v0star,0.4*v0star},{xx,XYTable}];

PInterpolation11=ListInterpolation[PTables[;;;;;;,1,1]],{XYTable,{0,2.2},\[De
lta]Table,{0.1*v0star,2.9*v0star},XYTable},InterpolationOrder->1];
PInterpolation12=ListInterpolation[PTables[;;;;;;,1,2]],{XYTable,{0,2.2},\[De
lta]Table,{0.1*v0star,2.9*v0star},XYTable},InterpolationOrder->1];
PTables[;;;;;;,1,1]>>ToString[Row[{"N/dc2/scratch/ldemelo/2TransitionVCC",T
oString[VCC],"_0.1_T0-P11test.dat"}]];
PTables[;;;;;;,1,2]>>ToString[Row[{"N/dc2/scratch/ldemelo/2TransitionVCC",T
oString[VCC],"_0.1_T0-P12test.dat"}]];

```

```

\[CapitalOmega]2Result1[r_?NumericQ,zf_?NumericQ]:=\[CapitalOmega]2Input[r]*Exp[-4/Pi*
NIntegrate[F\[Tau][v\[Tau],v0star]/(4*Pi)*((-M11Div\[Delta],\[CapitalOmega]2Test1[r,z
])-M21Div\[Delta],\[CapitalOmega]2Test1[r,z])*PInterpolation11[r*Sin\[Theta],z,\[D
elta],v\[Tau],r*Cos\[Theta]]+(-M12Div\[Delta],\[CapitalOmega]2Test1[r,z])-M22Div\[
Delta],\[CapitalOmega]2Test1[r,z])*PInterpolation12[r*Sin\[Theta],z,\[Delta],v\[Tau
],r*Cos\[Theta]]+(-M13Div\[Delta],\[CapitalOmega]2Test1[r,z])-M23Div\[Delta],\[Cap
italOmega]2Test1[r,z])*(1-PInterpolation11[r*Sin\[Theta],z,\[Delta],v\[Tau],r*Cos\[
Theta]]-PInterpolation12[r*Sin\[Theta],z,\[Delta],v\[Tau],r*Cos\[Theta]]),{v\[T
au],0.1*v0star,2.9*v0star},{\[Delta],-3*\[CapitalDelta],3*\[CapitalDelta]},{\[Theta],0
,2Pi},{z,0,zf},Method->{"AdaptiveMonteCarlo"}];
Tab\[CapitalOmega]2Result1=ParallelTable\[CapitalOmega]2Result1[r,z},{r,RTable},{z,0,
2.2,0.1}];
Export[ToString[Row[{"~/2TransitionVCC",ToString[VCC],"_0.1_T0-Iter1.dat"}]],Tab\[Capi
talOmega]2Result1];

```

VITA

VITA

EDUCATION

- **Ph.D., Physics.** December 2018
Indiana University-Purdue University Indianapolis, Indianapolis, IN
- **M.S., Physics.** July 2010
Illinois Institute of Technology, Chicago, IL
- **B.S., Physics.** December 2005
Illinois Institute of Technology, Chicago, IL

PUBLICATIONS

1. Jiaming Li, Ji Liu, **Leonardo de Melo**, Le Luo, Tianshu Lai and Zixin Wang. Sub-megahertz frequency stabilization of a diode laser by digital laser current modulation. *Appl. Opt.*, 54(13):3913-3917, May 2015.
2. Jiaming Li, Ji Liu, Wen Xu, **Leonardo de Melo**, and Le Luo. Parametric cooling of a degenerate Fermi gas in an optical trap. *Phys. Rev. A*, 93:041401, Apr 2016.
3. Li, J., **de Melo, L. F.**, Luo, L. Cooling an Optically Trapped Ultracold Fermi Gas by Periodical Driving. *J. Vis. Exp.* (121), e55409, doi:10.3791/55409 (2017).

MANUSCRIPTS

- Li, J., Harter, A. K., Liu, J., **de Melo, L. F.**, Joglekar, Y. N. and Luo, L. Observation of parity-time symmetry breaking transitions in a dissipative Floquet system of ultracold atoms. arXiv: 1608.05061 [cond-mat.quant-gas] (2016).

PRESENTATIONS

Talks:

- *Realization of Strongly Interacting Fermi Gases.* **Indiana Academy of Science Annual Meeting.** Indianapolis, USA. March 2015.
- *Theoretical and Experimental Studies of Absolute Absorption of a Lithium Vapor Cell.* **APS Division of Atomic, Molecular and Optical Physics (DAMOP) Annual Meeting.** Ft. Lauderdale, USA. May 2018.

Posters:

- *A New Apparatus for Studying Dimensional Crossover and Non-Equilibrium Dynamics of Strongly Interacting Fermi Gases.* **APS Division of Atomic, Molecular and Optical Physics (DAMOP) Annual Meeting.** Quebec City, Canada. June 2013.
- *Apparatus for Non-Equilibrium and Narrow Feshbach Studies.* **Midwest Cold Atom Workshop.** Madison, USA. November 2015.
- *Quantum Control and Simulation of Ultracold ^6Li Atoms.* **IUPUI Research Day.** Indianapolis, USA. April 2016.
- *Parametric Cooling of a Non-interacting Degenerate Fermi Gas in an Optical Trap.* **Midwest Cold Atom Workshop.** Chicago, USA. November 2016.
- *Temperature Dependent Measurement of Three-body Recombination Near a Narrow Feshbach Resonance in ^6Li .* **APS Division of Atomic, Molecular and Optical Physics (DAMOP) Annual Meeting.** Sacramento, USA. May 2017.
- *An Apparatus for Studying Feshbach Resonance in Ultracold ^6Li Degenerate Fermi Gas.* **Joint Annual Conference of Physical Societies in Guangdong-Hong Kong-Macao Greater Bay Area.** Macau, China. July 2018.

AWARDS

- School of Science Graduate Student Council Travel Grant, IUPUI, 2018.
- AAAS Program for Excellence in Science, 2016.
- GK-12 Fellowship, NSF, 2012.